UNIVERSIDADE DO ESTADO DE SANTA CATARINA
CENTRO DE CIÊNCIAS TECNOLÓGICAS
PROGRAMA DE PÓS-GRADUAÇÃO EM ENGENHARIA MECÂNICA

LARISSA STEIGER DE FREITAS

NUMERICAL SIMULATION OF VERTICAL ANNULAR AND CHURN AIR-WATER TWO-PHASE FLOWS

JOINVILLE
2021

LARISSA STEIGER DE FREITAS

NUMERICAL SIMULATION OF VERTICAL ANNULAR AND CHURN AIR-WATER TWO-PHASE FLOWS

Dissertação apresentada ao Programa de Pós-Graduação em Engenharia Mecânica, da Universidade do Estado de Santa Catarina, como requisito parcial para obtenção do título de Mestra em Engenharia Mecânica, área de concentração em Modelagem e Simulação Numérica.
Orientador: Prof. Dr. Marcus Vinícius Canhoto Alves.
Coorientador: Prof. Dr. Rafael Rodrigues Francisco.

JOINVILLE
2021

Freitas, Steiger de
Numerical simulation of vertical annular and churn air-water two-phase flows / Larissa Steiger de Freitas - 2021.
105 p.

Orientador: Marcus Vinícius Canhoto Alves
Coorientador: Rafael Rodrigues Francisco
Dissertação (mestrado) - Universidade do Estado de Santa Catarina, Centro de Ciências Tecnológicas, Programa de Pós-Graduação em Engenharia Mecânica, Joinville, 2021.

1. Escoamentos bifásicos. 2. Escoamento anular. 3. Escoamento churn. 4. OpenFOAM. I. Alves, Marcus Vinícius Canhoto. II. Francisco, Rafael Rodrigues. III. Universidade do Estado de Santa Catarina, Centro de Ciências Tecnológicas, Programa de Pós-Graduação em Engenharia Mecânica. IV. Título.

LARISSA STEIGER DE FREITAS

NUMERICAL SIMULATION OF VERTICAL ANNULAR AND CHURN AIR-WATER TWO-PHASE FLOWS

Dissertação apresentada ao Programa de Pós-Graduação em Engenharia Mecânica, da Universidade do Estado de Santa Catarina, como requisito parcial para obtenção do título de Mestra em Engenharia Mecânica, área de concentração em Modelagem e Simulação Numérica.

BANCA EXAMINADORA

Prof. Dr. Marcus Vinícius Canhoto Alves
UDESC

Membros:

Prof. Dr. Luis Fernando Lamas de Oliveira
UDESC

Prof. Dr. Rigoberto Eleazar Melgarejo Morales
UTFPR

Joinville, 22 de fevereiro de 2021.

This work is dedicated to my sister Renata Steiger de Freitas, who has always been my main source of inspiration.

ACKNOWLEDGEMENTS

To my family Sergio, Clarice, Renata and Lucas for all their love, dedication and words of encouragement. Nothing would be possible without you, thank you very much.

To the professors and friends, Marcus and Rafael, for the shared knowledge and the trust bestowed upon to me. And here, I give my special thanks to the incredible mentor I had, who offered me this very interesting study subject. I am immensely grateful for the partnership and for everything I learned from you, it was a pleasure.

To the State University of Santa Catarina – UDESC and the Department of Mechanical Engineering for the opportunity.

To the Coordination for the Improvement of Higher Education Personnel – CAPES for the Master Scholarship at UDESC (grant CAPES 001).

To the Nacional Council of Scientific and Technological Development for funding this work and for the overall support to our laboratory (grant CNPq 43382020187).

To the Santa Catarina Research Foundation – FAPESC for funding this work and for the overall support to our laboratory (grants: FAPESC 2019TR000779 and FAPESC 2019TR000783).

"All err the more dangerously because each follows a truth. Their mistake lies not in following a falsehood but in not following another truth." - Blaise Pascal as an enthusiast in the fields of fluid mechanics and pressure.

ABSTRACT

Two-phase flows have several applications in areas of engineering interest. They appear in distillation towers in the chemical industry, in refrigeration equipment in the thermal and nuclear power generation industry, and in the oil industry. This work presents three-dimensional and transient investigations on the annular and churn liquid-gas flow patterns, and the transition between them. The continuity and momentum equations are solved for each phase together with a purely advective equation. The hybrid algorithm `multiphaseEulerFoam`, which couples the characteristics of two-fluid models and VOF, is used to conduct simulations that are performed with the aid of the commercial OpenFOAM software. The experiments by Govan *et al.* (1991) serve as a basis for creating the problem geometry and for introducing the initial and boundary conditions in the program. Four different meshes are simulated to check the influence of the mesh refinement on the numerical solution. It is found that a 15264-volume mesh is not thin enough to capture all the flow effects. At the other extreme, a finer mesh with 186560 volumes is able to detect a good interaction between the phases and to describe the flow in detail. However, this mesh is not the one that presents the best results when compared with the experimental data, because of its aspect ratio is worse than that of a mesh with 48760 volumes. The results for the void fraction, the pressure gradient, and the dimensionless gas superficial velocity in annular and churn flows, as well as in the transition region between them are presented, together with the 98% air isosurfaces. In general, the relative errors found for churn flows are much smaller than those found for annular flows and for the transition point. This occurs because the velocity difference between the phases are smaller, therefore reducing numerical diffusion.

Palavras-chave: Two-phase flow. Annular flow. Churn flow. OpenFOAM.

RESUMO

Os escoamentos bifásicos têm várias aplicações em áreas de interesse da engenharia. Estão presentes em destiladores na indústria química, em equipamentos de refrigeração na indústria de geração de energia térmica e nuclear, e na indústria do petróleo. Este trabalho apresenta investigações transientes e tridimensionais dos padrões de escoamento líquido-gás anular e churn, e da transição entre eles. As equações da continuidade e da quantidade de movimento são resolvidas para cada fase em conjunto com uma equação puramente advectiva. O algoritmo híbrido `multiphaseEulerFoam`, que combina as características dos modelos de dois fluidos e VOF, é utilizado para conduzir as simulações que são realizadas com o auxílio do software comercial OpenFOAM. Os experimentos de Govan *et al.* (1991) servem de base para a criação da geometria do problema e para introduzir as condições iniciais e de contorno no programa. São simuladas quatro diferentes malhas com intuito de verificar a influência do refino da malha na solução numérica. É constatado que a malha de 15264 volumes não é fina o suficiente para capturar todos os efeitos do escoamento. No outro extremo, a malha mais fina com 186560 volumes é capaz de detectar uma boa interação entre as fases e de descrever o escoamento em detalhes, porém, não é que apresenta os melhores resultados quando comparados com os dados experimentais, devido a sua razão de aspecto ser pior em relação a malha de 48760 volumes. Os resultados para a fração de vazio, para o gradiente de pressão e para a velocidade superficial adimensional do gás nos fluxos anular e churn, bem como na região de transição entre eles são apresentados, juntamente com as isosuperficies com 98% de ar. Em geral, os erros relativos encontrados para o escoamento churn são muito menores do que os encontrados para o escoamento anular e para o ponto de transição. Isto acontece, pois, as velocidades entre as fases são menores, o que gera menos difusão numérica.

Keywords: Escoamentos bifásicos. Escoamento anular. Escoamento churn. OpenFOAM.

LIST OF FIGURES

Figure 1 – Vertical two-phase gas-liquid flow patterns. From left to right: bubble flow, slug flow, churn flow and annular flow. 23
Figure 2 – Test facility used in the experiments of Lin *et al.* (2020). 26
Figure 3 – Test facility used in the experiments of Barbosa *et al.* (2001). 28
Figure 4 – Test facility used in the experiments of Wang *et al.* (2017). 29
Figure 5 – Flooding and flow reversal. 30
Figure 6 – Data for pressure gradient of a vertical pipe with fully developed air-water flow. 32
Figure 7 – Illustration of the experiment rig used by Govan *et al.* (1991) 33
Figure 8 – The volume of fluid technique for capturing the free surface interface. . . . 37
Figure 9 – Main OpenFOAM directories. 46
Figure 10 – `multiphaseEulerFoam` algorithm solution procedure. 47
Figure 11 – Pressure Implicit with Splitting of Operators (PISO) algorithm solution procedure. 48
Figure 12 – Correction in the `multiphaseEulerFoam` algorithm. 49
Figure 13 – Part of Govan *et al.* (1991) experimental rig that inspired the geometry of the simulations. 51
Figure 14 – Geometry used in simulations. 52
Figure 15 – Void fraction between the 0.296 [m] and 1.195 [m] planes for the annular flow simulated with a 15264 mesh. 56
Figure 16 – Dimensionless gas superficial velocity at 0.858 [m] from the pipe inlet for the annular flow simulated with a 15264 mesh. 57
Figure 17 – Pressure gradient at 0.858 [m] from the inlet for the annular flow simulated with a 15264 mesh. 57
Figure 18 – Isosurfaces for annular flow at 0.296 [m] simulated with a 15264 mesh. . . . 58
Figure 19 – Isosurfaces for annular flow at 1.195 [m] simulated with a 15264 mesh. . . . 59
Figure 20 – Void fraction between the 0.296 [m] and 1.195 [m] planes for the annular flow simulated with a 30528 mesh. 60
Figure 21 – Dimensionless gas superficial velocity at 0.858 [m] from the pipe inlet for the annular flow simulated with a 30528 mesh. 61
Figure 22 – Pressure gradient at 0.858 [m] from the inlet for the annular flow simulated with a 30528 mesh. 61
Figure 23 – Isosurfaces for annular flow at 0.296 [m] simulated with a 30528 mesh. . . . 62
Figure 24 – Isosurfaces for annular flow at 1.195 [m] simulated with a 30528 mesh. . . . 62
Figure 25 – Void fraction between the 0.296 [m] and 1.195 [m] planes for the annular flow simulated with a 48760 mesh. 63
Figure 26 – Dimensionless gas superficial velocity at 0.858 [m] from the pipe inlet for the annular flow simulated with a 48760 mesh. 64

Figure 27 – Pressure gradient at 0.858 [m] from the inlet for the annular flow simulated with a 48760 mesh. 64
Figure 28 – Isosurfaces for annular flow at 0.296 [m] simulated with a 48760 mesh. . . . 65
Figure 29 – Isosurfaces for annular flow at 1.195 [m] simulated with a 48760 mesh. . . . 66
Figure 30 – Void fraction between the 0.296 [m] and 1.195 [m] planes for the annular flow simulated with a 186560 mesh. 67
Figure 31 – Dimensionless gas superficial velocity measured at three different points: 0.381 [m], 0.858 [m] and 1.227 [m]. 67
Figure 32 – Pressure gradient at 0.858 [m] from the inlet for the annular flow simulated with a 186560 mesh. 68
Figure 33 – Isosurfaces for annular flow at 0.296 [m] simulated with a 186560 mesh. . . 69
Figure 34 – Isosurfaces for annular flow at 1.195 [m] simulated with a 186560 mesh. . . 69
Figure 35 – Void fraction between the 0.296 [m] and 1.195 [m] planes for the churn-annular transition simulated with a 15264 mesh. 71
Figure 36 – Dimensionless gas superficial velocity at 0.858 [m] from the pipe inlet for the churn-annular transition simulated with a 15264 mesh. 71
Figure 37 – Pressure gradient at 0.858 [m] from the inlet for the churn-annular transition simulated with a 15264 mesh. 72
Figure 38 – Isosurfaces for churn-annular transition at 0.296 [m] simulated with a 15264 mesh. 73
Figure 39 – Isosurfaces for churn-annular transition at 1.195 [m] simulated with a 15264 mesh. 73
Figure 40 – Void fraction between the 0.296 [m] and 1.195 [m] planes for the churn-annular transition simulated with a 48760 mesh. 74
Figure 41 – Dimensionless gas superficial velocity at 0.858 [m] from the pipe inlet for the churn-annular transition simulated with a 48760 mesh. 75
Figure 42 – Pressure gradient at 0.858 [m] from the inlet for the churn-annular transition simulated with a 48760 mesh. 75
Figure 43 – Isosurfaces for churn-annular transition at 0.296 [m] simulated with a 48760 mesh. 76
Figure 44 – Isosurfaces for churn-annular transition at 1.195 [m] simulated with a 48760 mesh. 77
Figure 45 – Void fraction between the 0.296 [m] and 1.195 [m] planes for the churn-annular transition simulated with a 186560 mesh. 78
Figure 46 – Dimensionless gas superficial velocity measured at three different points: 0.381 [m], 0.858 [m] and 1.227 [m]. 78
Figure 47 – Pressure gradient at 0.858 [m] from the inlet for the churn-annular transition simulated with a 186560 mesh. 79

Figure 48 – Isosurfaces for churn-annular transition at 0.296 [m] simulated with a 186560 mesh. 80
Figure 49 – Isosurfaces for churn-annular transition at 1.195 [m] simulated with a 186560 mesh. 80
Figure 50 – Void fraction between the 0.296 [m] and 1.195 [m] planes for the churn flow simulated with a 15264 mesh. 82
Figure 51 – Dimensionless gas superficial velocity at 0.858 [m] from the pipe inlet for the churn flow simulated with a 15264 mesh. 82
Figure 52 – Pressure gradient at 0.858 [m] from the inlet for the churn flow simulated with a 15264 mesh. 83
Figure 53 – Isosurfaces for annular flow at 0.296 [m] simulated with a 15264 mesh. . . . 83
Figure 54 – Isosurfaces for annular flow at 1.195 [m] simulated with a 15264 mesh. . . . 84
Figure 55 – Void fraction between the 0.296 [m] and 1.195 [m] planes for the churn flow simulated with a 30528 mesh. 85
Figure 56 – Dimensionless gas superficial velocity at 0.858 [m] from the pipe inlet for the churn flow simulated with a 30528 mesh. 86
Figure 57 – Pressure gradient at 0.858 [m] from the inlet for the churn flow simulated with a 30528 mesh. 86
Figure 58 – Isosurfaces for churn flow at 0.296 [m] simulated with a 30528 mesh. 87
Figure 59 – Isosurfaces for churn flow at 1.195 [m] simulated with a 30528 mesh. 87
Figure 60 – Void fraction between the 0.296 [m] and 1.195 [m] planes for the churn flow simulated with a 48760 mesh. 88
Figure 61 – Dimensionless gas superficial velocity at 0.858 [m] from the pipe inlet for the churn flow simulated with a 48760 mesh. 89
Figure 62 – Pressure gradient at 0.858 [m] from the inlet for the churn flow simulated with a 48760 mesh. 90
Figure 63 – Isosurfaces for churn flow at 0.296 [m] simulated with a 48760 mesh. 91
Figure 64 – Isosurfaces for churn flow at 1.195 [m] simulated with a 48760 mesh. 91
Figure 65 – Void fraction between the 0.296 [m] and 1.195 [m] planes for the churn flow simulated with a 186560 mesh. 92
Figure 66 – Dimensionless gas superficial velocity measured at three different points: 0.381 [m], 0.858 [m] and 1.227 [m]. 93
Figure 67 – Pressure gradient at 0.858 [m] from the inlet for the churn flow simulated with a 186560 mesh. 94
Figure 68 – Isosurfaces for churn flow transition at 0.296 [m] simulated with a 186560 mesh. 94
Figure 69 – Isosurfaces for churn flow transition at 1.195 [m] simulated with a 186560 mesh. 95
Figure 70 – Pressure gradients calculated with the 186560-volume mesh. 96

LIST OF TABLES

Table 1 – Turbulence model constants. 45
Table 2 – Fluids properties obtained at $T = 293.15\,[K]$ and at $P = 133000\,[Pa]$. 53
Table 3 – Boundary Conditions. 54
Table 4 – Relative errors found for annular flow. 70
Table 5 – Relative errors found for churn-annular transition. 81
Table 6 – Relative errors found for churn flow. 95

LIST OF SYMBOLS

A	Cross-sectional Area [m^2]
C_D	Drag Coefficient [-]
C_0	Courant Number [-]
C_α	Interface Compression Coefficient [-]
d_d	Droplet Diameter [m]
D	Hydraulic Cross-sectional Diameter [m]
E_R	Relative Error [-]
$\vec{F}_D$	Drag Force [N]
$\vec{F}_S$	Surface Tension Force [N]
$\vec{g}$	Gravity Acceleration [$\frac{m}{s^2}$]
G	Mass Flow [$\frac{kg}{m^2s}$]
I	Turbulent Intensity [-]
j	Superficial Velocity [$\frac{m}{s}$]
k	Turbulent Kinetic Energy [$\frac{m^2}{s^2}$]
ℓ	Turbulent Scale Length [m]
m	Mass [kg]
$\dot{m}$	Mass Flow Rate [$\frac{kg}{s}$]
M	Molar mass [$\frac{g}{mol}$]
n	Number of Moles [$mols$]
P	Pressure [Pa]
$\tilde{P}$	Turbulent Kinetic Energy Production [$\frac{Pa}{s}$]
q	Volumetric Flow Rate [$\frac{m^3}{s}$]
R	Ideal Gas Constant [$\frac{J}{K.mol}$]
R_v	Reference Value [-]
Re	Reynolds Number [-]

S	Invariant Measure of Strain Rate [$\frac{1}{s}$]
S_v	Simulated Value [-]
t	Time [s]
T	Temperature [K]
$\vec{U}$	Phase Velocity [$\frac{m}{s}$]
$\vec{U}_c$	Compression Velocity [$\frac{m}{s}$]
$\vec{U}_{ref}$	Reference Velocity [$\frac{m}{s}$]
V	Volume [m^3]
y	Distance to Nearest Wall [m]

GREEK SYMBOLS

α	Volume Fraction [-]
κ	Surface Curvature [m]
μ	Dynamic Viscosity [$Pa.s$]
ν	Kinematic Viscosity [$\frac{m^2}{s}$]
ρ	Density [$\frac{kg}{m^3}$]
σ	Surface Tension Coefficient [$\frac{N}{m}$]
ω	Turbulent Dissipation Rate [$\frac{1}{s}$]

SUBSCRIPTS

c	Continuous Phase
d	Dispersed Phase
G	Gas
k	Phase
L	Liquid
m	Mixture

CONTENTS

1 INTRODUCTION 17
1.1 Objectives 18
1.1.1 General Objectives 18
1.1.2 Specific Objectives 18
1.2 Structure of the Text 18

2 LITERATURE REVIEW 20
2.1 Multiphase Flows 20
2.1.1 Mass Flow Rate (kg/s) 20
2.1.2 Volumetric Flow Rate (m^3/s) 20
2.1.3 Mass Flow (kg/m^2s) 21
2.1.4 Superficial Velocity (m/s) 21
2.1.5 Probability of Phase k Occurrence $(dimensionless)$ 21
2.1.6 Mixture Density (kg/m^3) 22
2.1.7 Phase Velocity (m/s) 22
2.2 Two-Phase Liquid-Gas Flows 22
2.2.1 Annular Flow 24
2.2.2 Churn Flow 27
2.2.3 Churn-Annular Transition 30
2.3 The Govan *et al.* (1991) Experiment 32
2.4 Numerical Models 34
2.4.1 Eulerian and Lagrangian Descriptions 35
2.4.2 Interface-Tracking and Interface-Capturing 36
2.4.3 State of the Art 37
2.5 HyTAF (Hyperbolic Transient Annular Flow) 39

3 NUMERICAL METHODOLOGY 40
3.1 Hybrid Approach 40
3.1.1 Governing Equations 41
3.1.2 Drag Force 41
3.1.3 Surface Tension 42
3.1.4 Interface Capturing 43
3.1.5 Turbulence 43
3.1.6 Time Step 45
3.2 Numerical Procedure 46
3.2.1 OpenFoam Directories 46
3.2.2 multiphaseEulerFoam Algorithm 47

3.2.3 Computational Domain Discretization . . . 49
3.2.4 Surface Tension Correction . . . 49

4 NUMERICAL SIMULATIONS . . . 50
4.1 Characteristics of the Simulations . . . 50
4.1.1 Geometry of the Problem . . . 50
4.1.2 Fluids Properties . . . 52
4.1.3 Boundary Conditions . . . 53
4.1.4 Mesh Analysis . . . 54

5 RESULTS AND DISCUSSION . . . 55
5.1 Annular Flow . . . 55
5.1.1 Mesh 1: 15264 Volumes . . . 55
5.1.2 Mesh 2: 30528 Volumes . . . 59
5.1.3 Mesh 3: 48760 Volumes . . . 63
5.1.4 Mesh 4: 186560 Volumes . . . 66
5.2 Churn-Annular Transition . . . 70
5.2.1 Mesh 1: 15264 Volumes . . . 70
5.2.2 Mesh 3: 48760 Volumes . . . 74
5.2.3 Mesh 4: 186560 Volumes . . . 77
5.3 Churn Flow . . . 81
5.3.1 Mesh 1: 15264 Volumes . . . 81
5.3.2 Mesh 2: 30528 Volumes . . . 84
5.3.3 Mesh 3: 48760 Volumes . . . 88
5.3.4 Mesh 4: 186560 Volumes . . . 92
5.4 Pressure Gradient Comparison . . . 96

6 CONCLUSIONS . . . 97

REFERENCES . . . 99

1 INTRODUCTION

Two-phase flows have several applications in areas of great engineering interest. They appear in distillation towers in the chemical industry, in refrigeration equipment, in the thermal and nuclear power generation industry and in the oil industry.

A two-phase flow consists of two phases or components that can be macroscopically distinguished. These flows have great hydrodynamic complexity and an extremely unstable nature, in addition to their significantly different behavior, according to the assumed flow pattern (SANTOS, 2008). In vertical ducts, the flow is not subject to gravitational segregation, and depending on factors such as the velocity of the phases, the void fraction, the tension on the walls, and the pressure gradient can assume different geometries, namely: bubble flow, slug flow, churn flow and annular flow (HAFEMANN, 2015).

Transient analysis of flows with more than one phase is important to correctly predicting operational emergencies, or to verify the equipment operability in shutdown and restart situations (ALVES, 2014). An example of this importance comes from the nuclear industry, where the behavior of the fluids and their spatial distribution are directly related to the operational safety of Pressurized Water Reactors (PWR). In cases where there is a failure in the cooling of the reactors, (Loss-of-Coolant Accidents - LOCAs), the liquid film adjacent to the tube wall may dissipate, generating dried-out flows. This type of flow can rapidly increase the temperature of the pipe wall should the heat flow be kept constant, thus causing large-scale accidents.

The transient behavior prediction in two-phase gas-liquid flows is fundamental for the characterization of the annular and churn regimes (ALVES, 2014). This prediction can be carried out experimentally or through numerical simulations. However, it can be very expensive to reproduce in experimental rigs. The advancement of Computational Fluid Dynamics (CFD), was driven, among other factors, by the high cost of the experimental rigs used in the reproduction of two-phase liquid-gas flows. Thus, numerical simulations have been widely used in recent years, as they are a cheaper alternative for predicting the behavior of fluids, when compared with the test sections, since many of the software available on the market are free.

The morphology of the annular and churn flow patterns present characteristics of dispersed and segregated flows at the same time. For this reason, simulating these flow regimes can be quite complex, since the codes indicated for simulating dispersed flows are different from those indicated for segregated flows. According to Tocci (2016), for dispersed flows, the use of the two-fluid model is indicated for cases where the interface size is smaller than the numeric grid cell. In this model, each fluid must behave as a continuum and fill the entire computational domain, resulting in the loss of information during the averaging process, which can be mitigated through auxiliary closure relationships. On the other hand, interface-capturing methods usually fail in dispersed flows where the fluid elements are smaller than the grid cells. Therefore, these models are usually indicated to simulate segregated flows. The VOF method, specifically, is an interface-capturing model and is ideal for studying the effects of the liquid film on churn and annular flow patterns (PARSI *et al.*, 2016).

Thus, the best way to perform the simulations for these types of flows is to use the hybrid code developed by Wardle and Weller (2013), which can couple the characteristics of the two-fluid model and the VOF method. This algorithm is called `multiphaseEulerFoam` and is available in native OpenFOAM libraries. OpenFOAM (Open-source Field Operation and Manipulation) is an open-source commercial software, developed by OpenCFD Ltd in 2004. OpenFOAM is a simulator widely used in industry and academia, being able to solve the mechanics of the continuum, including the Computational Fluid Dynamics (CFD).

The wide occurrence of two-phase flows in the industry and their major impacts on the safety and production of industrial processes, makes the transient prediction of their behaviors essential. Despite the large number of works available in the literature regarding two-phase vertical liquid-gas flows, most present simplified models and empirical correlations for calculating pressure drops in only one dimension, which does not describe the behavior of fluids in depth.

1.1 OBJECTIVES

1.1.1 General Objectives

This work aims to investigate parameters associated with annular and churn flow patterns, as well as the transition between them, through transient and three-dimensional simulations.

1.1.2 Specific Objectives

- To simulate two-phase flows using the hybrid code developed by Wardle and Weller (2013), through the commercial software OpenFOAM;
- To obtain pressure gradients for the same measurement points used by Govan *et al.* (1991);
- To analyze the behavior of gas void fractions and dimensionless gas velocities;
- To obtain isosurfaces to investigate the flow patterns in detail and to compare them with the behavior described in the literature.

1.2 STRUCTURE OF THE TEXT

The present work is divided into six chapters. The first presents an introduction on the subject, the justification, and the general and specific objectives to be achieved. The concept of multiphase flow is presented, its importance for the industry is highlighted, and the main methods for modeling segregated and dispersed flows are briefly commented.

The second chapter presents a literature review on the subject, which describes some of the main parameters of multiphase flows. The geometries of the vertical two-phase flow patterns are presented, and some specific concepts of annular flow, churn flow and the transition between them are commented, as well as the associated flooding and flow reversal phenomena. The experiment by Govan *et al.* (1991) used to validate the present work detailed. Finally, some numerical works developed in recent years are presented, as well as the HyTAF model.

Chapter three presents the governing equations that constitute the hybrid formulation proposed by Wardle and Weller (2013). The continuity equation, the momentum equation and the relations for drag forces and for surface tension are presented. In addition, a purely advective equation to capture the interface between the phases is presented. The turbulence models used in the simulation are also discussed, and the Courant criteria that controls the time step of the simulations is defined. Finally, some concepts about the numerical procedure are discussed, such as the functioning of the internal OpenFoam directories and some details about the hybrid algorithm used, as well as the methods of discretization. In addition, a small correction made for surface tension is presented in this chapter.

Chapter four contains important information used to conduct the simulations. First, the geometry of the problem is described, and the properties of the fluids are commented. The boundary conditions required to start the simulation are presented and, finally, the meshes tested in the simulations are briefly discussed.

Chapter five presents and discusses the results obtained for the void fractions, the dimensionless gas superficial velocities and the pressure gradients. Several meshes are tested for annular and churn flow patterns, and for a point located in the transition between these two flow regimes. In addition, some isosurfaces that allow the visualization of the flows over time are presented. Finally, chapter six presents the final considerations and suggestions for future works.

2 LITERATURE REVIEW

In this chapter, a brief literature review is presented. Initially, some important parameters about multiphase flows are introduced, and the possible configurations for two-phase liquid-gas flows are explained. Then, annular flow, churn flow, and the transition between these flow patterns are discussed, as well as the associated flooding and flow reversal phenomena. The experiment by Govan *et al.* (1991), used to validate the present work, is detailed. Finally, some numerical works developed in recent years are presented, as well as the HyTAF model.

2.1 MULTIPHASE FLOWS

A multiphase flow is composed of two or more phases or components that can be macroscopically distinguished. According to Rosa (2012), the term *phase* can be understood as a homogeneous spatial region with well-defined transport and state properties, and that is delimited by an infinitesimal thickness interface.

It is possible to classify the two-phase flows according to the phases involved: gas-liquid, gas-solid, liquid-liquid and liquid-solid. The present work has as its object of study the two-phase flows that occur specifically when gases and liquids are the phases in motion. According to Crowe (2006), these flows are generally classified as segregated and dispersed. For the segregated regime, both phases are continuous, and droplets or bubbles from one phase into the other may or may not exist. In dispersed flows, one phase consists of discrete particles, such as small gas bubbles or liquid droplets, while the other phase is continuous.

Some fundamental parameters associated with multiphase flows are presented below. The definitions shown are based on Rosa (2012).

2.1.1 Mass Flow Rate (kg/s)

In the absence of chemical reactions, the mass flow rate of the mixture $(\dot{m})$ is defined by Equation 2.1 as the sum of the mass flow rates of each phase k.

$$\dot{m} = \sum_{k=1}^{n} \dot{m}_k, \tag{2.1}$$

where, $1 \leq k \leq n$, and n corresponds to the number of phases.

2.1.2 Volumetric Flow Rate (m^3/s)

In a cross section of the pipeline and in the absence of chemical reactions, the volumetric flow rate of the mixture (q) is defined by Equation 2.2 as the sum of the volumetric flow rates of each phase k.

$$q = \sum_{k=1}^{n} q_k, \tag{2.2}$$

where, $1 \leq k \leq n$.

2.1.3 Mass Flow (kg/m^2s)

In a cross section of a pipeline where no chemical reactions occur, the total mass flow of the mixture (G) is represented by the sum of the mass flow rates per unit area of each phase k, given by Equation 2.3:

$$G = \sum_{k=1}^{n} G_k \quad where \quad G_k = \frac{\dot{m}_k}{A}, \tag{2.3}$$

where, $1 \leq k \leq n$ and A is the cross-sectional area of the tube.

2.1.4 Superficial Velocity (m/s)

The superficial velocity of the mixture (j) is defined by Equation 2.4 as the sum of the volumetric flow rates per unit area of each phase k.

$$j = \sum_{k=1}^{n} j_k \quad where \quad j_k = \frac{q_k}{A}, \tag{2.4}$$

where, $1 \leq k \leq n$, and j_k corresponds to the average velocity that the phase k would have if it were flowing alone in the pipe.

2.1.5 Probability of Phase k Occurrence $(dimensionless)$

For average processes based on volume, the probability of phase k occurrence (α_k) represents the volumetric fraction of the phase k in a sampling volume, given by Equation 2.5. In addition, the sum of the probabilities of occurrence of each phase must be equal to one.

$$\sum_{k=1}^{n} \alpha_k = 1, \tag{2.5}$$

where, $1 \leq k \leq n$.

In liquid-gas flows with constant cross-section, the probability of the gas phase occurring, (α_g), is usually known as the fraction of void, whereas the probability of the liquid phase occurring, (α_l), is usually called liquid holdup. Both can be found by Equation 2.6 given below:

$$\alpha_G = \frac{A_G}{A} \quad and \quad \alpha_L = \frac{A_L}{A}, \tag{2.6}$$

where, $A = A_G + A_L$, where A_G and A_L represent the area occupied by the gas and the area occupied by the liquid, respectively.

2.1.6 Mixture Density (kg/m^3)

The mixture density (ρ_m), given by Equation 2.7, is obtained by summing the product of each phase fraction by the density of the corresponding phase.

$$\rho_m = \sum_{k=1}^{n} \alpha_k \rho_k, \tag{2.7}$$

where, $1 \leq k \leq n$.

2.1.7 Phase Velocity (m/s)

Considering a unidimensional flow in a pipe with constant transversal area, the average velocity of the phase k (U_k), given by Equation 2.8, is obtained by the ratio between the phase k volumetric flow rate and the transversal area occupied by the such phase.

$$U_k = \frac{q_k}{A_k}, \tag{2.8}$$

furthermore, the velocity of the phase k can be written in terms of the superficial velocity of the phase k and its fraction, as in the Equation 2.9:

$$U_k = \frac{j_k}{\alpha_k}. \tag{2.9}$$

2.2 TWO-PHASE LIQUID-GAS FLOWS

Although two-phase flows are present in several industrial activities, working with this type of flow is a complex matter. The mass, the moment and the energy balances are sensitive to the morphology of the components flowing inside the pipe (BRENNEN, 2005). The definitions presented in section 2.1 directly reflect on the geometry of the two-phase flows, and the spatial distribution of the phases is called flow regime (TOCCI, 2016). Each flow regime has unique characteristics governed by the properties of the phases and their corresponding fractions and the interfacial configurations (RODRIGUES, 2009). In a vertical-oriented pipe, with an internal liquid-gas flow, the flow patterns can assume different denominations, namely: bubble flow, slug flow, churn flow and annular flow, which are illustrated in Figure 1.

The bubble flow is characterized by the presence of small bubbles, with a diameter much smaller than the tube diameter, that flow in a continuous liquid phase. Discrete bubbles can assume distorted shapes and travel along the tube in the form of waves of void, interacting with each other, and presenting coalescence (ROSA, 2012).

The slug flow arises with the increase in the mixture title because of the frequent collisions between the discrete bubbles, that coalesce giving rise to elongated bubbles with a bullet shape. These new elongated bubbles fill the pipe cross-section partially or completely and are called Taylor bubbles. In addition, this flow pattern has a liquid piston region, which contains small dispersed bubbles, and a descending liquid film region (WALLIS, 1969). A recirculation region is formed when the piston and the free-falling film meet, and that results in the detachment of gas from the elongated bubble in the form of dispersed bubbles at the rear of the Taylor bubble, while the Taylor bubble nose is spherical in shape (FABRE, 2003).

As the gas flow increases or the gas phase expands because of the pressure drop, the slug flow becomes unstable and the collapse of the Taylor bubbles introduces a chaotic and oscillatory flow pattern called churn. This flow regime presents large interfacial waves where the liquid film adjacent to the walls can change its direction.

An even greater increase in gas flow leads to annular flow, where the flow reversal occurs and the the liquid film keeps the flow always upwards without oscillations (WOLFF, 2012). The annular pattern is characterized by the presence of a stable liquid film with a voluminous gas core at high speed, which has entrained liquid droplets dragged from the film by shear forces.

Figure 1 – Vertical two-phase gas-liquid flow patterns. From left to right: bubble flow, slug flow, churn flow and annular flow.

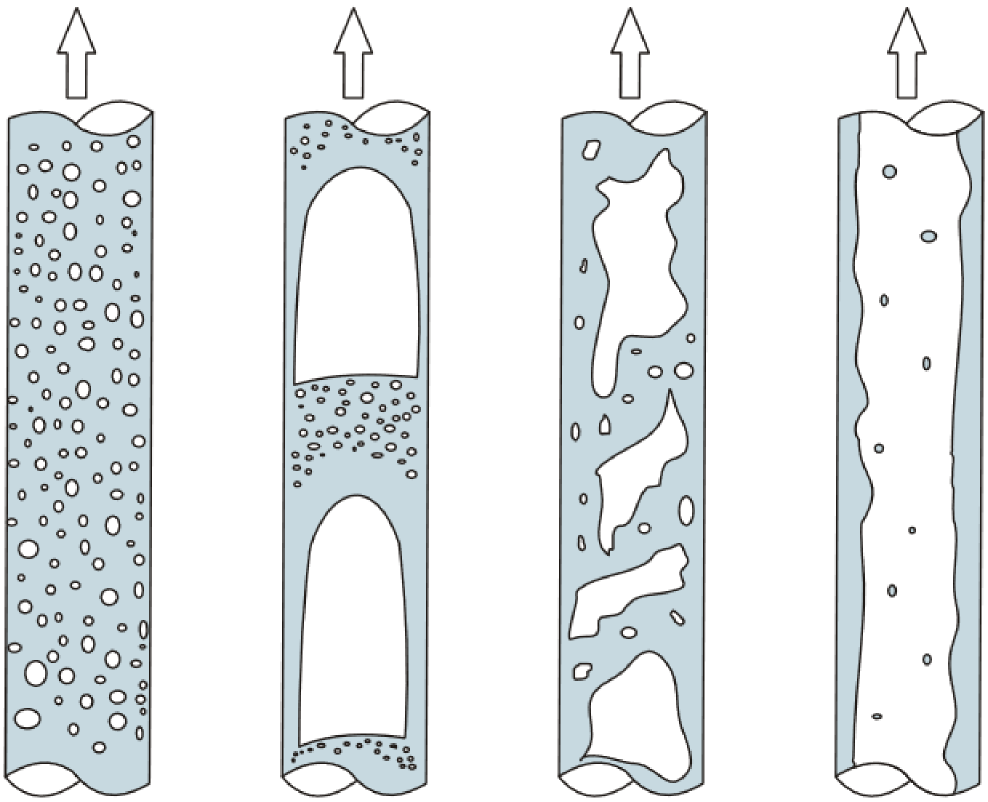

Source: Medina (2011).

The present work aims at investigating the annular and churn flows, as well as the transition between them. Thus, these flow patterns will be discussed in more detail in the subsections that follow.

2.2.1 Annular Flow

Among the flow patterns presented in section 2.2, the annular regime has the most practical applications, being the predominant pattern in most heat exchangers and steam generators, due to the wide range of flow conditions. In vertical piping, there are no gravitational segregation effects and this flow presents symmetry in relation to the central axis. Part of the liquid phase is distributed in a thin film adjacent to the tube walls, and the remaining liquid may or may not be dispersed in a continuous gas core (WOLF, 2001).

There are two main approaches to annular flow: ideal and classical. In an ideal annular flow, there is no entrainment of the liquid phase in the gas core. In other words, there are no droplets being dragged from the liquid film to the gaseous core by shearing forces, and the interface is smooth. However, this type of flow is rarely found in practice, because interfacial waves and the appearance of droplets have already been observed at relatively small flow rates. The classic approach considers that there are liquid droplets dispersed in the gas phase, and the structure of the film is complex because of disturbances resulting from different amplitudes and wavelengths (ALVES, 2014).

Investigation into the annular flow pattern began in the 1960s, when the first analytical models for the ideal annular flow emerged (BARBOSA, 2001). Hewitt (1961), established one of the first triangular relationships between the thickness of the liquid film, the mass flow in the film, and the pressure gradient. Having two of these known parameters, it is possible to find the third by using shear stress distribution models in the film. Later, other triangular relations appeared in the literature, and some are discussed in detail by Hewitt and Hall-Taylor (1970) and by Hewitt (1982).

Around the 1970s, the liquid droplets entrainment rate in the gas core began to be studied. Hutchinson and Whalley (1973), proposed empirical correlations to study this phenomenon and its relationship with the thickness of the liquid film and with the interfacial tensions. Tatterson (1975), developed an automated model that consisted in subjecting the flow to a high voltage. This model caused a pulse in the circuit, enough to estimate the size of the droplets dispersed in the gas core, since the author verified that the pulse height would be proportional to the diameter of the droplet squared. Later on, Whalley *et al.* (1974) and Whalley and Hewitt (1978), related the liquid droplets entrainment rate in the gas core to the product between a deposition coefficient, which depends on the physical properties of each phase, and the concentration of droplets in the gas core.

Theoretical and experimental studies on the turbulence in the annular flow have been abundant since the mid-1960s. The high velocity of the phases in the annular flow and the entrainment of droplets in the gas core demand turbulent flow investigations. The first studies about the turbulence analyzed the region of the liquid film only, treating the flow as being monophasic, and using Reynolds' analogy to relate the turbulent moment to the heat transfer (LEVY, 1999). Later, it was found that these models overestimate the heat transfer coefficients and the turbulence in the liquid film, giving rise to slightly more robust models.

An example of this type of modeling is the work of Dobran (1983), who studied the turbulence in the annular flow by splitting the flow into two regions: a continuous region close to the wall and a region of undulations close to the gas-liquid interface. In the continuous region, turbulence was regarded as a single-phase flow, and in the region with undulations the turbulent diffusion was proportional to its thickness. Regrettably, according to Cioncolini *et al.* (2009a), this type of model that covers two regions of the flow lacks accurate experimental data for its correct calibration. Thus, different approaches to the single-phase flow theory close to the wall were proposed by Cioncolini and Thome (2011), who provided velocity and temperature profiles, to predict different flow parameters with greater precision when compared to previous works.

Between the 1980s and 1990s, several studies that investigated the parameters associated with annular flow emerged, further increasing the existing database on this type of flow (ALVES, 2014). The variety of available data allowed Hewitt and Govan (1990) to present a set of correlations describing the entrainment of liquid droplets in the gas core, based on 2354 points, from 32 sources. This model was later incorporated into the Harwell Nuclear Energy Laboratory code for the transient calculation of dried-out flows, *i.e*, flows in which the liquid film on the pipe wall disappears, causing a rapid increase in the wall temperature, provided the heat flow is kept constant.

Investigations regarding annular flow continued over the next century. Wolf *et al.* (2001) conducted an experimental study in a pipe with 10.8 [m] long and 31.8 [mm] in diameter, to evaluate the flow behavior for different fractions of liquid and gas at the inlet. The results showed that the annular pattern, in general, requires a significant length to become fully developed. The flow and the average thickness of the film, for example, showed considerable variations for distances between 100 and 300 tube diameters in high fractions of liquid at the inlet. In addition, the pressure gradient continued to change for all flows tested, even after a distance of 100 pipe diameters, a fact attributed to a great pressure drop in the studied conditions, caused by gravitational forces.

Okawa and Kataoka (2005) presented new empirical correlations for the rate of entrainment and droplet deposition in the annular air-water flow, elaborated from experimental data and models available in the literature. To correlate the entrainment rate, the authors used the ratio between the interfacial shear force and the surface tension force in the liquid film as a scale parameter for the experimental data used. The deposition rate was correlated by taking the superficial velocity of the gas phase as a reference at low droplet concentrations, while for high concentrations the amount of drops itself was the factor of greatest influence. The model showed good agreement with the data bank regarding the annular flow of steam and water at high pressure.

Aliyu *et al.* (2017) developed a model to predict the interfacial friction between the gas and liquid phases, through measurements of the pressure gradient and the thickness of the film in the annular flow. The experiments were performed on a 101.6 [mm] internal diameter pipe, since most of the studies available in the literature are relevant only for small diameters between 10 and 50 [mm]. The gas superficial velocity ranged from 11 to 29 [m/s], and the superficial velocity of the liquid from 0.1 to 1 [m/s]. The results were compared with experimental data obtained in different flow conditions and tube sizes, thus making it possible to create a correlation for interfacial friction with a maximum absolute mean error of 28.1%.

Lin *et al.* (2020) conducted experiments based on image analyses to detect the characteristics and the space-time evolution of the interfacial waves present in the annular flow. The test rig consisted of a tube measuring 5.5 [m] in length and 20 [mm] in diameter, made of transparent acrylic. The liquid and gas superficial velocities were kept in an interval between 0.07 to 0.71 [m/s] and 7.64 to 30.82 [m/s], respectively. To produce the images, a high-speed FR-625 camera with 100 [mm] lenses was used, and the shooting frequency was adjusted to 500 [fps]. The results showed the existence of three types of interfacial waves, with different frequencies and velocities, that play a dominant role in the pressure gradient. In addition, the authors found that the orientation of these waves was directly related to the identification of the flow pattern. The schematic diagram of experimental apparatus used by the authors is shown in Figure 2.

Figure 2 – Test facility used in the experiments of Lin *et al.* (2020).

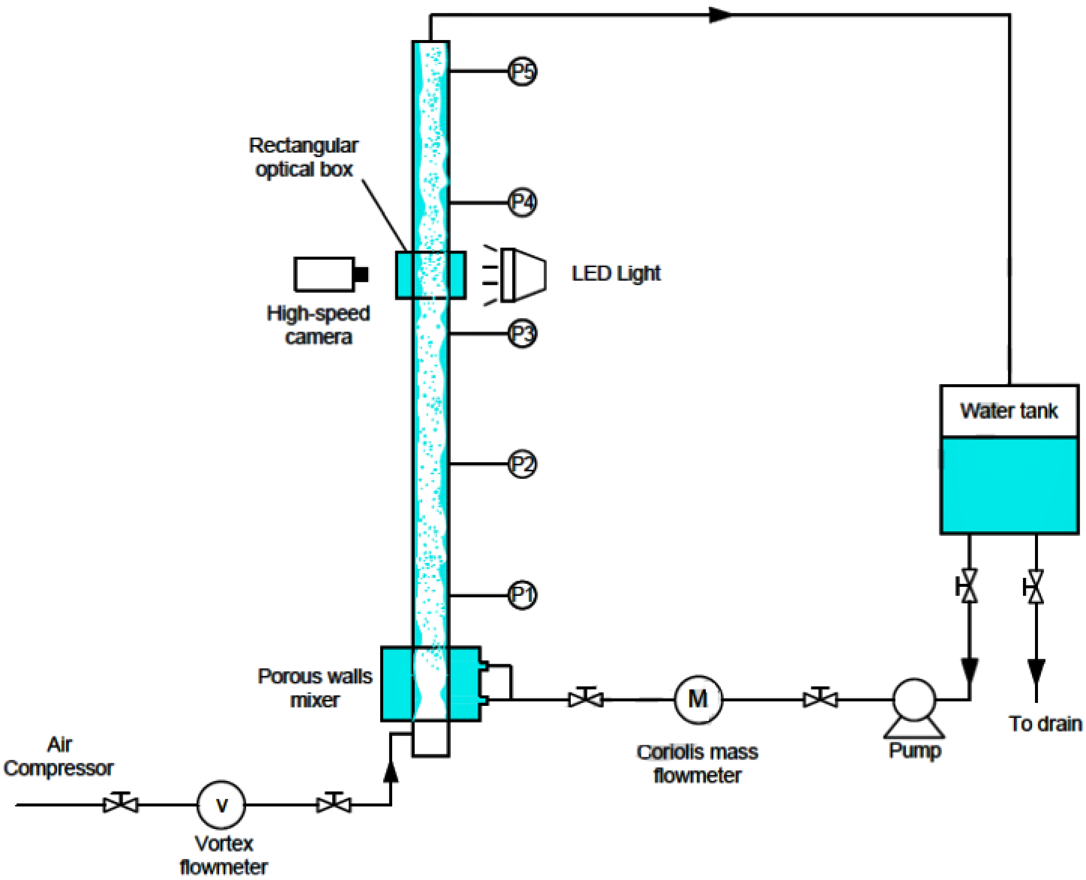

Source: Lin *et al.* (2020).

2.2.2 Churn Flow

Among all the flow patterns mentioned in section 2.2, churn flow is certainly the most complex and the least understood. This is because it is a highly unstable and disturbed flow regime, in which the movement of the liquid film tends to be oscillatory and not periodic, with upward and downward behaviors. In churn flow, the elongated bubbles known as Taylor bubbles are no longer present since they collapse because of the high gas fraction in the mixture.

The unstable nature of this flow pattern has often made it be considered only a transitional regime, which according to Barbosa *et al.* (2001a) originates from the fact that the word "churn" was used by several researchers to describe flow regimes that were not completely understood. In addition, the number of models and experiments available in the literature about churn flow are significantly smaller when compared to annular flow, which makes it even more difficult to predict their occurrence.

A good example is the work developed by McQuillan and Whalley (1985) to investigate the gas-liquid flow patterns that occur in vertical pipes. The authors modeled the transition between the slug and the churn patterns, and modified the equation proposed by Taitel *et al.* (1980) to determine the stability of the bubble flow, in addition to presenting a new stability criterion for the annular pattern. The equations were combined, allowing the obtention of a flow transition map which was compared with the experimental data available at the time. The success rate in predicting churn flow was only 36%, whereas for other flow regimes the success rate was over 80%.

Dukler and Taitel (1986) carried out experiments for slug and for churn flows in a pipe of 0.025 and 0.05 [m] in diameter. The authors considered that churn flow was just a phenomenon that occurred at the inlet of the pipe, as part of the process of stabilizing the slug flow. In the view of these researchers, Taylor bubbles were formed together with small unstable pistons in the liquid and gas inlet section. As the small pistons were unstable, they soon collapsed, forming larger pistons that would cause slug flow.

Barbosa *et al.* (2001) investigated the churn flow behavior through a series of experiments in a vertical pipe flowing an air and water mixture. The pipe inlet was purposely built with a transparent material to allow the visualization of the flow, which was recorded with high speed cameras. The formation of large waves, characteristics of the churn flow, were analyzed by the authors through the recordings, and thus the frequency of the waves could be determined. The results found were, in general, consistent with those proposed by Hewitt *et al.* (1985), and other parameters such as velocity and distance traveled by the waves were estimated through mathematical modeling performed on the forces acting on the waves. The test facility used by the authors is shown in Figure 3.

Sawai *et al.* (2004) analyzed the oscillatory movement of the liquid in the churn flow, and its effects on the pressure gradient, through experiments carried out in a vertical test tube of 25.8 [mm] internal diameter, with air and water as working fluids. The researchers performed joint measurements of the pressure drop and the interface structure and compared them with

Figure 3 – Test facility used in the experiments of Barbosa *et al.* (2001).

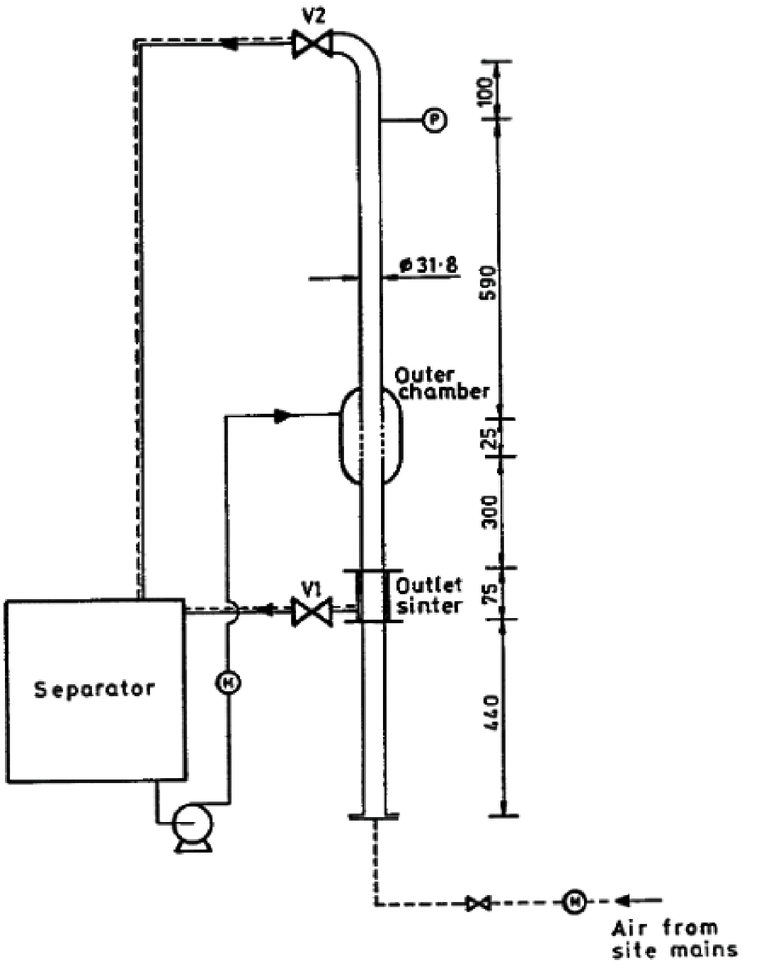

Source: Barbosa *et al.* (2001).

conventional literature correlations for two-phase flows. It was found that the pressure gradient measured in the churn flow was much higher than that predicted by the correlations, especially under conditions of low liquid flow. As the liquid flow decreased, the wave velocity became much higher than the average liquid velocity, indicating that the pressure gradient was mostly influenced by the propagation of the waves.

Wang *et al.* (2017) examined the droplets entrainment for a gas-liquid flow in the churn pattern, through experiments in a 19 [mm] internal diameter pipe, under atmospheric pressure. The authors positioned a Nikon D700 digital camera with special lenses at the tube outlet to produce high resolution images of the drops dragged from the oscillatory film. To prevent the camera lenses from becoming fuzzy, the apparatus had a side fan that directed the drops to a water collector. The obtained images suggested a large number of droplets dragged in the churn flow, which gradually decreased as the gas velocity increased and approached the transition to annular flow, where it passed through a minimum point. In addition, the diameter of the droplets dragged from the film was estimated by using a density and size probability function and comparing with the existing correlations. The test facility used by the authors is shown in

Figure 4.

Figure 4 – Test facility used in the experiments of Wang *et al.* (2017).

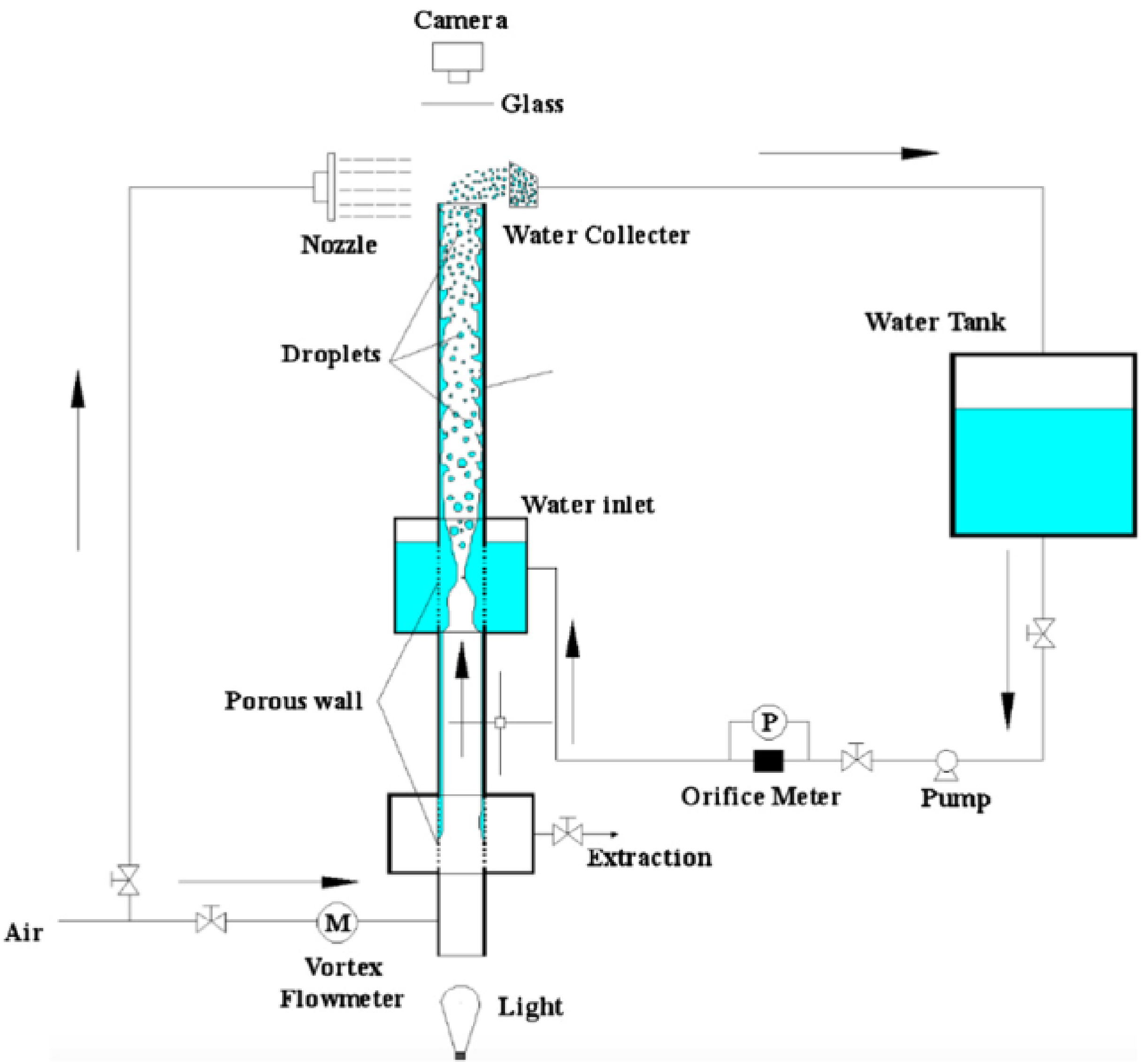

Source: Wang *et al.* (2017).

Zhang *et al.* (2019) conducted experiments in 3.7 [m] long transparent pipe, with 0.05 [m] internal diameter and 3 [mm] thickness, to analyze the entrainment of droplets in churn and annular flows. Using a high-speed camera, the authors verified the existence of different forms of droplet entrainment, which may be related to waves of great amplitude, to the interfacial shear stress, or to the rupture of gas bubbles. The results found indicated that the gas velocity is predominant in the droplet entrainment process, since it determines the entrainment process and the initial velocity of the entrained droplets. On the other hand, the velocity of the liquid has little influence, and its effects can be neglected.

2.2.3 Churn-Annular Transition

The transition mechanisms involving the flow patterns in slug, churn, and annular are closely related to the flooding and flow reversal phenomena. Thus, it is necessary to discuss them for a complete understanding of the flow regimes and their transitions. Figure 5 illustrates the case presented by Hewitt and Hall-Taylor (1970), which considers a vertical pipe where the gas is inserted at the base of the pipe, and flows countercurrent to a liquid film that is injected through the tube sides (Figure 5.a).

Figure 5 – Flooding and flow reversal.

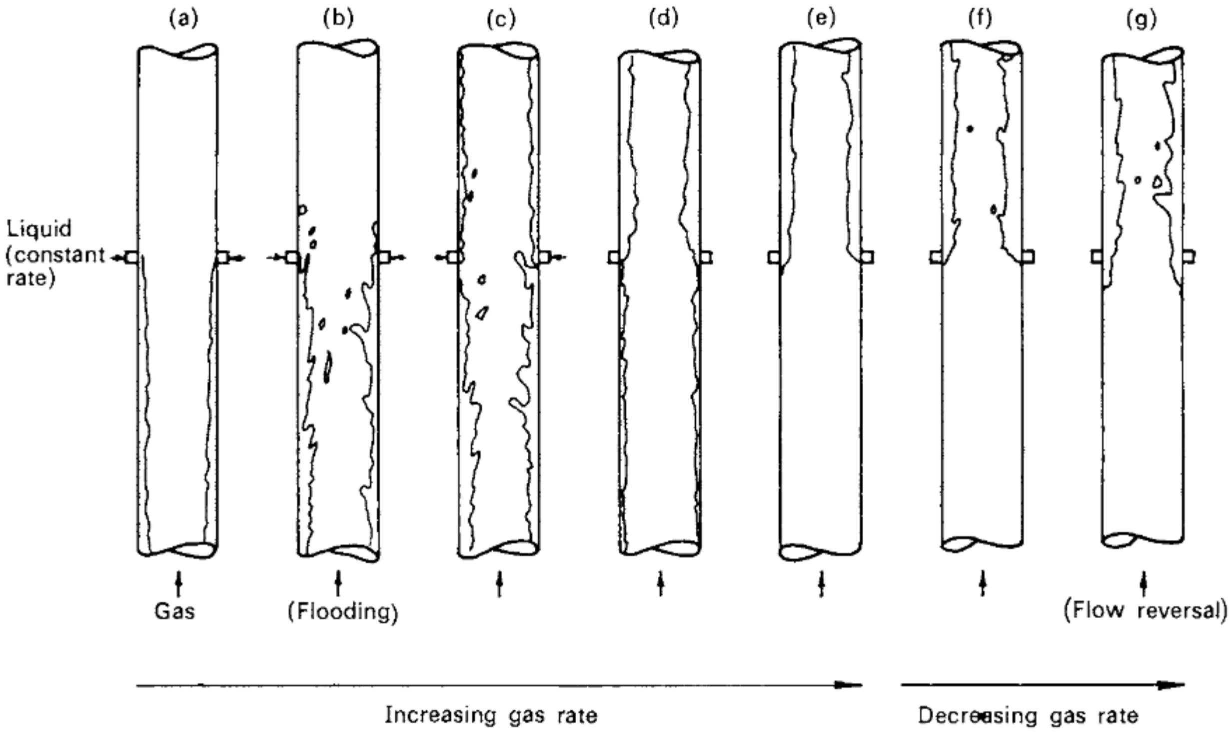

Source: Hewitt and Hall-Taylor (1970).

As the gas rate increases, the liquid film begins to show oscillations that are carried by the gas phase, until the flooding occurs, *i.e*, the point at which the first liquid droplet is transported above the injector (Figure 5.b) . After the flooding, the liquid exhibits an upward and downward behavior concomitantly inside the tube (Figure 5.c,d), until an even greater increase in gas velocity causes the liquid to be transported upwards only (Figure 5.e). With a further reduction in the gas velocity, the flow reaches a point at which the liquid film, in addition to flowing upwards, starts to descend below the liquid injection point. This latter phenomenon is known as the flow reversal.

The churn-annular transition is mainly related to the flow reversal mechanism described above. Concurrent annular flow occurs when the velocity of the gas phase is above the reversal velocity. However, depending on the geometry used to introduce the fluids into the pipeline, it is possible to obtain the annular flow at slightly different velocities (HEWITT AND HALL-

TAYLOR, 1970). According to Barbosa Jr. (2010), because it is an easily detectable phenomenon, flow reversal is the most used parameter to characterize the transition between churn and annular patterns.

Based on the correlation of Hewitt and Wallis (1963) for the flooding phenomenon, Wallis (1969) proposed the flow reversal criterion given by Equation 2.10:

$$\sqrt{j_g^*} + m\sqrt{j_l^*} \approx C \tag{2.10}$$

where m and C are constants that vary with the tube geometry. j_g^* and j_l^* represent the dimensionless superficial velocities of gas and liquid, and can be obtained by Equations 2.11 and 2.12, respectively:

$$j_g^* = j_g \sqrt{\frac{\rho_g}{gD\left(\rho_l - \rho_g\right)}} \tag{2.11}$$

$$j_l^* = j_l \sqrt{\frac{\rho_l}{gD\left(\rho_l - \rho_g\right)}} \tag{2.12}$$

where j_g and j_l are the gas and liquid superficial velocities, ρ_g and ρ_l are the gas and liquid densities, g is the gravitational acceleration and D is the pipe hydraulic diameter.

Still, Wallis (1961) established that for a traditional pipeline, at the point of flow reversal, the dimensionless gas superficial velocity is given by Equation 2.13:

$$j_g^* \approx 1 \tag{2.13}$$

however, McQuillan (1985) presented several intervals in his work where the flow reversal point might occur, which was emphasized by the work of Govan *et al.* (1991).

Another way to identify the churn-annular transition is by analyzing the pressure gradient. According to Owen (1986), in the churn flow pattern, the flooding waves are intensely present, and as the gas velocity increases, they tend to disappear. The disappearance of these waves causes a drop in the pressure gradient, which passes through a minimum point in the transition region and rises gradually when approaching the annular flow. Figure 6 presents data of the dimensionless pressure gradient plotted against the dimensionless gas flow rate, for all flow patterns present in a vertical pipe.

The average interfacial shear stress on the wall can also be used as a transition criterion, since it assumes positive values when the flow in the film is entirely in the upward direction, and negative values when part of the flow in the film is downward. Thus, the churn-annular transition occurs when the average shear stress on the wall is equal to zero, since it is positive in the annular flow and negative in the churn flow.

Figure 6 – Data for pressure gradient of a vertical pipe with fully developed air-water flow.

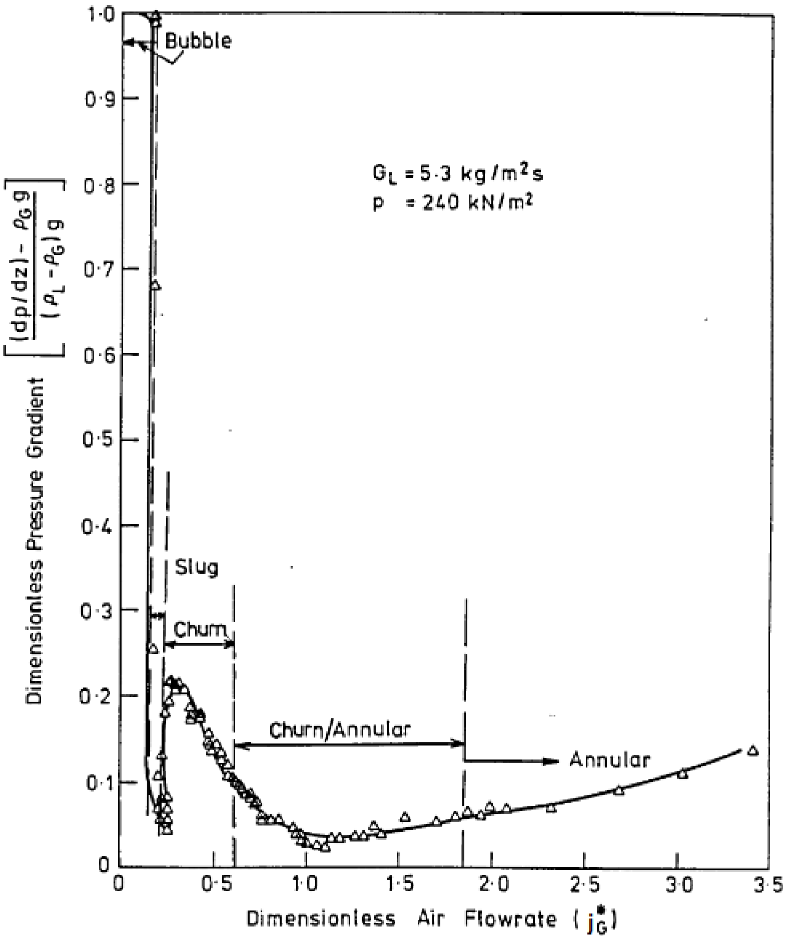

Source: Adapted from Owen (1986).

2.3 THE GOVAN *ET AL.* (1991) EXPERIMENT

This section describes in detail the experimental procedure that will be used as the main validation parameter for the numerical simulations proposed in this work. Govan *et al.* (1991) carried out experiments with air and water to investigate the flooding phenomenon and the churn flow pattern, by measuring the liquid holdup and the pressure gradient. Figure 7 illustrates the test bench used by the authors.

The flooding experiments were conducted in a vertical pipe of 32 [mm] internal diameter, with different geometries at its outlet, namely: the porous wall outlet, the tapered outlet, and the square-edged outlet. This procedure was performed to verify the influence of the output format on the flooding process, since the data presented in the literature about this phenomenon showed a large discrepancy. In this work, only the porous outlet is relevant, so this type of geometry will be the only one discussed here.

The test section was built in transparent acrylic resin (to allow visualization of the flooding point), and copper. The air and water flows were measured through an orifice plate and

Figure 7 – Illustration of the experiment rig used by Govan *et al.* (1991)

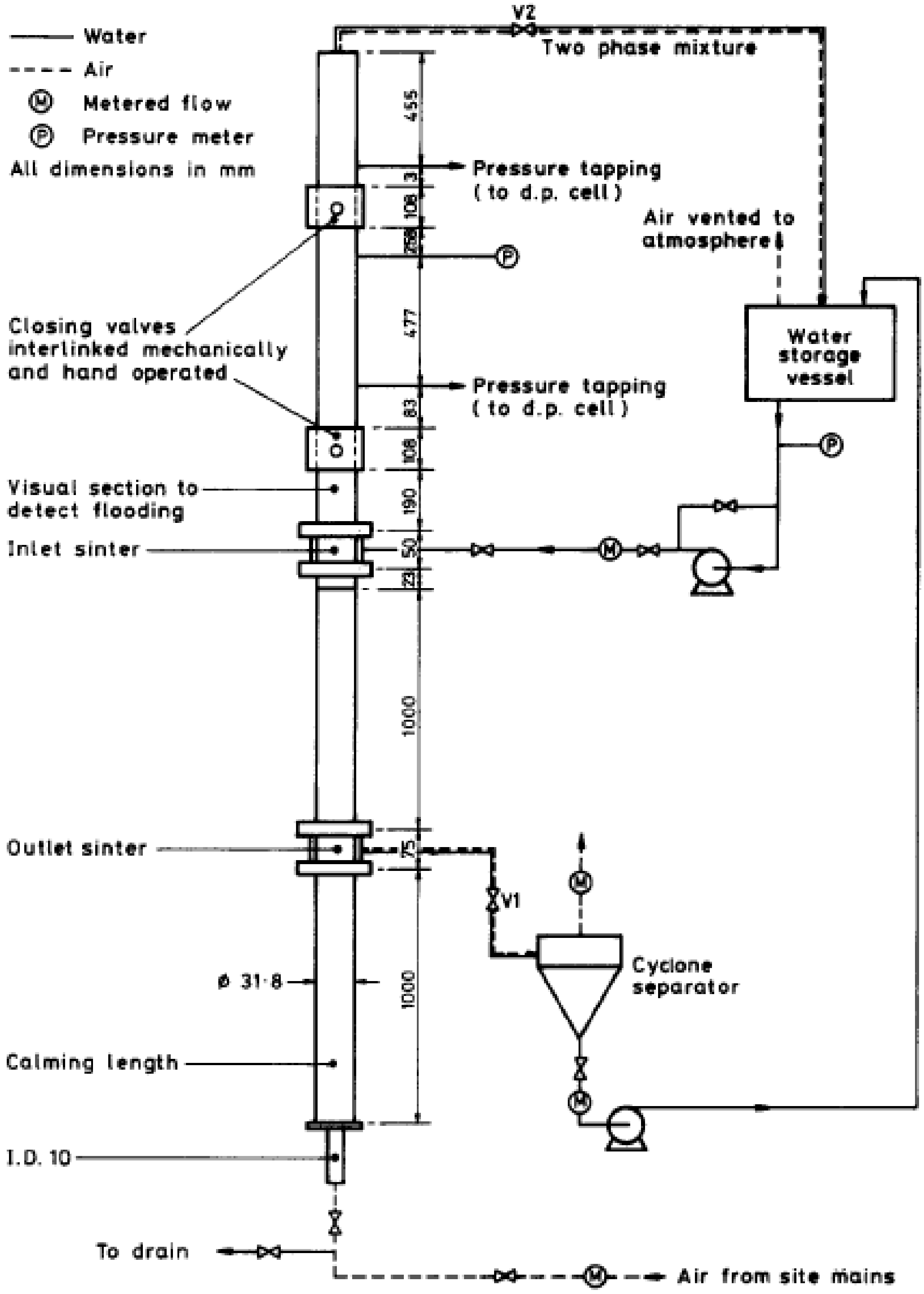

Source: Govan *et al.* (1991).

calibrated rotameters, respectively. The air pressure at the pipe outlet was maintained at 1.33 [bar] through the V2 valve in all experiments, and the temperature was maintained at 20 [^{o}C]. The air passing through the test rig was separated from the liquid by a cyclonic separator and, after separation, it was discarded in the atmosphere while the liquid phase was returned to a storage tank.

The liquid phase was injected into the test section through an inlet sinter, and before the flooding point occurred it left the pipeline through the outlet sinter, located at the bottom of the apparatus. After flooding, part of the liquid phase flowed above the injection point, giving rise to churn flow, and part flowed downwards. The air was introduced into the apparatus through a 10 [mm] diameter section, which avoided water drainage, and passed through a stabilizing section of 1 [m]. Also, the V1 valve was inserted to minimize the effects of air loss at the inlet.

Two distinct cases were analyzed in the experiments conducted for churn flow: the case where there was a falling liquid film, and the case where this film did not exist. For the situation in which there is a descending film, the rig configuration was the same used in the flooding experiments and, for the case without the film, the water could be injected by both the lower and the upper sinter, which allowed the analysis of the development length as it resulted in two different test sections.

To measure the liquid holdup, two simultaneous shut-off valves were installed on the rig positioned 0.92 [m] apart. In such a way, the water contained in the section between the valves was drained into a measuring cylinder. The pressure gradient was obtained by using two pressure tappings positioned 846 [mm] apart. Because of the unstable and oscillatory nature of the churn flow, the results found showed large fluctuations, and to obtain an average value the results had to be smoothen. The maximum uncertainty of the pressure gradient was estimated at 60 $[N/m^3]$ for the churn flow and 15 $[N/m^3]$ for the churn-annular transition region, where the number of fluctuations is smaller.

2.4 NUMERICAL MODELS

As presented in the previous subsections, the amount of work on annular and churn flows is noteworthy. However, most of these studies are experimental and are limited to empirical correlations for the entrainment and droplet deposition rates, and to one-dimensional models for calculating the phase fractions and the pressure gradient in steady state.

The advancement of Computational Fluid Dynamics (CFD) was driven, among other factors, by the high cost of the experimental apparatuses used in the reproduction of two-phase liquid-gas flows. Thus, numerical simulations have been widely employed in recent years, as they are a cheaper alternative for predicting fluid behavior when compared to test sections, since many of the software available on the market is free. The following subsections will discuss some CFD methodologies for two-phase flows and some works developed in recent years.

2.4.1 Eulerian and Lagrangian Descriptions

Most analyses of computational fluid mechanics are based on the fluid particle model, which allows representing a fluid through discrete particles. There are two ways to reference a fluid particle system: through Eulerian or Lagrangian approaches.

In the Eulerian approach, the coordinate system is fixed, that is, the properties of the fluid are calculated in a space position (x, y, z), at time t (SOUSA E LIMA, 2008). According to Santiago (2007), an Eulerian computational mesh is composed of a set of discrete points, for which the transport equations are solved, by means of algebraic equations which are approximations of the the partial differential equations that govern the system. In this type of description, dynamic boundary conditions of velocity and pressure are used to include the effects of particle motion in the model, since the computational mesh is fixed (NOTELO, 2010). For Charles *et al.* (2009), the Eulerian model may present large oscillations in the solution of some advection-diffusion problems, since the method is sensitive to numerical diffusion because of the approximation adopted in the resolution of the differential equations.

In the Lagrangian description the fluid particles are followed individually at each instant of time, and it is possible to establish an equation for the trajectory of each particle throughout the numerical integration of the ordinary differential equations that describe its movement (WOLK, 2003). In Lagrangian models, the computational mesh moves along with the flow, so it is necessary to recalculate the position of the mesh elements whenever there is an advance in time (NOLETO, 2010). According to Spivakovskaya *et al.* (2007), the Lagrangian formulation is efficient in solving advection problems, since it can eliminate the effects of numeric diffusion, but it requires a great computational effort in cases where many particles are included in the model, which makes its application unfeasible. In addition, fluid particles may eventually collide with each other, making it even more difficult to model this type of problem.

When modeling liquid-gas flows, the gas phase can be referenced by either the Eulerian or the Lagrangian descriptions. The Eulerian application may require less computational effort when analyzing the characteristics of the gas at fixed points in space. On the other hand, if the number of gas particles is scarce, the Lagrangian description must present results that are more accurate and free from numerical oscillations. Thus, flows with more than one phase can present the formulations called Eulerian-Eulerian, and Eulerian-Lagrangian, depending on the description used in the dispersed phase (SIVIER *et al.*, 1993).

In the Eulerian-Eulerian description, the liquid and gas phases are treated individually as a continuous medium and, for this reason, this method is known as a two-fluid model. The equations of conservation of mass and amount of movement are used to include the temporal character in the model. Moreover, additional equations are needed to describe the momentum transfer between the phases, and the turbulence. Despite requiring less computational effort when compared to the Eulerian-Lagrangian approach, the use of this methodology may not describe the flow in detail, since the discrete information of the dispersed phase is lost when averaging the equations in each computational cell. This occurs because one of the hypotheses of the two-fluid model is that the fluid is continuous and fills the entire computational domain (TOCCI, 2016). Despite this problem, the Eulerian-Eulerian method continues to present the most consistent results when it comes to the reality of the dispersed flows.

In the Eulerian-Lagrangian approach, the continuous phase is described by the Eulerian formalism, and the dispersed phase is modeled on Lagrangian references. The average equations are solved for the continuous phase, while the movement of the discrete particles is described through known equations of fluid dynamics. The trajectories can be traced within the studied control volume. In this method, closure relationships are also needed to compute the interfacial forces.

2.4.2 Interface-Tracking and Interface-Capturing

The interface capture and tracking models are CFD methods widely used to find the interface in flows with more than one phase. According to Tezduyar (2006), interface tracking methods require meshes that can track the interface, so the mesh needs to be updated whenever the flow evolves. The conservation equations are solved for each of the phases and are coupled throughout the interface, which can suffer only moderate deformations. Also, the phases are solved individually in their own meshes that can deform according to the interface movement (TOCCI, 2016).

The interface capture methods are based on fixed spatial domains where a scalar function is used to capture the interface. The Volume of Fluid Method (VOF) is an interface capture method, which is capable of including coalescence phenomena in the interface. According to Tocci (2016), in the VOF method the scaling function works as an indicator and corresponds to the volume fraction occupied in each cell, which can vary between one (fluid 1) and zero (fluid 2). Thus, when the indicator function assumes values other than one and zero, it means that the algorithm is capturing the flow interface. A schematic interface is shown in Figure 8, where the border between two fluids is represented by the solid blue line and the numbers indicate the volumetric fraction of each cell.

The choice of CFD models depends on the nature of the problem studied. The Eulerian-Eulerian formulation is sensitive to numerical oscillations, and there may be a loss of information when simulating the dispersed phases. In the Eulerian-Lagrangian description, the simulation can eliminate the effects of numerical diffusion. However, this approach quickly becomes prohibitive as the number of particles involved in the flow increases. The methods of tracking and capturing the interface can also require great computational effort, so the VOF method is employed when the interface capture is essential.

Figure 8 – The volume of fluid technique for capturing the free surface interface.

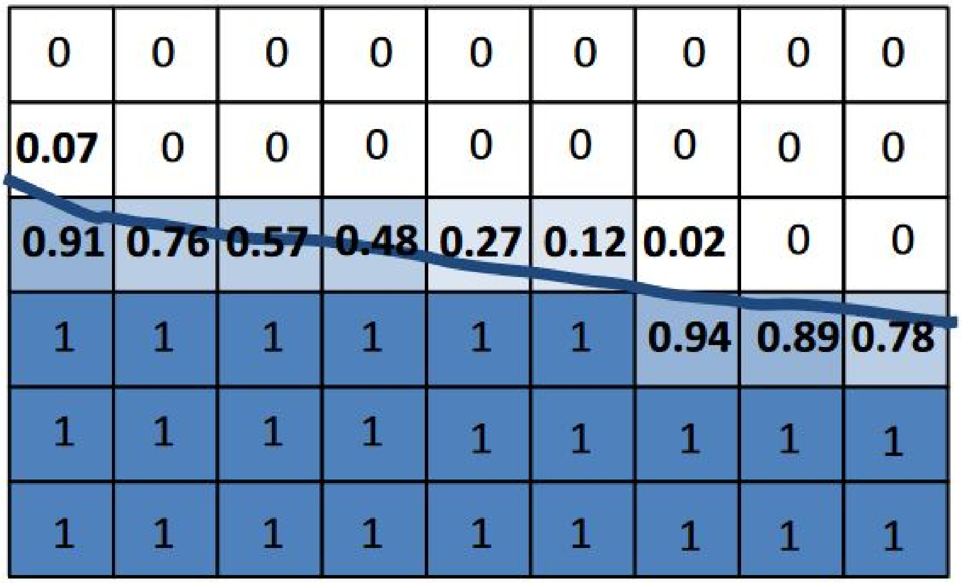

Source: Davidson *et al.* (2015).

2.4.3 State of the Art

Da Riva and Del Col (2009) used the commercial code ANSYS-Fluent to simulate air-water and vapor-liquid flow R134a in the churn pattern, under adiabatic and transient conditions, through the volume of fluid method (VOF). The simulations were performed with different values for the liquid and gas superficial velocities and with different pipe diameters, in order to analyze the influence of these parameters on the liquid-gas interface. In air-water simulations, the authors observed a strong effect of the liquid superficial velocity on the formation of the flooding waves: the higher the liquid flow, the more frequent the waves, and the liquid film adjacent to the wall became more disturbed and thicker. In the simulations performed with liquid-vapor R134a, in addition to the large amplitude flooding waves, smaller waves were identified, which was attributed to the fact that the surface tension between the liquid-vapor R134a was lower when compared to the air-water mixture.

Liu *et al.* (2011) presented a new two-fluid CFD model to investigate concurrent annular flow in vertical pipelines through commercial ANSYS-Fluent software. In order to predict the flow in the liquid film, in the gas core and the interaction between the phases, the model solves the transient equations of mass and momentum conservation for the film and gas core regions. In this model, the impact of the entrainment of liquid droplets in the gas core is not considered because of the assumed hypothesis that the gas core is homogeneous. However, the impact of the entrainment in the flow is, in some way, considered in the interfacial positions through the source terms of the moment equations, turbulent kinetic energy, turbulent dissipation, and other governing equations. The predictions made using this method, provided good agreement with the experimental data.

Thaker and Banerjee (2013) conducted numerical simulations to investigate the interfacial behavior of different air-water flow patterns in horizontal pipes. The three-dimensional simulations were performed with the aid of the commercial OpenFOAM software, and its native `interFoam` algorithm. The VOF method was used to track the air-water interfaces in a 1.5 [m] long and 10 [mm] internal diameter pipe for various Reynolds numbers. The numerically captured flow patterns were in line with what is available in the literature, which reinforced the idea that OpenFOAM is able to predict and capture the phenomena of bubble generation, growth and collapse.

Karami *et al.* (2014) developed numerical and experimental studies in a horizontal piping of 0.15 [m] diameter, with low fractions of liquid. The simulations occurred under conditions similar to those experimentally tested, and the commercial ANSYS-Fluent software was used together with the multiphase VOF model to obtain important parameters of the two-phase flow such as: the interface format, the velocity fields of the liquid and gaseous phases, the liquid holdup, and the shear stress. The authors tested three different mesh sizes. However, the phenomenon of liquid entrainment could not be verified through simulations, since to capture its effects an extremely thin mesh is required and, consequently, a very high simulation time. The results found in the simulations were in agreement with the experimental data.

Qiu *et al.* (2014) used the VOF model, within the commercial ANSYS-Fluent software, to conduct transient and three-dimensional simulations of heat transfer and flow during a wet steam condensation process in vertical ducts of 12 [mm] in diameter and 4 [m] in length. The effects of gravity and surface stresses were considered in the model, and a uniform heat flow of q = 25 $[kw/m^2]$ through the wall was used as a boundary condition for the problem. The bubble, slug, churn, and annular flow patterns were investigated, and the flow values found in the simulations were in accordance with the flow pattern map, proposed by Hewitt (1969). In addition, the simulated heat transfer coefficients also showed a good consistency when compared with the correlations developed by Boyko-Kruzhilin's (1967).

Parsi *et al.* (2016) used a hybrid model with Eulerian descriptions (Eulerian-Eulerian) coupled with the VOF method available in the ANSYS-Fluent software to study churn flow. The simulated geometry consisted of an elbow of 76.2 [mm] of internal diameter and 1.5 of curvature radius, with 3 [m] of length in the vertical and 1.9 [m] in the horizontal. The superficial velocities of the gas and liquid varied so that the churn flow and the transition to the annular pattern were considered in the simulation. The results found were consistent with data in the literature, which indicated that the hybrid approach was efficient in simulating regions with larger scales through VOF, and in capturing the effects of smaller scale through Eulerian analysis.

Tekavčič *et al.* (2019) conducted numerical simulations using the native `interFoam` algorithm, available in the commercial OpenFOAM software, to investigate the frequency of large amplitude waves, formed by the high gas fraction in the churn flow pattern. A three-dimensional model with isothermal conditions was implemented for two pipes containing air and water, of 19 and 32 [mm] internal diameter, in order to reproduce the experiments developed by Barbosa

Jr. *et al.* (2001) and by Wang *et al.* (2013). In addition, the authors performed a study of the sensitivity of the mesh used, testing four different meshes ranging from thousands to millions of computational cells. The results obtained for the frequency and amplitude of the waves were consistent with the experimental data analyzed.

Pham *et al.* (2020) used the commercial OpenFoam software to conduct simulations using the two-fluid and VOF models in order to make a quantitative comparison between them. The authors simulated the traditional bubble flow, and a particular case with a single bubble in the tube, with a diameter much smaller than that of the grid cell. For the traditional bubble flow, the two-fluid model presented a good prediction of gas and liquid velocities, while the VOF method presented a lower accuracy in the flow description even after being coupled to a Lagrangian discrete bubble model (DBM) to simulate the cases where the bubble size was smaller than the mesh cell. For the case with the single bubble in the tube, the two-fluid model presented poorer results and was less effective than the VOF method in predicting kinematic parameters and flow dynamics. The authors made a series of considerations about the applicability of the two-fluid and VOF models in dispersed and segregated flows.

2.5 HYTAF (HYPERBOLIC TRANSIENT ANNULAR FLOW)

This section briefly describes the works developed by Alves (2014) and Alves *et al.* (2017) that will be used as one of the validation parameters for the numerical simulation proposed in this dissertation.

Alves (2014) and Alves *et al.* (2017) developed a numerical code to investigate the churn and annular flows, as well as the transition between them. A hyperbolic and transient model called HyTAF (Hyperbolic Transient Annular Flow) was built and the hyperbolic balance equations for mass, momentum and entropy were written for the liquid and gas phases. In addition, the authors used closure equations available in the literature to find interfacial friction and entrainment rates. The finite difference method was used to discretize the governing equations with a second order approximation for space and a first order approximation for time. To deal with sudden variations in the space-time domains, the coefficient matrix splitting method was implemented.

The results found were compared with experimental data in steady and transient state. More than eight literature sources were used for the steady state comparison, providing more than 1500 data points for the pressure gradient, film flow rate and void fraction. The average deviation between the model and the data was around 17% for the pressure gradient and 5.8% for the void fraction. For the transient case, a simulation in a vertical tube with 42 [mm] in length and 49 [mm] in internal diameter was conducted. The authors obtained good results with the transient model, and the average deviation was around 14.5% for the pressure gradient and 7.9% for the liquid holdup.

3 NUMERICAL METHODOLOGY

In this chapter, the hybrid approach used in the simulations is discussed. The system's governing equations are presented, and they consist of the continuity equation, the momentum equation, and the relations for the drag forces and for the surface tension. In addition, a purely advective equation to capture the interface between the phases is presented. The turbulence models used in the simulation are also discussed, and the Courant criteria to control the time step of the simulations is defined. Also, the numerical procedure is briefly commented, the main OpenFoam directories are presented, and the operation of the `multiphaseEulerFoam` and PISO algorithms are presented in the form of flowcharts. Finally, the discretization method used in the equations is presented, and a correction in the original `multiphaseEulerFoam` algorithm for the surface tension is made.

3.1 HYBRID APPROACH

This work aims to investigate parameters associated with annular and churn flow patterns, as well the transition between them, through transient and three-dimensional simulations. As presented in Chapter 2, the topology of these flow patterns has characteristics of segregated and dispersed flows at the same time.

According to Tocci (2016), for dispersed flows, the use of the two-fluid model is indicated in cases where the interface size is smaller than the numeric grid cell. In this model, each fluid must behave as a continuum and must fill the entire computational domain, causing a loss of information during the averaging process that can be mitigated through auxiliary closure relationships. On the other hand, interface capture methods usually fail in dispersed flows where the fluid elements are smaller than the grid cells. Therefore, these models are usually indicated to simulate segregated flows. The VOF method, specifically, is an interface capture model and is ideal for studying the effects of the liquid film on churn and annular flow patterns (PARSI *et al.*, 2016).

Thus, the best way to perform the simulations herein proposed is to use the hybrid code developed by Wardle and Weller (2013), capable of combining the characteristics of the Eulerian-Eulerian and VOF models. This algorithm is called `multiphaseEulerFoam` and is available as one of the OpenFOAM libraries. OpenFOAM (Open-source Field Operation and Manipulation) is an open-source commercial software, developed by OpenCFD Ltd in 2004. It is a simulator widely used in industries and academia, being able to solve the mechanics of the continuum, including Computational Fluid Dynamics (CFD). Its main differential in relation to most commercial programs available is that its source code (written in C ++) is open, which allows customization by its users.

3.1.1 Governing Equations

To derive the system's governing equations, it is necessary to identify the phases present in each of the computational cells studied. According to Hill (1998), it is possible to condition the local equations through the indicator function $I_k(x,t)$, described by Equation 3.1. If the phase of interest is inside the observed cell, its average conservation equations are computed, multiplying them by 1. On the other hand, if the phase of interest is not present in the cell, its effects are disregarded, and its equations are multiplied by 0. Also, according to Cerne *et al.* (2001), if there is more than one phase present in the analyzed cell, an average process based on the volume fraction of each phase is used as weighing parameter to compute the effects of the mixture.

$$I_k\left(x,t\right) = \begin{cases} 1, \text{ if } \left(x,t\right) \text{is in phase k} \\ 0, \text{ if } \left(x,t\right) \text{is not in phase k} \end{cases} \tag{3.1}$$

According to Tocci (2016), the volumetric fraction of the k-phase is defined by Equation 3.2:

$$\alpha_k = \overline{I_k\left(x,t\right)} \tag{3.2}$$

where the bar represents the averaging process.

The mathematical modeling of the studied problem consists of the continuity Equation 3.3 and the momentum Equation 3.4. They are presented below, considering the hypothesis of an incompressible three-dimensional flow, with immiscible fluids and with constant fluid properties.

$$\frac{\partial \alpha_k}{\partial t} + \vec{U}_k \cdot \nabla \alpha_k = 0 \tag{3.3}$$

$$\frac{\partial\left(\rho_k \alpha_k \vec{U}_k\right)}{\partial t} + \left(\rho_k \alpha_k \vec{U}_k \cdot \nabla\right)\vec{U}_k = \nabla \cdot \left(\mu_k \alpha_k \nabla \vec{U}_k\right) - \alpha_k \nabla P + \rho_k \alpha_k \vec{g} + \vec{F_D}_{,k} + \vec{F_S}_{,k} \tag{3.4}$$

where ρ_k is the phase *k* density, α_k indicates the volume fraction of the phase *k*, $\vec{U}_k$ represents the velocity of the phase *k*, μ_k is the phase *k* dynamic viscosity, and $\vec{g}$ is the acceleration of gravity. Drag forces and surface tension are represented by $\vec{F_D}_{,k}$ e $\vec{F_S}_{,k}$, respectively.

3.1.2 Drag Force

According to Wardle and Weller (2013), the interfacial drag force represents the resistance due to the relative movement between the phases involved, being strongly dependent on the size of the bubbles or droplets and on the velocity between the phases in the annular and churn flows. The drag force $F_{D,k}$ is defined by Equation 3.5.

$$\vec{F}_{D,k} = \alpha_c \alpha_d K\left(\vec{U}_d - \vec{U}_c\right) \tag{3.5}$$

where the subscripts c and d indicate the continuous and dispersed phases, respectively, and K can be obtained by Equation 3.6.

$$K = \frac{3}{4}\rho_c C_D \frac{\left|\vec{U}_d - \vec{U}_c\right|}{d_d} \tag{3.6}$$

The term d_d is the disperse phase diameter while the constant C_D is the drag coefficient, usually found through experimental procedures. However, in cases where it is not possible to perform experiments, a series of empirical correlations can be used to obtain this coefficient (SALLES, 2020). This work uses the Schiller and Naumann's correlation, which is part of the OpenFoam libraries. This model is composed by the Equations 3.7 and 3.8, given below:

$$C_D = \begin{cases} \frac{24\left(1+0.15Re^{0.683}\right)}{Re} & Re \leq 1000 \\ 0.44 & Re > 1000 \end{cases} \tag{3.7}$$

$$Re = \frac{d_d}{\nu_c}\left|\vec{U}_d - \vec{U}_c\right| \tag{3.8}$$

where ν_c and Re are the kinematic viscosity of the continuous phase and the Reynolds number, respectively.

According to Tocci (2016), there are two ways to calculate the drag coefficient in the `multiphaseEulerFoam`. The first is to specify which phase is the dispersed one, and the second is to independently consider both phases as dispersed and to average the values obtained, using the volumetric fraction of each phase as weighing parameter. This work uses the latter case, known as the *blended* method.

3.1.3 Surface Tension

The surface tension can be calculated through Equation 3.9, proposed by Brackbill *et al.* (1992). This model interprets the surface tension as a continuous and three-dimensional effect, and not as an interface boundary condition.

$$\vec{F_{S,k}} = \sigma\kappa\nabla\alpha \tag{3.9}$$

where σ is the surface tension coefficient between the phases, and κ is the local surface curvature, given by the Equation 3.10.

$$\kappa = -\nabla.\left(\frac{\nabla\alpha}{|\nabla\alpha|}\right) \tag{3.10}$$

It is possible to verify in Equations 3.9 and 3.10 the strong dependence on the volumetric fraction of the phases. Thus, in order for the values obtained for the surface tension to be consistent, a high precision in obtaining the volumetric fractions of the phases is necessary for the correct calculation of the surface curvature, and later calculation of the surface tension.

3.1.4 Interface Capturing

To capture the interface between the phases, as in Tocci (2016) and Salles (2020), the method proposed by Weller (2008) is used. This method consists of adding to equation 3.3 a term referring to interface compression, which originates Equation 3.11.

$$\frac{\partial \alpha_k}{\partial t} + \vec{U}_k \cdot \nabla \alpha_k + \nabla \cdot \left(\vec{U}_c \alpha_k (1 - \alpha_k) \right) = 0 \tag{3.11}$$

The term $\alpha_k (1 - \alpha_k)$ ensures that Equation 3.11 will be valid only at the interface between the two phases, where there is a mixture of phases and $0 < \alpha_k < 1$. The convective term is added to compress the free surface, and the value of the artificial interface compression velocity, U_c, is given by the Equation 3.12:

$$\vec{U}_c = C_\alpha \left| \vec{U} \right| \frac{\nabla \alpha}{|\nabla \alpha|} \tag{3.12}$$

where C_α is the interface compression ratio, and the term $\frac{\nabla \alpha}{|\nabla \alpha|}$ indicates the normal unit vector at the interface. According to Wardle and Weller (2013), the magnitude of the velocity is used, because in some cases the dispersion of the interface can occur as fast as the magnitude of the local velocity.

The main strategy to control the use of the interface compression method is through the compression coefficient, C_α. This coefficient is treated as a binary that can be turned on or off, assuming the values one and zero, respectively. When the compression coefficient is turned on, the program uses the interface compression method to capture the interface between the phases, using the VOF model. Similarly, when the compression coefficient is turned off, the program does not use the interface compression method, and the pair of phases is treated as dispersed phases that are modeled using the two-fluid method (WARDLE and WELLER, 2013; TOCCI, 2016; SALLES, 2020).

3.1.5 Turbulence

To include the turbulence effects in the simulations, OpenFOAM has a library with several turbulence models. The model used here is the $k-\omega\ SST$, which is a combination of the models $k-\varepsilon$ and $k-\omega$, responsible for calculating the turbulent kinetic energy (k) and the turbulent dissipation rate (ω) in situations far and close to the tube wall, respectively. In the transition regions between the two models ($k-\omega$ and $k-\varepsilon$) an interpolation vector is used, thus the $k-\omega\ SST$ model combines the robust advantages of the $k-\omega$ model in the sub-layer of the boundary layer with the $k-\varepsilon$ model to deal with situations away from the boundaries (WILCOX, 1998).

The $k-\omega\ SST$ model implemented in OpenFoam is a modification of the original model, proposed by Menter (1994). The equations of turbulent kinetic energy and the turbulent dissipation rate, which describe this adapted model, were proposed by Menter *et al.* (2003), and are defined below by Equations 3.13 and 3.14, respectively.

$$\frac{\partial(\rho k)}{\partial t}+\frac{\partial(\rho U_i k)}{\partial x_i}=\tilde{P}_k-\beta^*\rho k\omega+\frac{\partial}{\partial x_i}\left[(\mu+\sigma_k\mu_t)\frac{\partial k}{\partial x_i}\right] \tag{3.13}$$

$$\begin{aligned}\frac{\partial(\rho\omega)}{\partial t}+\frac{\partial(\rho U_i\omega)}{\partial x_i}&=\alpha\rho S^2-\beta\rho\omega^2+\\ &\frac{\partial}{\partial x_i}\left[(\mu+\sigma_\omega+\mu_t)\frac{\partial\omega}{\partial x_i}\right]+2(1-F_1)\rho\sigma_{\omega 2}\frac{1}{\omega}\frac{\partial k}{\partial x_i}\frac{\partial\omega}{\partial x_i}\end{aligned} \tag{3.14}$$

Analyzing Equation 3.13, the term $\frac{\partial(\rho k)}{\partial t}$ refers to the time derivative, and $\frac{\partial(\rho U_i k)}{\partial x_i}$ indicates the turbulent kinetic energy convection. The term $\tilde{P}_k$ represents production, $\beta^*\rho k\omega$ indicates dissipation, and finally, $\frac{\partial}{\partial x_i}\left[(\mu+\sigma_k\mu_t)\frac{\partial k}{\partial x_i}\right]$ indicates the diffusion of the turbulent kinetic energy. In Equation 3.14, the terms have a very similar meaning for the turbulent dissipation rate, but the term F_1 appears to indicate a coupling function between the turbulence models $k-\omega$ and $k-\varepsilon$, responsible for the smooth transition between the models. This aforementioned function is represented by the Equations 3.15, 3.16 and 3.17 given below.

$$F_1=\tanh\left(arg^4\right) \tag{3.15}$$

$$arg=\min\left[\max\left(\frac{\sqrt{k}}{\beta^*\omega y};\frac{500\nu}{y^2\omega}\right);\frac{4\rho\sigma_{\omega 2}k}{CD_{k\omega}y^2}\right] \tag{3.16}$$

$$CD_{k\omega}=\max\left(2\rho\sigma_{\omega 2}\frac{1}{\omega}\frac{\partial k}{\partial x_i}\frac{\partial\omega}{\partial x_i};10^{-10}\right) \tag{3.17}$$

The term y indicates the distance between the mesh cell and the nearest wall in the computational domain. In regions distant from the pipe wall, the term F_1 is equal to zero, and the flow is solved by the $k-\varepsilon$ model. F_1 is equal to one for regions near the pipe wall, and in these cases the flow is resolved by the $k-\omega$ model. In an intermediate region, F_1 allows a smooth transition between the two models (MENTER *et al.*, 2003). The turbulent viscosity (ν_t) is defined by Equation 3.18.

$$\nu_t=\frac{a_1 k}{\max(a_1\omega;SF_2)} \tag{3.18}$$

where S is the invariant measure of the strain rate and F_2 is a second blending function defined by Equation 3.19.

$$F_2=\tanh\left[\left[\max\left(\frac{2\sqrt{k}}{\beta^*\omega y};\frac{500\nu}{y^2\omega}\right)\right]^2\right] \tag{3.19}$$

As mentioned earlier, the term $\tilde{P}_k$ indicates the production of turbulent kinetic energy. In fact, this is a production limiting term, which is used in the model to prevent the accumulation of turbulence in regions of stagnation, and is given by the Equation 3.20.

$$P_k = \mu_t \frac{\partial U_i}{\partial x_j}\left(\frac{\partial U_i}{\partial x_j} + \frac{\partial U_j}{\partial x_i}\right) \to \tilde{P}_k = \min\left(P_k; 10\beta^* \rho k \omega\right) \tag{3.20}$$

It is possible to couple the empirical constants of the $k-\varepsilon$ and $k-\omega$ models through Equation 3.21:

$$\alpha = \alpha_1 F_1 + \alpha_2 \left(1 - F_1\right) \tag{3.21}$$

According to Menter *et al.* (2003), the empirical constants for the model are given by the Table 1.

Table 1 – Turbulence model constants.

$\beta^* = 0.09$	
$\alpha_1 = \frac{5}{9}$	$\alpha_2 = 0.44$
$\beta_1 = \frac{3}{40}$	$\beta_2 = 0.0828$
$\sigma_{k1} = 0.85$	$\sigma_{k2} = 1$
$\sigma_{\omega 1} = 0.5$	$\sigma_{\omega 2} = 0.856$

Source: Menter *et al*. (2003).

3.1.6 Time Step

An important aspect of the simulation is to ensure its convergence. This can be done through the Courant-Friedrichs-Lewy convergence criterion (CFL method). This condition establishes that the distance that any information can travel during the time interval inside the mesh must mandatorily be smaller than the distance between the elements of the mesh. The mathematical definition of the Courant number, for n degrees of freedom, is given below by Equation 3.22.

$$C_o = \Delta t \sum_{i=1}^{n} \frac{U_i}{\Delta x_i} \tag{3.22}$$

where Δt represents the time step, and Δx is the distance between the mesh cells.

This criterion sets a maximum value for the time step, in order to guarantee the convergence of the numerical solution. This is an important condition used in the resolution of explicit partial differential equations to avoid erroneous simulation results. According to Wardle and Weller (2013), to obtain good results when simulating a two-phase flow with the `multiphaseEulerFoam` algorithm, it is necessary to keep the Courant number less than or equal to 0.25. In this work, the Courant number used in all the simulations was limited to 0.005, and the maximum time step was 10^{-6}.

Beerens (2013) showed other physical parameters capable of influencing the stability and accuracy of the simulation. Surface tension can also, in some cases, restrict the time step in the simulation.

3.2 NUMERICAL PROCEDURE

3.2.1 OpenFoam Directories

After the mathematical modeling of the problem, it is necessary to feed the program with some important parameters such as: the initial and boundary conditions, information about the geometry used, the discretization and interpolation models, and the properties of the fluids. Figure 9 illustrates a scheme with the main directories typical of the OpenFOAM software. At the beginning of the simulation, there are three main folders: ‘‘`0`’’, ‘‘`constant`’’ and ‘‘`system`’’. In the ‘‘`0`’’ folder, the initial velocity and pressure conditions of the problem are inserted, while the ‘‘`constant`’’ folder contains information about the geometry used (`polyMesh/blockMeshDict`), in addition to the properties of the fluids (`transportProperties`) and the chosen turbulence model (`turbulenceProperties`). Finally, the ‘‘`system`’’ folder is related to the methods for solving the differential equations obtained in the mathematical modeling such as: the time step and Courant number (`controlDict`), the interpolation and discretization methods (`fvSchemes`) and the number of iterations and tolerances (`fvSolutions`).

Figure 9 – Main OpenFOAM directories.

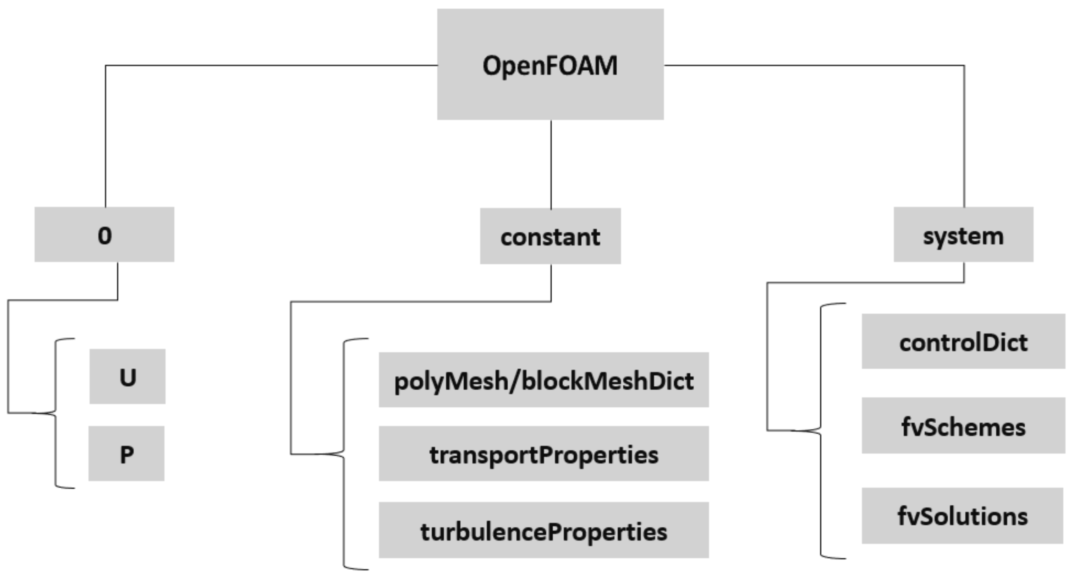

Source: Author (2021).

As the simulation progresses, new folders containing the results are created for each time interval stipulated.

3.2.2 multiphaseEulerFoam Algorithm

Figure 10 illustrates the solution procedure for the `multiphaseEulerFoam` algorithm, described by Wardle and Weller (2013). According to the authors, the first step of the simulation is to update the time interval based on the Courant number. After updating the Δt, the algorithm solves a set of coupled equations of volume fraction with the interface capturing method. Then the drag coefficients are calculated, making it possible to create an equation for the velocities of the phases that is solved for the initial values.

Finally, the Pressure Implicit with Splitting of Operators (PISO) algorithm proposed by Issa (1986) is used to solve the pressure-velocity coupling. In this algorithm, the momentum equation is solved first, and then it is possible to formulate the pressure equation giving initial estimates. Thenceforth, pressure and velocity fields are explicitly corrected. It is important to note that the PISO algorithm requires the solution to be convergent at all times and the shrinkage of the residues can be an indicator of convergence. Figure 11 illustrates the solution procedure for the PISO algorithm.

Figure 10 – `multiphaseEulerFoam` algorithm solution procedure.

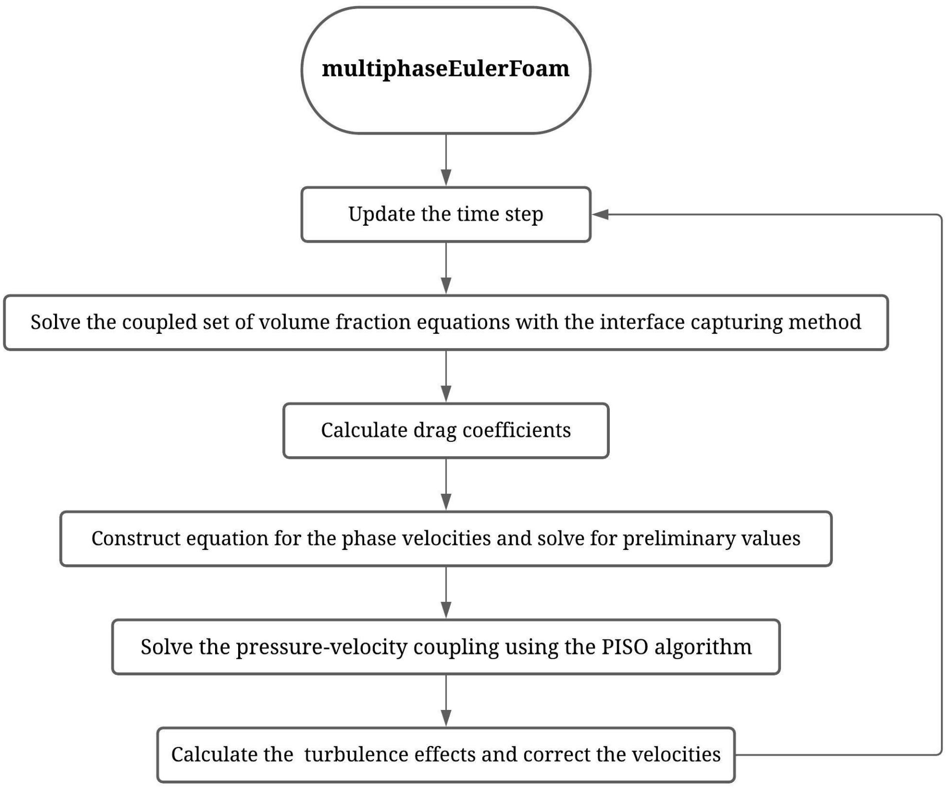

Source: Author (2021).

Figure 11 – Pressure Implicit with Splitting of Operators (PISO) algorithm solution procedure.

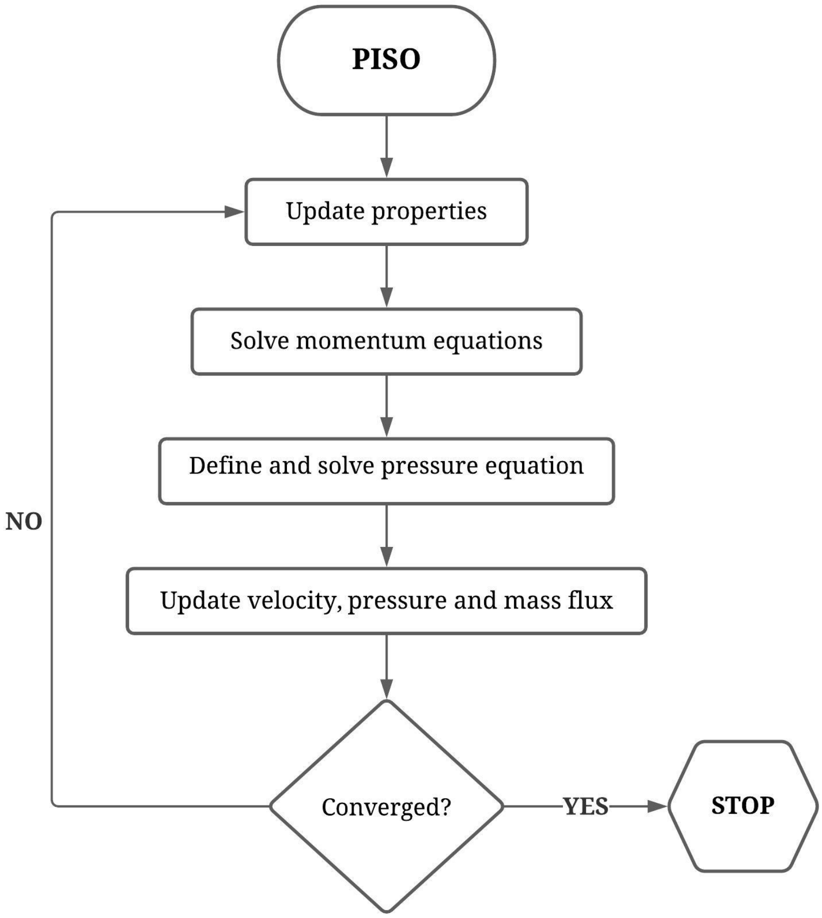

Source: Author (2021).

3.2.3 Computational Domain Discretization

To numerically solve Equations 3.3 and 3.4, it is necessary to discretize the transient, gradients, and Laplacian terms they present. To do this, the implicit Euler methods, the least squares method and the Gauss method with limited linear interpolation were used, respectively. As in Tocci (2016) and Salles (2020) the turbulent divergent, the phase fractions, and the convective terms were discretized using the limited linear Gauss, VanLeer, and limited linear Gauss V methods. All these methods have limiting functions to avoid non-physical values in the simulations.

The terms of equation 3.11 are treated with the Multidimensional Universal Limiter with Explicit Solution (MULES), which is responsible for ensuring the conservation of the phases and limiting the fraction of each one. It is extremely important that flow transport is limited, because if the flow transport is very large, it can lead to a sub-zero volume fraction in a particular cell (TOCCI, 2016).

3.2.4 Surface Tension Correction

The methodology of the present work is based on Tocci (2016) and Salles (2020). Both authors had to correct the original `multiphaseEulerFoam` algorithm because the surface tension was missing in the reconstruction of the velocity field. The version used in this work is the same used by Salles (2020) and therefore, before starting the simulations, the same corrections he had already proposed were made in the code. Figure 12 illustrates the change in the original code.

Figure 12 – Correction in the `multiphaseEulerFoam` algorithm.

```
phase.U() =
    HbyAs[phasei]
  + fvc::reconstruct
    (
        rAlphaAUfs[phasei]
       *(
          fluid.surfaceTension(phase)*mesh.magSf()
          +(phase.rho() - fvc::interpolate(rho))
          *(g & mesh.Sf())
          - ghSnGradRho
          + mSfGradp
        )
    )/phase.rho();
```

Source: Adapted from Salles (2020).

4 NUMERICAL SIMULATIONS

This chapter contains important information for conducting the simulations. First, the assumptions made for conducting the simulations are reviewed. Then, the geometry of the problem is described, and the fluids used and their properties are emphasized. The boundary conditions required to start the simulation are presented. Finally, the refinement of the meshes used in the simulation are discussed.

4.1 CHARACTERISTICS OF THE SIMULATIONS

The mathematical modeling was described throughout the previous chapter, and to simplify the equations and make the simulations feasible, some important hypotheses were assumed:

- Three-dimensional flow;
- Incompressible fluids;
- Immiscible fluids;
- The characteristics of each fluid are constant throughout the flow;
- Two-phase flow with non-reactive fluids.

In this section, some important physical characteristics necessary to describe the problem will be presented.

4.1.1 Geometry of the Problem

The geometry of the Problem was built based on the experimental rig conducted by Govan *et al.* (1991), described in section 2.3 of this work. Multiphase flows require, in general, a great computational effort to be simulated. Therefore, in this work, only one of the sections used by the authors was considered in the simulations. Nevertheless, this work is part of a larger project that is under development by the Department of Mechanical Engineering at the State University of Santa Catarina and shall be continued by the department with the complete geometry. Figure 13 illustrates the grayed-out part of Govan *et al.* (1991) rig that inspired the geometry of the simulations.

From the section chosen on the rig used by Govan *et al.* (1991), the geometry used in the simulations was built. As in the experiments, the simulations were conducted in a 1.682 [m] tube with 0.0318 [m] of internal diameter. The liquid and gaseous phases enter at the bottom of the pipe and leave the duct through the upper outlet. The liquid is introduced to induce an annular flow, with a film thickness of 0.0015 [m]. This geometry is illustrated in Figure 14.

Figure 13 – Part of Govan *et al.* (1991) experimental rig that inspired the geometry of the simulations.

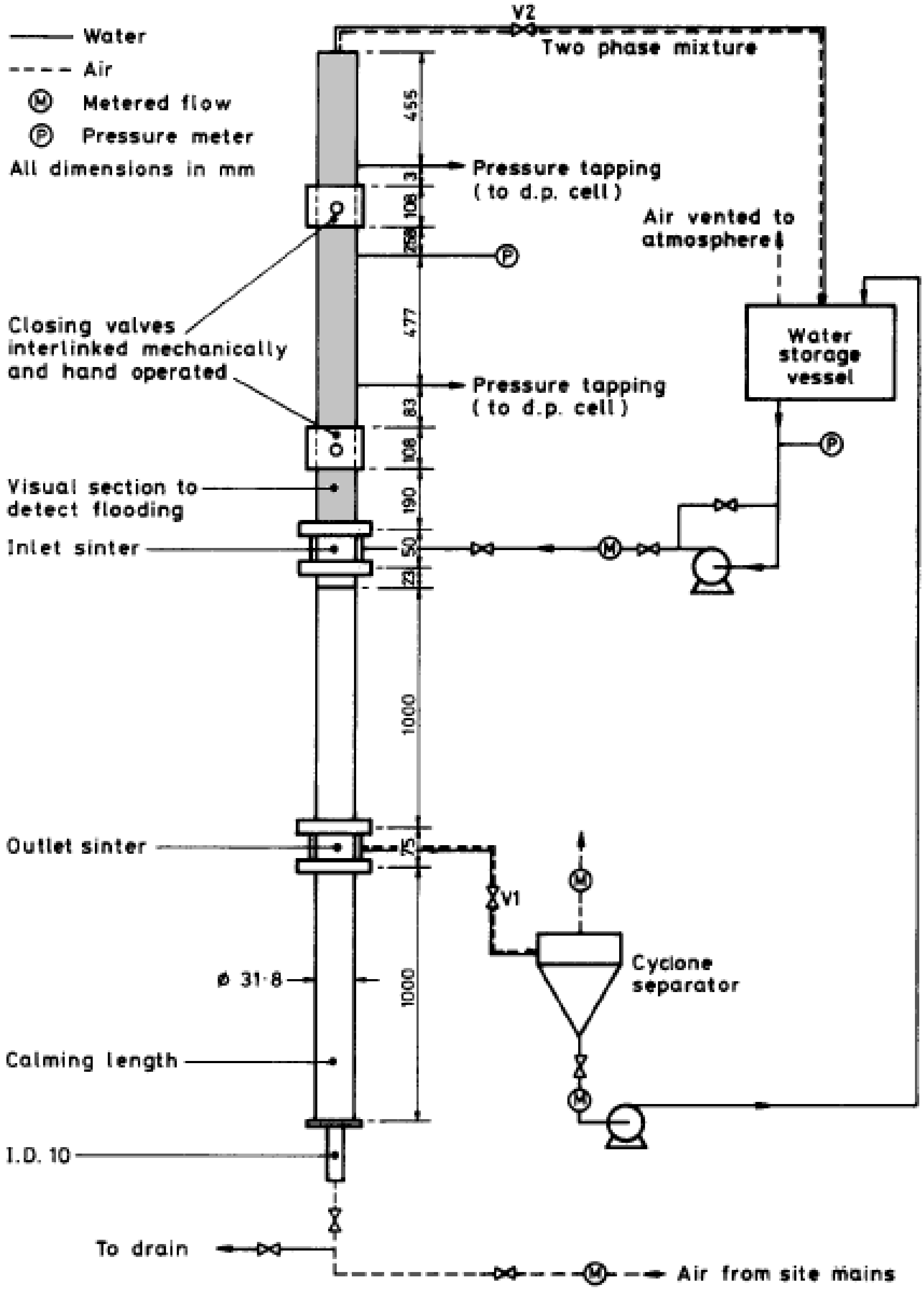

Source: Adapted from Govan *et al.* (1991).

Figure 14 – Geometry used in simulations.

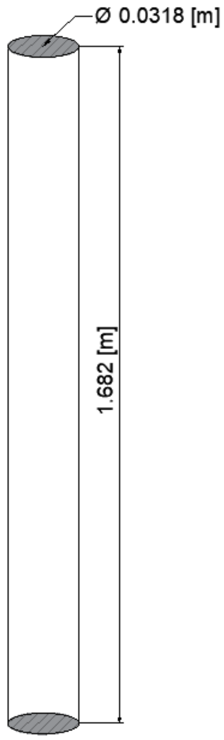

Source: Author (2021).

4.1.2 Fluids Properties

The fluids used to perform the simulations proposed in this work were the same as the ones in the experiments by Govan *et al.* (1991): water and air. The water density could be obtained directly from the tables presented in Çengel and Cimbala (2014), because it can be considered constant in relation to the pressure variation. The gas phase, on the other hand, was considered an ideal gas, and Equation 4.1 was used to find its density at a pressure of $P = 133000\,[Pa]$ and a temperature of $T = 293.15\,[K]$.

$$PV = nRT \tag{4.1}$$

where n and R are the number of moles and the universal gas constant $(8.31\,[JK.mol])$, respectively. In addition, the number of moles and density can be obtained using Equations 4.2 and 4.3 below:

$$n = \frac{m}{M} \tag{4.2}$$

where M is the molar mass,

$$\rho = \frac{m}{V} \tag{4.3}$$

then, it is possible to combine the above equations by substituting Equations 4.2 and 4.3 in 4.1, yielding in Equation 4.4:

$$\rho = \frac{PM}{RT} \tag{4.4}$$

Table 2 presents the properties of air and water used in the simulations.

Table 2 – Fluids properties obtained at $T = 293.15\,[K]$ and at $P = 133000\,[Pa]$.

	Air	**Water**
$\rho\,[kg/m^3]$	1.58	997
$\mu\,[Pa.s]$	$1.84\,x\,10^{-5}$	0.001

Source: Author (2021).

4.1.3 Boundary Conditions

To analyze the annular flow, the churn flow, and the transition region between these regimes, three points of the experiment conducted by Govan *et al.* (1991) were selected. Each point was taken from one of the aforementioned regions in order to establish the flow conditions required for entering the simulation. For the velocity field, the liquid and gas flows were provided at the pipe inlet, and the non-slip condition was used in the pipe wall. To build the pressure field, the point located at 0.858 [m] from the tube inlet was used as a reference, because in the experiments conducted by Govan *et al.* (1991), this was the point where the pressure was kept fixed at 1.330 [bar] through valve 2.

In addition, some parameters required by the $k-\omega\,SST$ turbulence model were calculated, such as turbulent kinetic energy (k), and the turbulent dissipation rate (ω). The turbulent kinetic energy at the pipe inlet was found with the aid of Equation 4.5

$$k = \frac{3}{2}\left(I\left|\vec{U_{ref}}\right|\right)^2 \tag{4.5}$$

where $\vec{U_{ref}}$ is the reference velocity and I is the turbulent intensity which according to CFD-Wiki of CFD Online can be found through the Equation 4.6:

$$I = 0.16Re^{-\frac{1}{8}} \tag{4.6}$$

At at the pipe inlet, the turbulent dissipation rate was calculated for each fluid through Equation 4.7:

$$\omega = \frac{k^{0.5}}{c_{\mu}^{\frac{1}{4}}\ell} \tag{4.7}$$

where c_μ is a constant equal to 0.09 and ℓ is the turbulent scale length which according to the ANSYS Fluent 15 manual (2013) is given by Equation 4.8:

$$\ell = 0.07D \tag{4.8}$$

Table 3 presents the boundary conditions for the cases covered in this work.

Table 3 – Boundary Conditions.

	ANNULAR		**TRANSITION**		**CHURN**	
	Air	**Water**	**Air**	**Water**	**Air**	**Water**
$\dot{m}\,[kg/s]$	$1.87\,x\,10^{-2}$	$2.53\,x\,10^{-2}$	$1.73\,x\,10^{-2}$	$2.53\,x\,10^{-2}$	$1.56\,x\,10^{-2}$	$2.43\,x\,10^{-2}$
$k\,[m^2/s^2]$	$5.98\,x\,10^{-1}$	$6.93\,x\,10^{-6}$	$5.26\,x\,10^{-1}$	$6.93\,x\,10^{-6}$	$4.35\,x\,10^{-1}$	$6.48\,x\,10^{-6}$
$\omega\,[1/2]$	$6.34\,x\,10^{+2}$	2.16	$5.95\,x\,10^{+2}$	2.16	$5.41\,x\,10^{+2}$	2.09

Source: Author (2021).

4.1.4 Mesh Analysis

According to Hernandez-Perez *et al.* (2011), the use of different mesh structures in the computational domain may imply different results. The authors investigated different structures to simulate a gas-liquid flow in cylindrical tubes using the VOF model and found a great dependence on the solution with the mesh used. The “butterfly mesh” was the one that presented the most accurate results. In this mesh, cartesian coordinates are used for the center of the tube, combined with cylindrical coordinates around it. As in Tocci (2016) and Salles (2020), this was the mesh used to perform the simulations of this work.

The simulations were performed on the computers available at the Center of Technological Sciences at the State University of Santa Catarina. Due to the large computational effort required to simulate flows with more than one phase, and considering the limitations of the processors employed, it was possible to create four different meshes: one with 15264 volumes, another with the same cross-section as the finer mesh but greater axial refining and containing a total of 30528 volumes, one with 48760 volumes, and finally one with 186560 volumes.

For the post-processing step of the data found, an OpenFOAM tool called ParaView was used. ParaView allows the visualization of flow geometry, in addition to having a series of data processing features. The data were exported to the graphic softwares Origin and Insight, which generated of the images that will be presented in this work.

5 RESULTS AND DISCUSSION

This chapter presents the results found in the numerical simulations conducted. The analyzes are performed considering only the last second of the simulations, that is, when the flow is already in steady state. The annular flow, the churn flow, and the transition region between these regimes are simulated in four different meshes: one with 15264 volumes, another with 30528, one with 48760, and finally, one with 186560 volumes. To validate the simulations developed, the values are compared with cases presented in the literature.

5.1 ANNULAR FLOW

The first simulated flow pattern was the annular flow with a mass flow rate of $1.87x10^{-2}$ $[kg/s]$ for the air and $2.53x10^{-2}$ $[kg/s]$ for the water. This point was taken from the Govan *et. al* (1991) experiment, to enable the subsequent validation of the simulations. The geometry of the piping, the fluids used, and the detailed boundary conditions have already been discussed in chapter 4 and can be seen in Figure 14 and in Tables 2 and 3.

5.1.1 Mesh 1: 15264 Volumes

The first analysis of the annular flow was performed in a very thick mesh containing 15264 volumes, 288 in the transversal and 53 in the axial direction. Two-phase flows require considerable simulation time, so it is important to make an analysis of the influence of the mesh refinement in the simulations, since thinner meshes require a much greater computational effort.

Figure 15 shows the temporal variation of the void fraction, measured between the planes located at 0.296 [m] and 1.195 [m] from the pipe inlet. The simulation starts with a gas void fraction equal to one, since the pipe is initially filled with air only. In the initial moments the gas fraction decreases, indicating the influx of the liquid phase, since the sum of the gas and the liquid volumetric fractions must be equal to one. With the progression of time, the void fraction seems to present a smooth behavior, which is not very characteristic of the annular flow, as there should normally be some oscillations that indicate the passage of liquid droplets in the tube, or the passage of disturbance waves.

Figure 16 shows the temporal variation of the dimensionless gas superficial velocity, calculated with the aid of Equation 2.11. The gas undergoes a sudden drop in its velocity in the initial instants with the influx of the liquid phase in the pipeline, but over time the variation of the gas velocity becomes minimal, indicating that the simulation was not able to capture all the interaction between the liquid and gas phases inside the tube. This is probably a consequence of the mesh used, which may have not been thin enough to capture the flow details.

Figure 15 – Void fraction between the 0.296 [m] and 1.195 [m] planes for the annular flow simulated with a 15264 mesh.

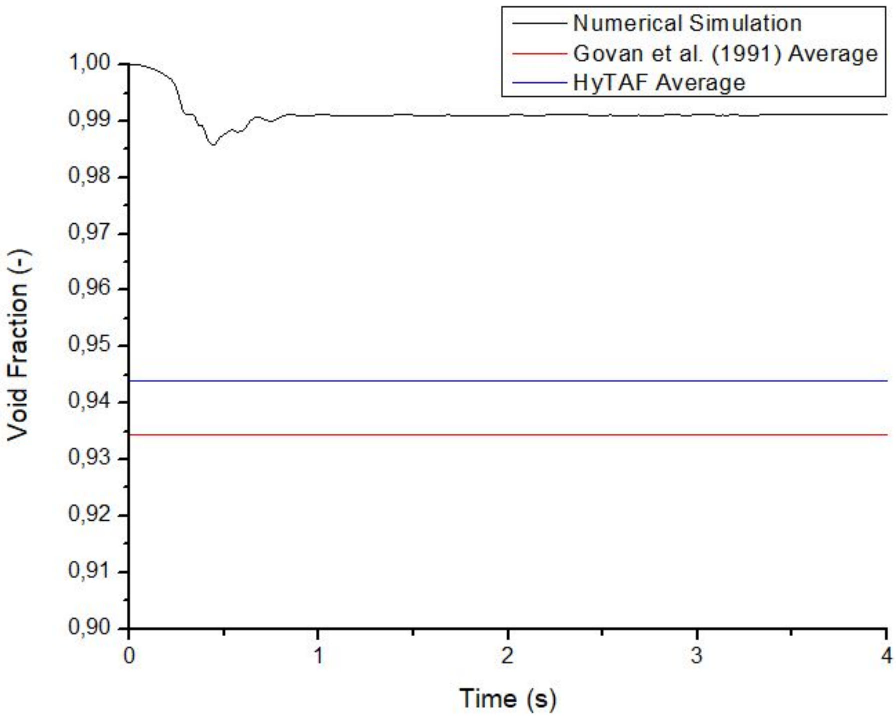

Source: Author (2021).

Figure 17 shows the temporal variation of the pressure gradient inside the pipe, calculated between the planes located at 0.381 [m] and 1.227 [m] from the duct inlet. Its behavior can be analyzed in conjunction with Figure 15 of the void fraction: when there is more liquid in the pipeline, the pressure gradient is higher, as the liquid is much heavier than the gas and therefore requires a higher consumption of energy, which also reflects in the increase of the pressure gradient. When the void fraction is closer to one, the pressure gradient tends to decrease.

The relative errors (E_R) between the simulations and the experiment conducted by Govan *et al.* (1991) and HyTAF simulations (ALVES, 2014; ALVES *et al.* 2017) were calculated using Equation 5.1:

$$\%E_R = 100.\left|\frac{S_v - R_v}{R_v}\right| \tag{5.1}$$

where S_v is the average of the simulated values and R_v is the reference value.

The relative error between the Govan *et al.* (1991) experiment and the simulations conducted were 6.06% for the void fraction and 35.83% for the pressure gradient. Regarding the HyTAF simulations, the error was 5.01% for the void fraction and 16.24% for the pressure gradient. The dimensionless gas superficial velocity was plotted together with the theoretical transition value $j_g* = 1$. In theory, the annular-churn transition should occur at this point, whereas the annular pattern should assume values above one, but as mentioned in subsection 2.2.3 of this work, this does not always occur in practice.

Figure 16 – Dimensionless gas superficial velocity at 0.858 [m] from the pipe inlet for the annular flow simulated with a 15264 mesh.

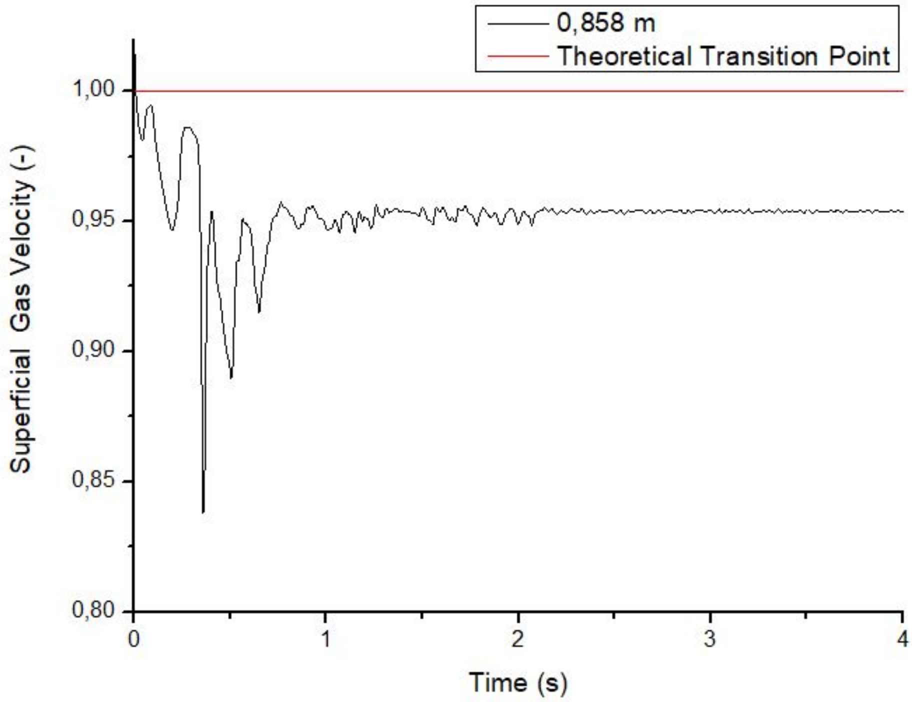

Source: Author (2021).

Figure 17 – Pressure gradient at 0.858 [m] from the inlet for the annular flow simulated with a 15264 mesh.

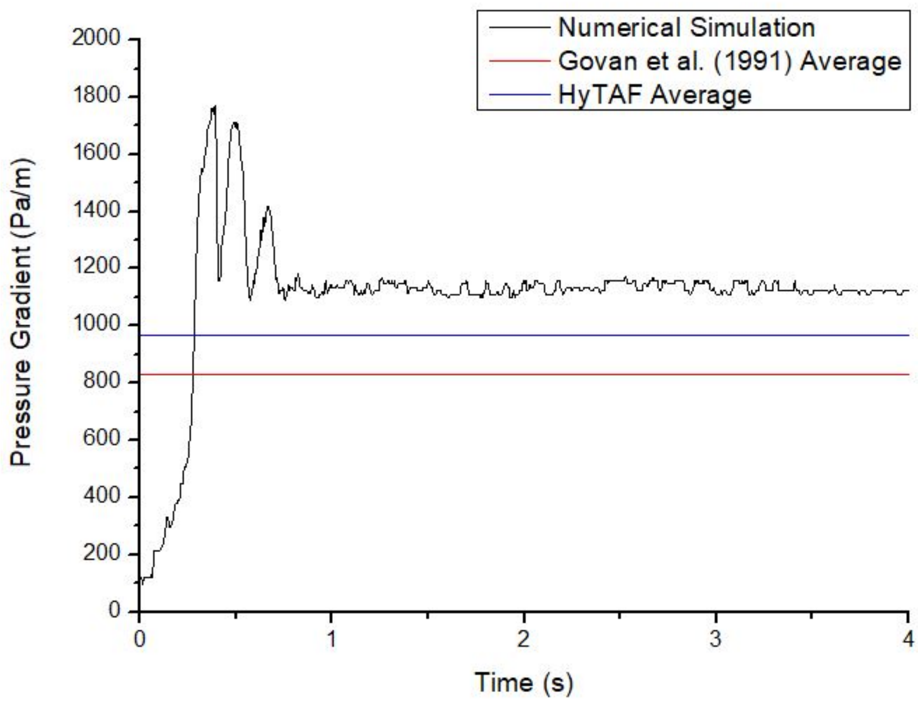

Source: Author (2021).

For a better understanding of the flow, Figures 18 and 19 were obtained, and they present the isosurface with 98% air for the annular flow at different times. In each of the figures, the cross sections of the pipe are shown at two different points: the first cut is made at a position 0.296 [m] away from the tube inlet, and the second one is located at 1.195 [m] from the tube inlet.

Through the analysis of Figures 18 and 19, the simulation captured, in both cases, a very irregular liquid film with several ripples. At the point located at 0.296 [m] from the inlet, the film is still being formed and the flow is not yet fully developed, because of the proximity to the fluid injection point. At 1.195 [m], the liquid film begins to atomize, and runs out in some places, not fully encompassing the diameter of the tube. In addition, the liquid droplets that should be pulled from the liquid film by shearing forces are not observed in the gas core. Several factors may have caused these inconsistencies, such as the mesh used, an inefficient capture of the interface, or some deficiency in the shear stress modeling.

Figure 18 – Isosurfaces for annular flow at 0.296 [m] simulated with a 15264 mesh.

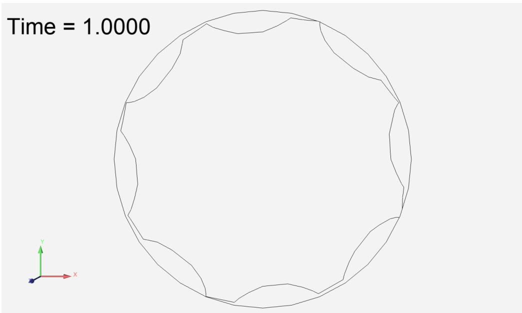

(a) Annular flow in 1s.

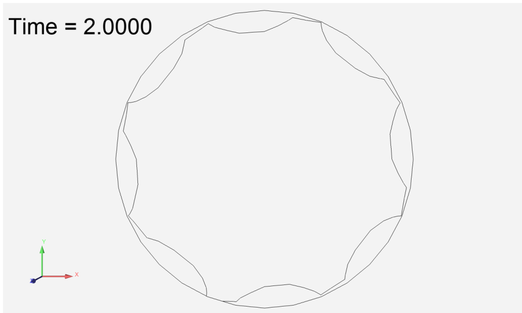

(b) Annular flow in 2s.

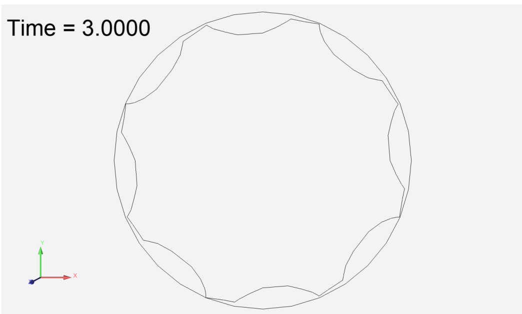

(c) Annular flow in 3s.

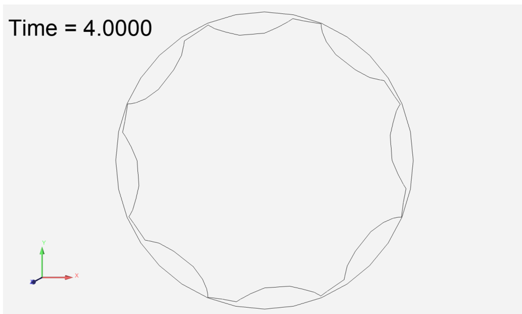

(d) Annular flow in 4s.

Source: Author (2021).

Figure 19 – Isosurfaces for annular flow at 1.195 [m] simulated with a 15264 mesh.

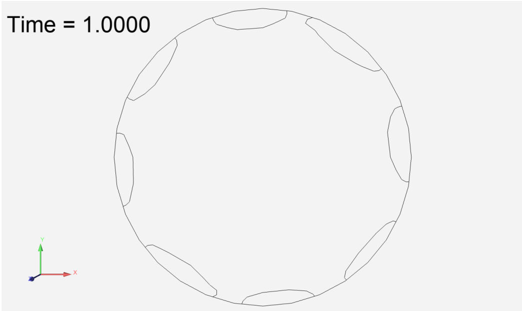

(a) Annular flow in 1s.

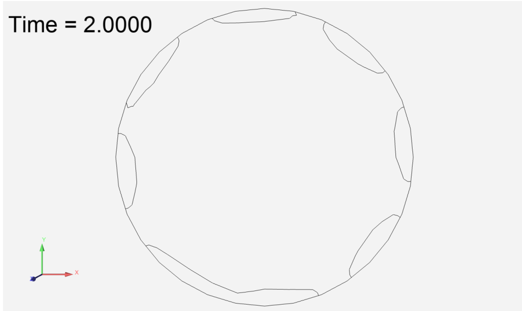

(b) Annular flow in 2s.

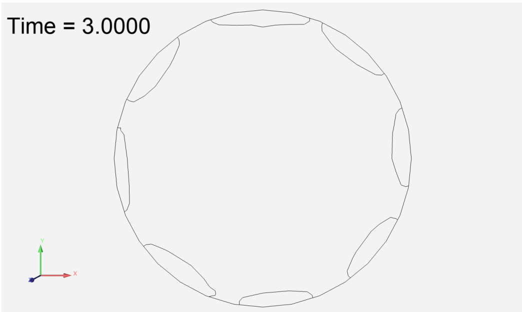

(c) Annular flow in 3s.

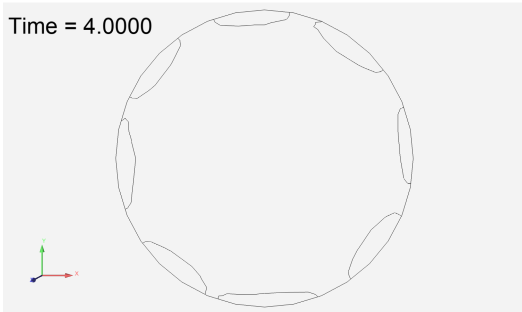

(d) Annular flow in 4s.

Source: Author (2021).

5.1.2 Mesh 2: 30528 Volumes

A second mesh with 30528 volumes was used to simulate the annular flow. This mesh has the same cross section as mesh 1, with 288 volumes. However, it has a greater axial refining, containing 106 volumes. Figure 20 shows the void fraction temporal variation, and as in the previous case, the influx of the liquid phase into the tube causes an initial drop in the gas void fraction. In this case large oscillations appear over time, demonstrating that the axial refining of the mesh was able to capture greater details of the flow and of the interaction between the liquid and gas phases. The relative error calculated between the simulation of the void fraction with this mesh and the Govan *et al.* (1991) experiment was 5.87%. For the HyTAF simulations, the relative error was 4.82%.

Figure 21 shows the dimensionless gas superficial velocity at 0.858 [m] from the pipe inlet. Different from that what was found in the 15264-volume mesh, large fluctuations appear in the superficial velocity, indicating that the gas is either accelerating or decelerating inside the pipe, due to the interference of the liquid phase. These oscillations are reflected in the pressure gradient, shown in Figure 22, which also presents much larger oscillations when compared to the previous mesh. The relative error calculated between the pressure gradient simulation with the axially refined mesh and the experiment of Govan *et al.* (1991) was 33.41%. For the HyTAF simulations, the relative error was 14.16%.

Figure 20 – Void fraction between the 0.296 [m] and 1.195 [m] planes for the annular flow simulated with a 30528 mesh.

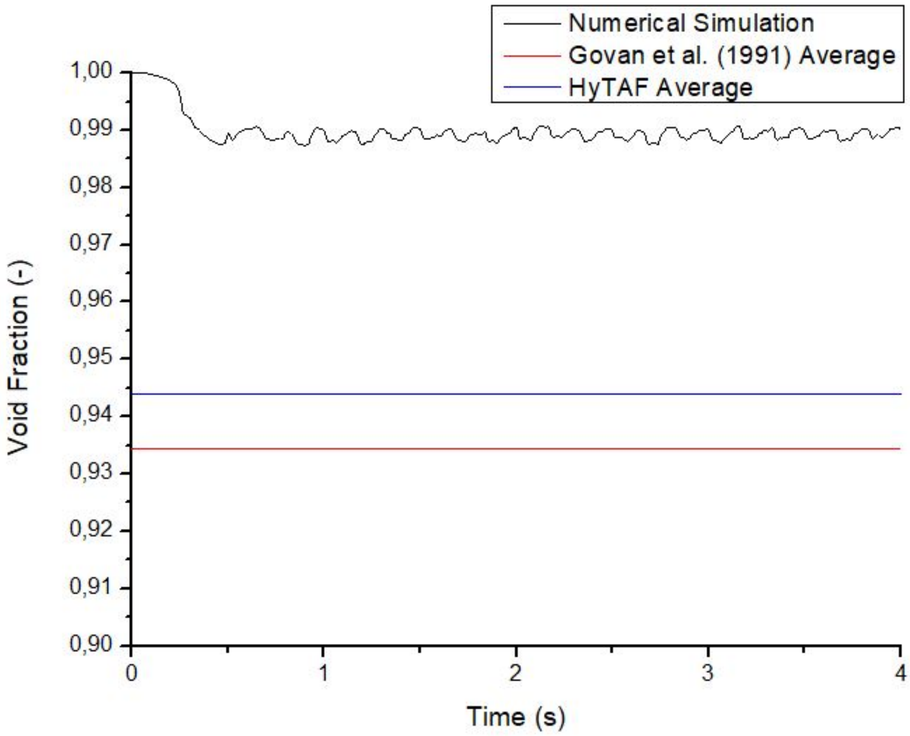

Source: Author (2021).

Figures 23 and 24 show the isosurfaces with 98% air for the annular flow for a short lapse of time, at 0.296 [m] and 1.195 [m] from the pipe inlet, respectively. Through these figures, the simulation captured a more regular liquid film when compared to that obtained by mesh 1. However, there is still an inconsistency in the simulation of the model, since, again, the liquid film characteristic of the annular flow is not continuous in the simulated interval. In both cases, the thickness of the film varies a lot over time, probably due to the passage of disturbance waves, and there are points where the liquid film runs out.

Moreover, even with the 30528-volume mesh, it was still not possible to capture the liquid droplets in the gas core, which should dragged from of the liquid film by shear forces. However, although the simulation did not show these droplets characteristic of annular flow, it was still possible to capture oscillations in the void fraction, superficial velocity and pressure gradient. Probably, these oscillations are due to the greater variation detected in the thickness of the liquid film during the simulation.

Figure 21 – Dimensionless gas superficial velocity at 0.858 [m] from the pipe inlet for the annular flow simulated with a 30528 mesh.

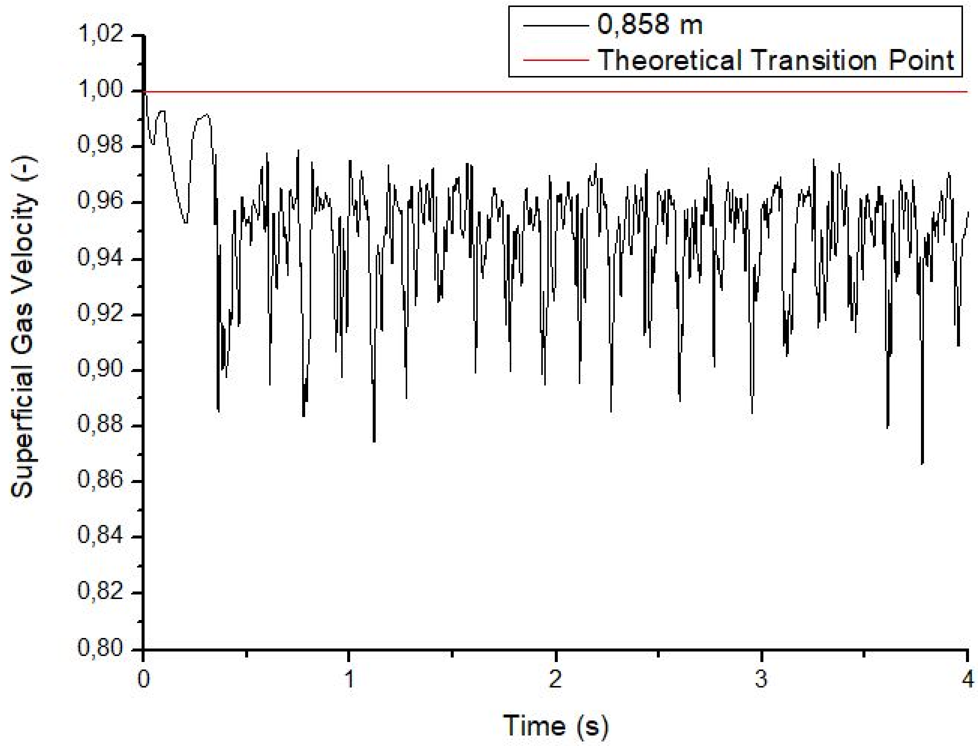

Source: Author (2021).

Figure 22 – Pressure gradient at 0.858 [m] from the inlet for the annular flow simulated with a 30528 mesh.

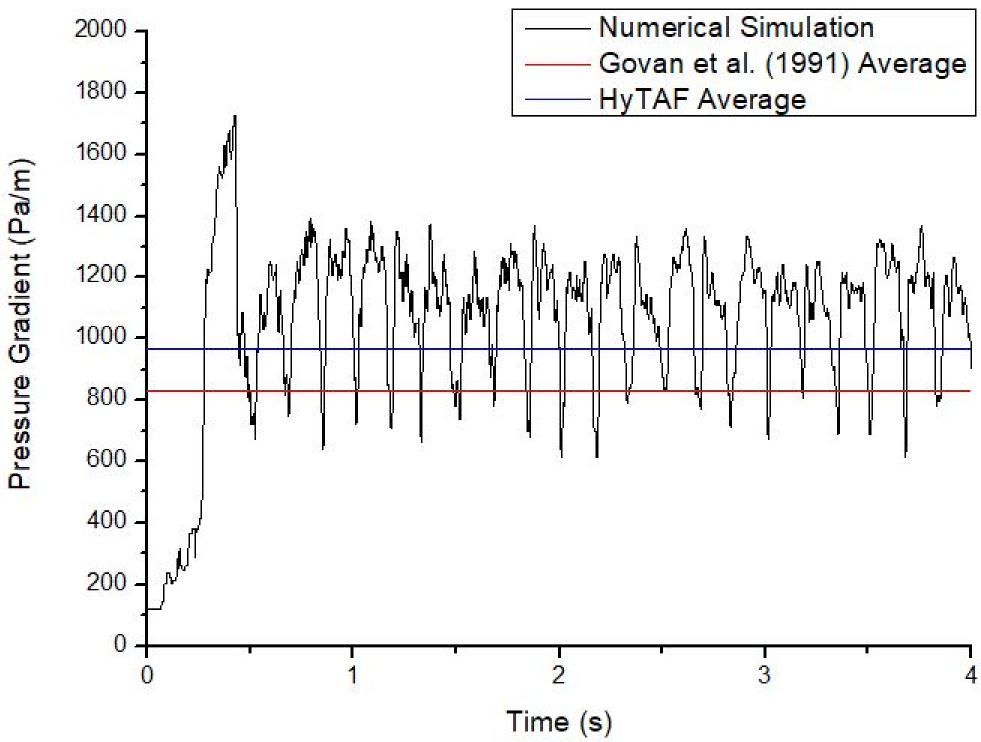

Source: Author (2021).

Figure 23 – Isosurfaces for annular flow at 0.296 [m] simulated with a 30528 mesh.

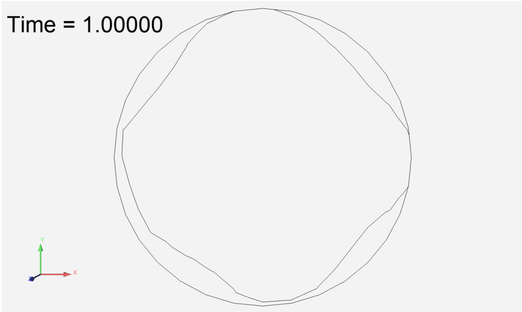

(a) Annular flow in 1s.

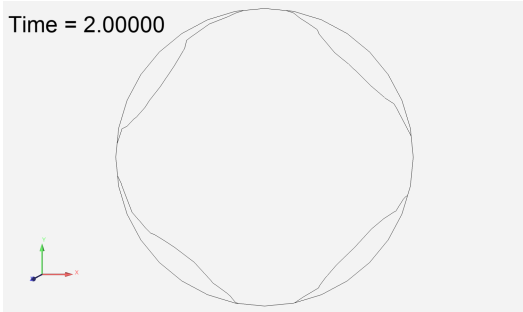

(b) Annular flow in 2s.

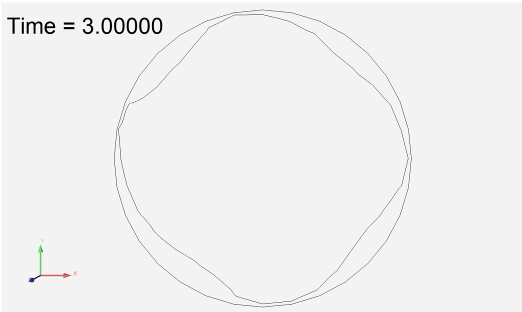

(c) Annular flow in 3s.

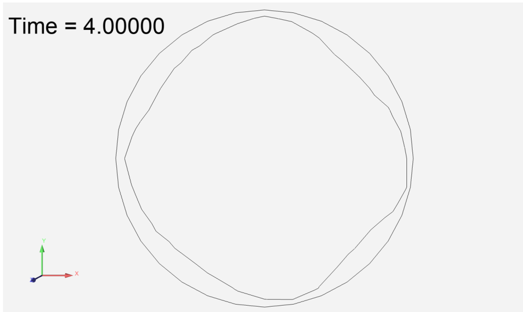

(d) Annular flow in 4s.

Source: Author (2021).

Figure 24 – Isosurfaces for annular flow at 1.195 [m] simulated with a 30528 mesh.

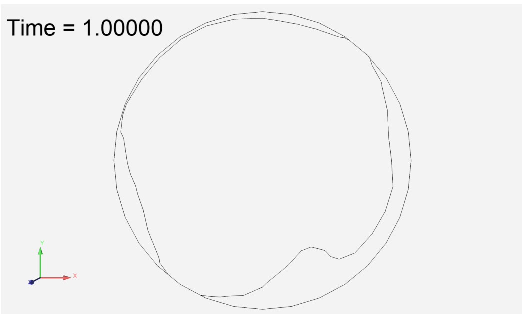

(a) Annular flow in 1s.

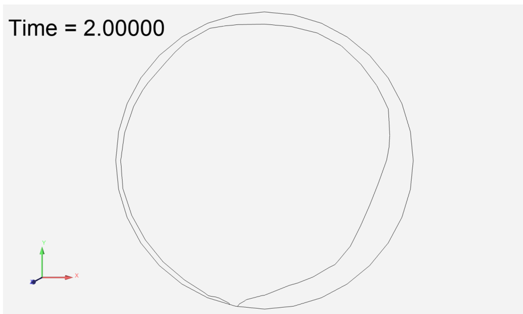

(b) Annular flow in 2s.

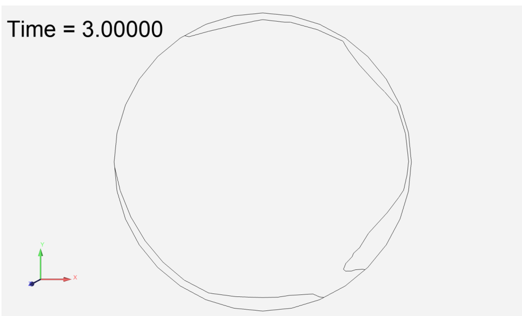

(c) Annular flow in 3s.

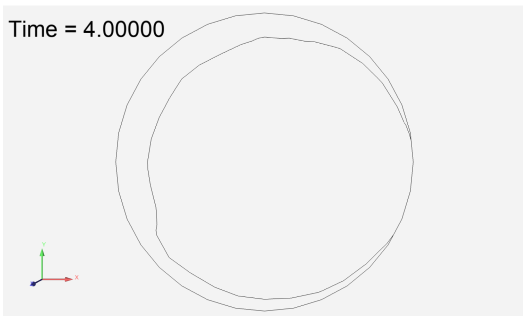

(d) Annular flow in 4s.

Source: Author (2021).

5.1.3 Mesh 3: 48760 Volumes

The third case studied was the annular flow with the same boundary conditions. However, in a mesh with intermediate grid of 48760 volumes, 460 in the transversal and 106 in the axial. Figure 25 shows the void fraction found between the planes located at 0.296 [m] and 1.195 [m] from the pipe inlet. The oscillations are less accentuated when compared to the previous 30528-mesh. However it is still possible to observe important oscillations that indicate the interaction between the liquid and gas phases. The relative error calculated between the simulation of the void fraction with the third mesh, and the experiment by Govan *et al.* (1991) was 6.05%. For the HyTAF simulations, the relative error was 4.99%.

Figure 26 shows the dimensionless gas superficial velocity at a point located 0.858 [m] from the pipe inlet. The behavior over time is very similar to that found in the simulation performed with mesh 2. The pressure gradient was also obtained and is illustrated in Figure 27. The relative error calculated between the simulation of the pressure gradient with the mesh of 48760 volumes, and the experiment by Govan *et al.* (1991) was 22.02%. For the HyTAF simulations, the relative error was 4.42%.

Figure 25 – Void fraction between the 0.296 [m] and 1.195 [m] planes for the annular flow simulated with a 48760 mesh.

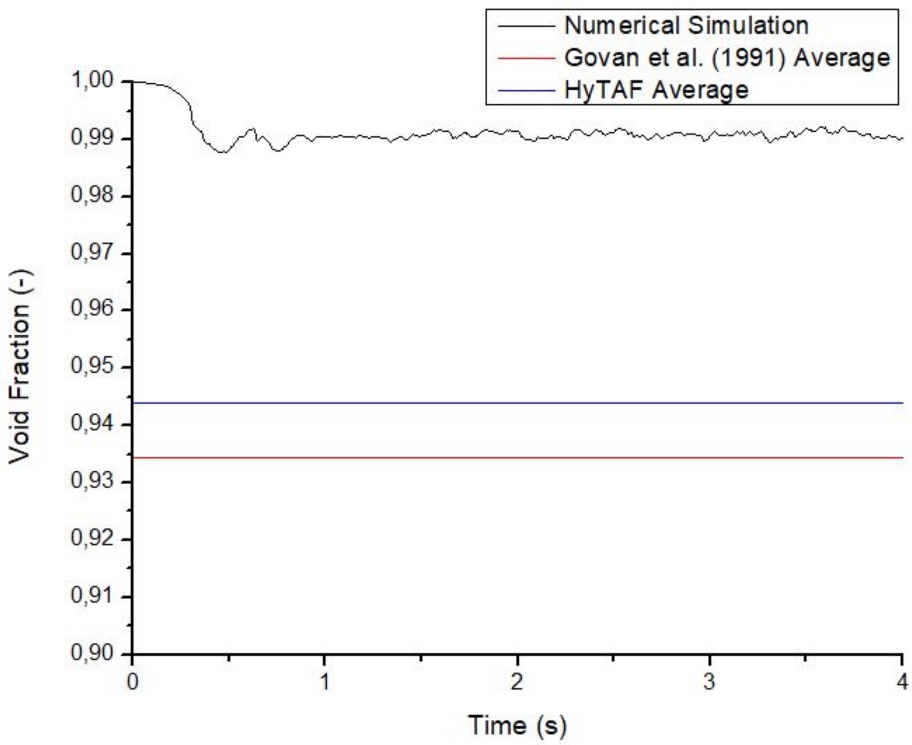

Source: Author (2021).

Figure 26 – Dimensionless gas superficial velocity at 0.858 [m] from the pipe inlet for the annular flow simulated with a 48760 mesh.

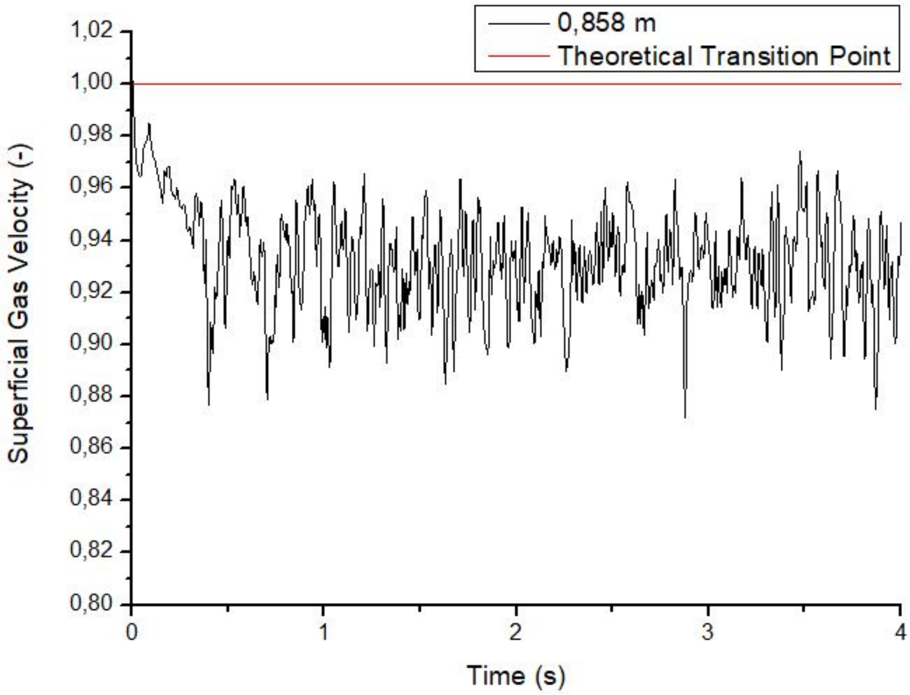

Source: Author (2021).

Figure 27 – Pressure gradient at 0.858 [m] from the inlet for the annular flow simulated with a 48760 mesh.

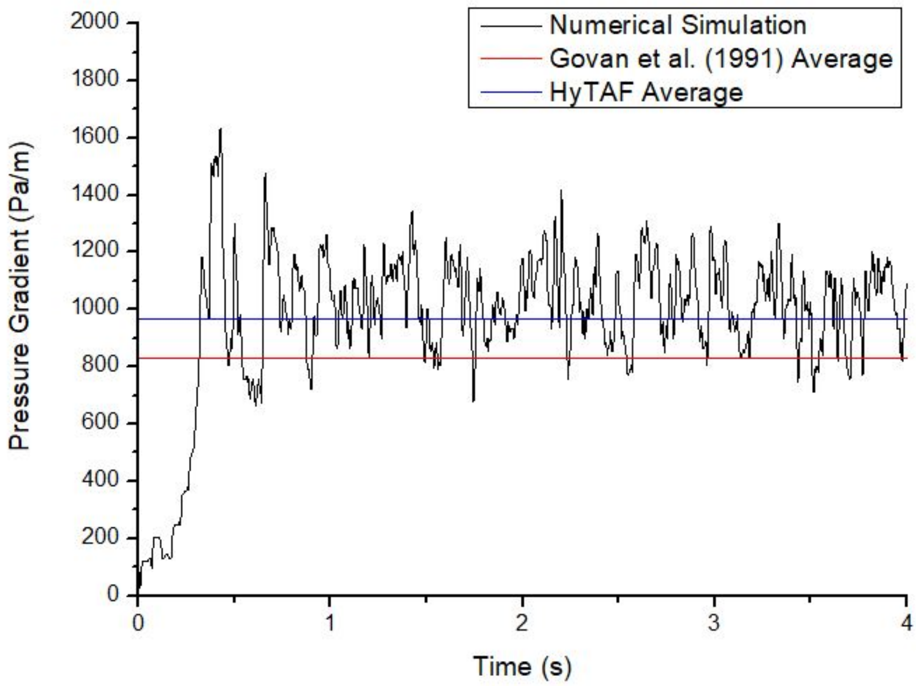

Source: Author (2021).

Figures 28 and 29 show the isosurfaces with 98% air for the annular flow, at 0.296 [m] and 1.195 [m] from the pipe inlet, respectively. Through the analysis of these figures, the liquid film is a little less regular than that found through the simulation with mesh 2. In this case, there seems to be more regions where the liquid film becomes atomized, and the liquid droplets, which should be present in the gas core, do not appear again. Thus, as in mesh 2, the largest oscillations detected in the void fraction, superficial velocity and pressure gradient are due to the variation in the liquid film thickness during the simulation.

Despite the liquid film becoming more atomized in the simulation conducted with the mesh of 48760 volumes, the results found for the pressure gradient were better than those obtained with the meshes of 15264 and 30528 volumes.

Figure 28 – Isosurfaces for annular flow at 0.296 [m] simulated with a 48760 mesh.

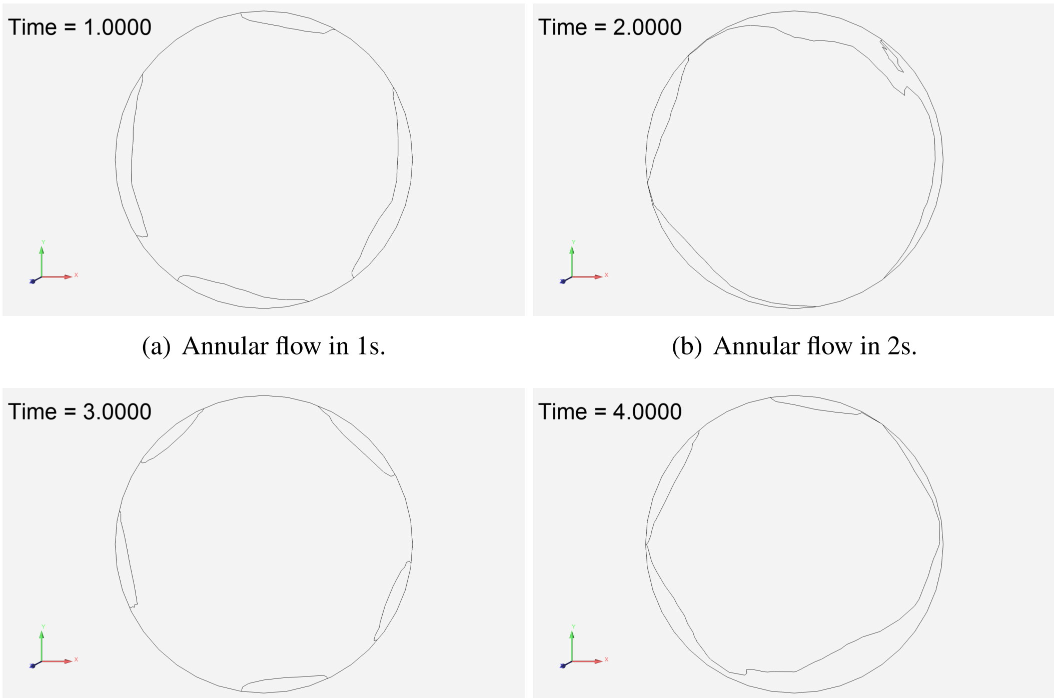

(a) Annular flow in 1s.

(b) Annular flow in 2s.

(c) Annular flow in 3s.

(d) Annular flow in 4s.

Source: Author (2021).

Figure 29 – Isosurfaces for annular flow at 1.195 [m] simulated with a 48760 mesh.

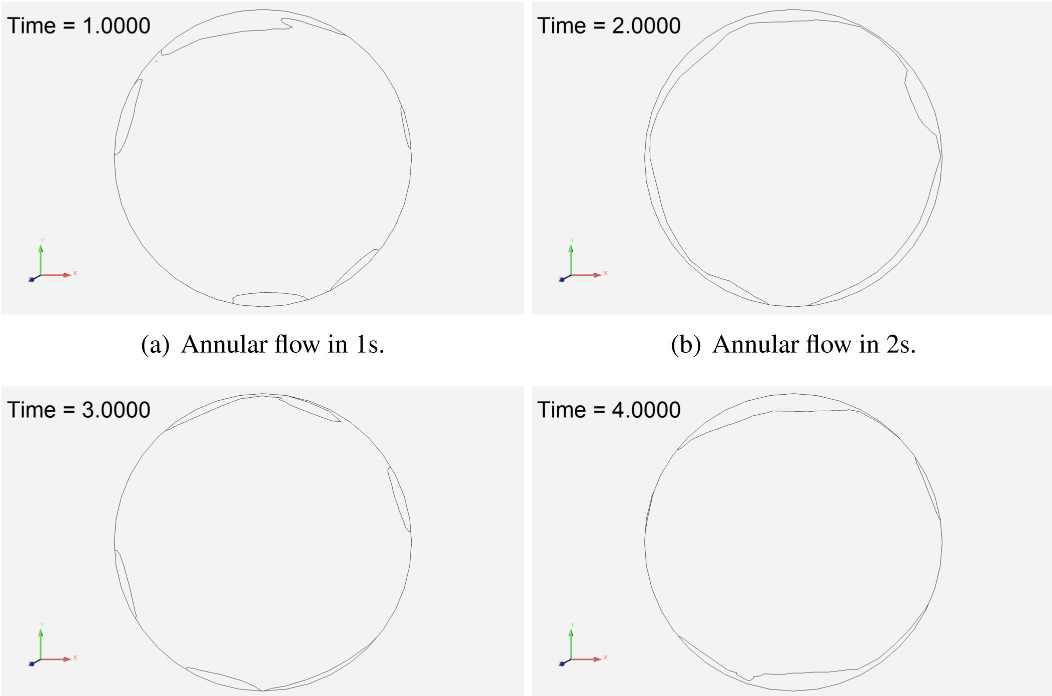

(a) Annular flow in 1s.

(b) Annular flow in 2s.

(c) Annular flow in 3s.

(d) Annular flow in 4s.

Source: Author (2021).

5.1.4 Mesh 4: 186560 Volumes

A simulation for the annular flow in a mesh with 186560 volumes was also performed, to complete the analysis of the effect of the mesh size on the flow capture. This mesh has a large cross-sectional refinement, containing 1760 volumes, and 106 axial volumes. Figure 30 shows the temporal variation of the void fraction, measured between the planes located at 0.296 [m] and 1.195 [m] from the pipe inlet. Unlike the previous meshes, this simulation was able to capture a great disturbance in the void fraction, probably caused by the passage of liquid filaments in the pipeline or even by the natural oscillation of the liquid film thickness, which in the case of mesh 4 is described in more detail. The relative error between the simulations performed for the void fraction and the experiment of Govan *et al.* (1991) was 4.90%. For the HyTAF simulations, the error was 3.86%.

Figure 31 illustrates the dimensionless gas superficial velocity, measured in three different points: 0.381 [m], 0.858 [m] and 1.227 [m]. Through this figure, the dimensionless gas superficial velocity tends to increase with distance, so that the averages at points 0.381 [m], 0.858 [m] and 1.227 [m] were calculated for the last second of simulation such as 0.901, 0.945 and 0.955, respectively. In addition, greater fluctuations are observed at the point closest to the entrance of the pipeline. This occurs because in this region there is more liquid filaments being formed, which causes a greater flow disturbance.

Figure 30 – Void fraction between the 0.296 [m] and 1.195 [m] planes for the annular flow simulated with a 186560 mesh.

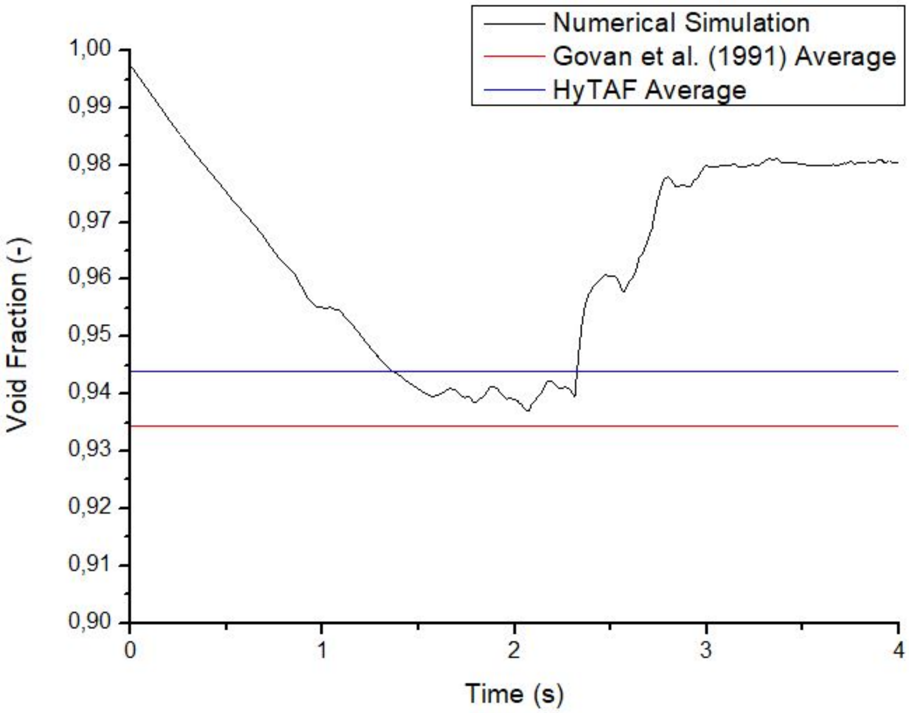

Source: Author (2021).

Figure 31 – Dimensionless gas superficial velocity measured at three different points: 0.381 [m], 0.858 [m] and 1.227 [m].

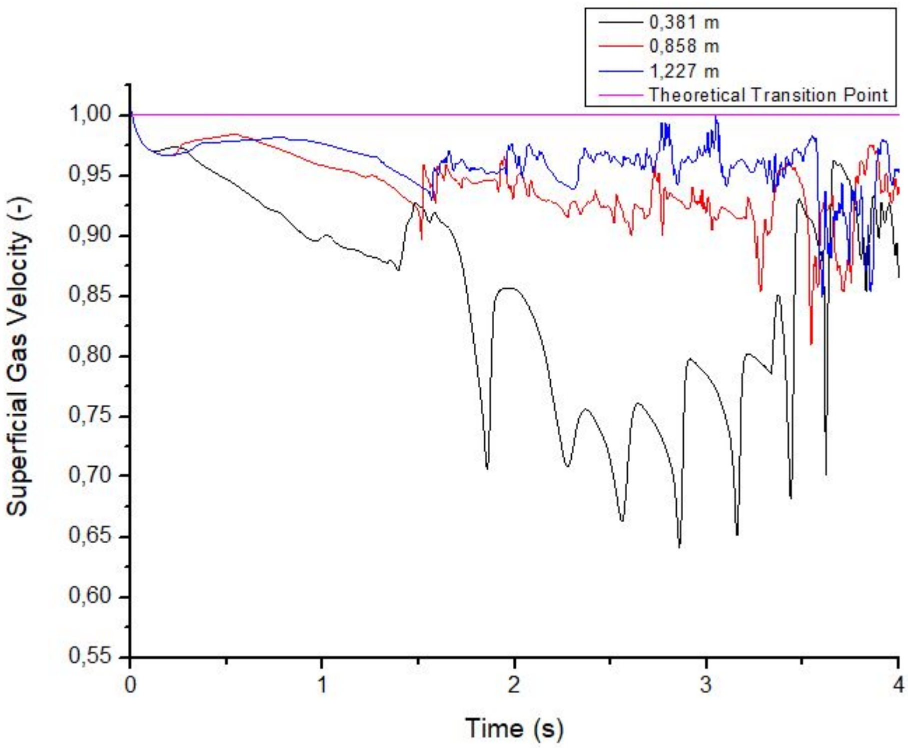

Source: Author (2021).

Figure 32 shows the time variation of the pressure gradient calculated between the plans located at 0.381 [m] and 1.227 [m] from the pipe inlet. Through this figure, the simulation captured more fluctuations when compared to previous simulations, reaching a much higher peak. This occurs because this mesh was able to capture details of the flow that the others were unable to, such as greater oscillations in the void fraction, which resulted in a greater oscillation in the pressure gradient. The relative error between the simulations performed for the pressure gradient and the experiment of Govan *et al.* (1991) was 38.25%. For the HyTAF simulations, the error was 18.31%.

Figure 32 – Pressure gradient at 0.858 [m] from the inlet for the annular flow simulated with a 186560 mesh.

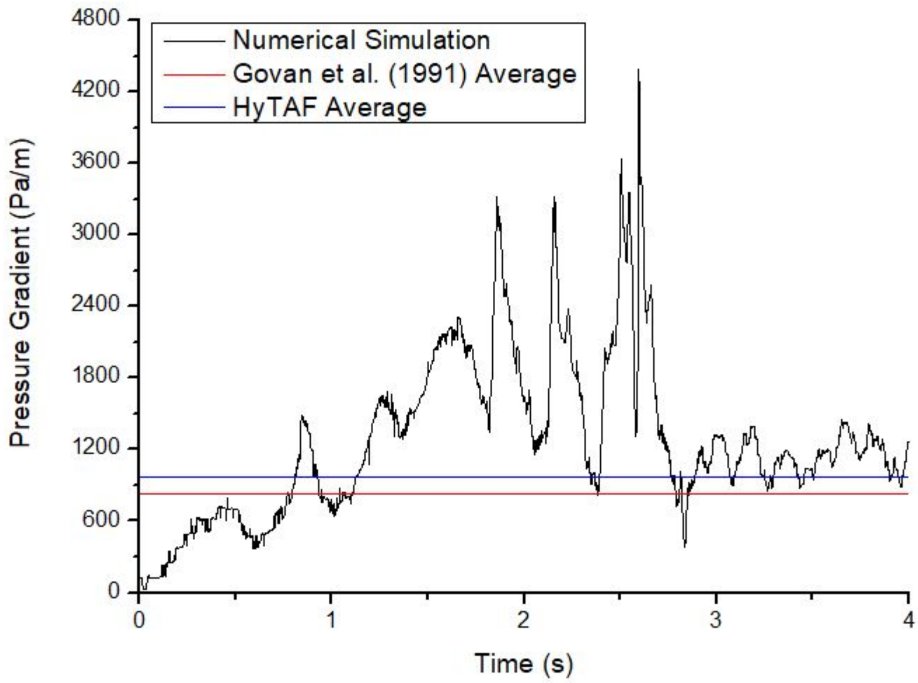

Source: Author (2021).

Figures 33 and 34 show the isosurfaces with 98% air for the annular flow in some moments, at 0.296 [m] and 1.195 [m] from the tube inlet, respectively. At the point located at 0.296 [m] from the entrance, the flow is not yet fully developed, and it is possible to observe the formation of an unstable liquid film that soon breaks. At the point located at 1.195 [m] from the tube entrance, in addition to the unstable film, there are some liquid filaments that detach from the film by shear forces. This was the only mesh that managed to capture this phenomenon. However, the liquid film is still running out, which is probably caused by a deficiency in the interface capture, in the shear stress modeling, or even in the mesh used.

Figure 33 – Isosurfaces for annular flow at 0.296 [m] simulated with a 186560 mesh.

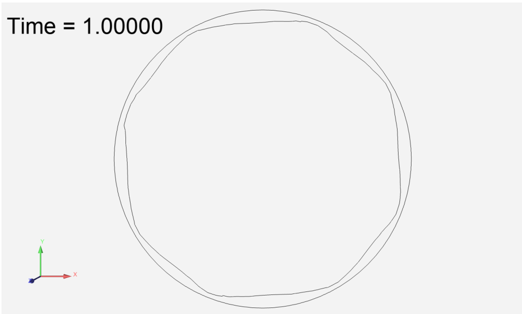

(a) Annular flow in 1s.

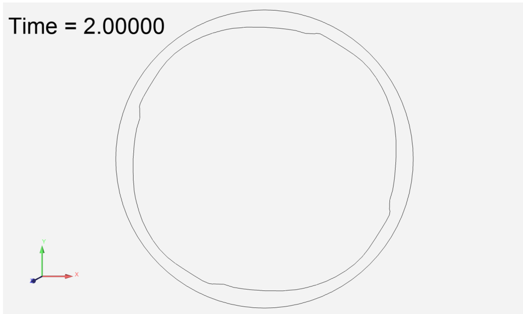

(b) Annular flow in 2s.

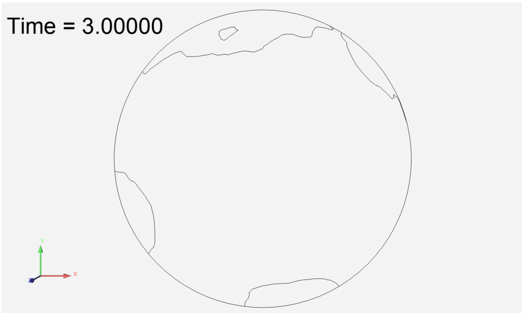

(c) Annular flow in 3s.

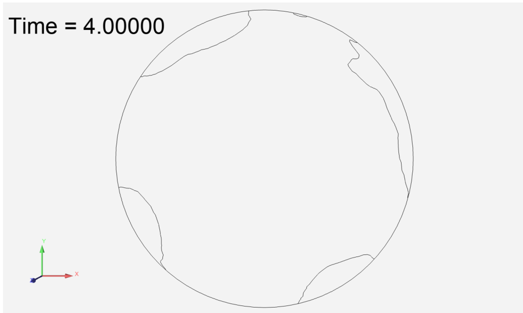

(d) Annular flow in 4s.

Source: Author (2021).

Figure 34 – Isosurfaces for annular flow at 1.195 [m] simulated with a 186560 mesh.

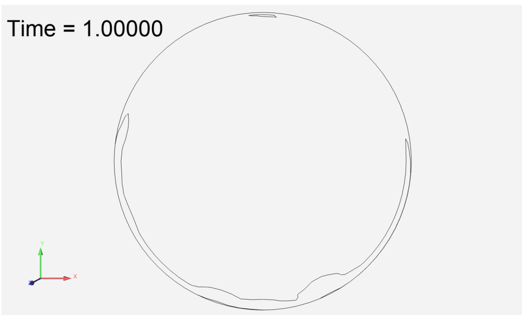

(a) Annular flow in 1s.

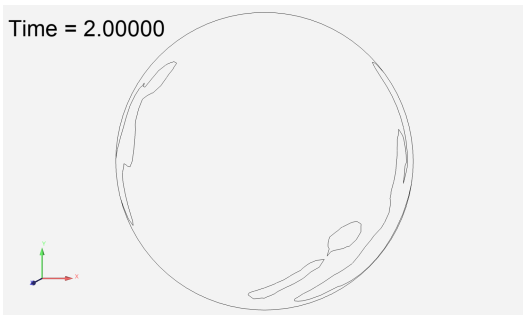

(b) Annular flow in 2s.

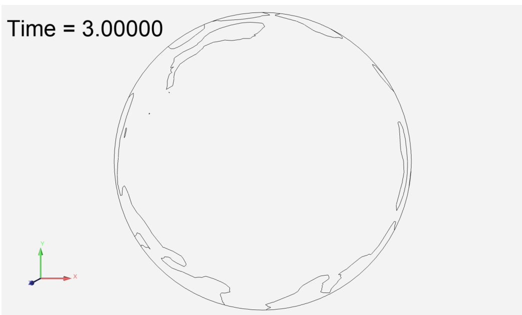

(c) Annular flow in 3s.

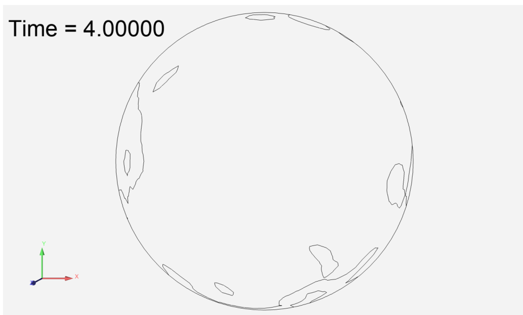

(d) Annular flow in 4s.

Source: Author (2021).

Table 4 summarizes the results found with the four meshes tested for the annular flow.

Table 4 – Relative errors found for annular flow.

ANNULAR FLOW				
Relative Error	*Govan et al. (1991)*		*HyTAF*	
	Void Fraction [-]	Pressure Gradient [Pa/m]	Void Fraction [-]	Pressure Gradient [Pa/m]
Mesh 1	6.06%	35.83%	5.01%	16.24%
Mesh 2	5.87%	33.41%	4.82%	14.16%
Mesh 3	6.05%	22.02%	4.99%	4.42%
Mesh 4	4.90%	38.25%	3.86%	18.31%

Source: Author (2021).

5.2 CHURN-ANNULAR TRANSITION

The second flow condition was a transition point between annular and churn flows, with a mass flow rate of $1.73x10^{-2}$ $[kg/s]$ for the air and $2.53x10^{-2}$ $[kg/s]$ for the water. The geometry of the piping, the fluids used, and the detailed boundary conditions have already been discussed in chapter 4. For the transition point, the simulations were performed using meshes 1, 3 and 4.

5.2.1 Mesh 1: 15264 Volumes

The first analysis of the transition point was performed with a thick mesh, of 15264 volumes. Figure 35 shows the time variation of the void fraction. As in the annular flow previously studied, the simulation starts with the tube filled with air only,, until the influx of the liquid phase causes a change in the gas void fraction. The behavior of the void fraction over time is smooth and without oscillations, probably indicating that the simulation is capturing little interaction between the liquid and gas phases in the pipeline. When liquid droplets or filaments flow through the tube, fluctuations in the gas void fraction are expected to be found. The relative error calculated between the simulation of the void fraction with the mesh 1 and the experiment by Govan *et al.* (1991) was 6.31%. For the HyTAF simulations, the relative error was 4.44%.

Figure 36 shows the temporal variation of the dimensionless gas superficial velocity at 0.858 [m] from the duct inlet. Its behavior is similar to that found for the annular flow with the 15264-volume mesh, but in this case the fluctuations are slightly higher. Once again, the gas undergoes a sudden drop in velocity due to the influx of the liquid phase into the tube and, over time, the variation in the superficial velocity of the gas becomes very small, indicating that the simulation was not able to capture all the interaction between the phases in detail, reinforcing what had already been verified through Figure 35.

Figure 35 – Void fraction between the 0.296 [m] and 1.195 [m] planes for the churn-annular transition simulated with a 15264 mesh.

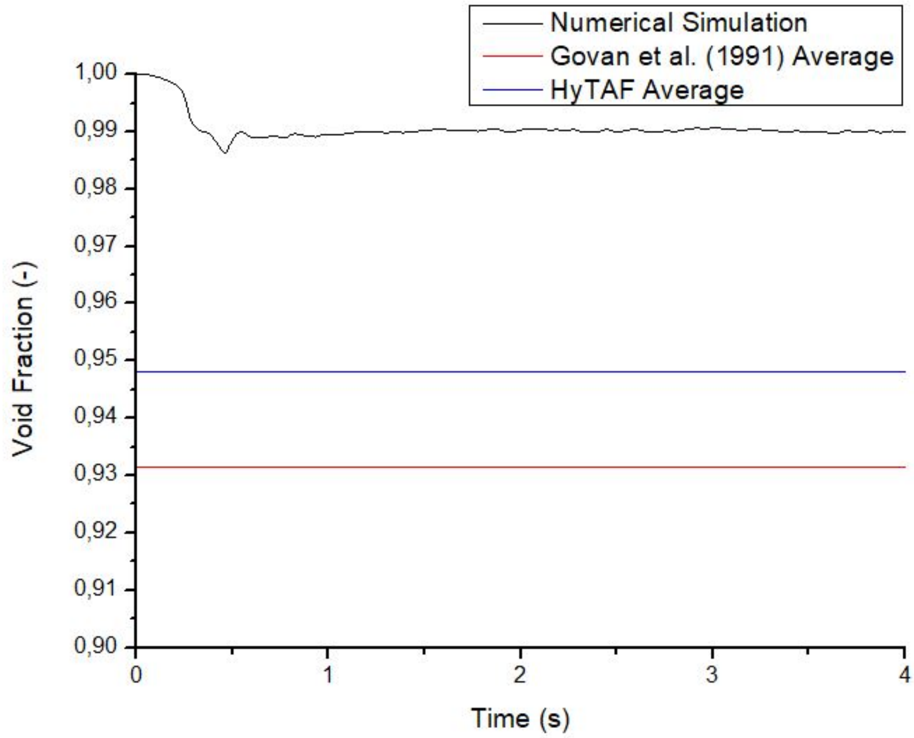

Source: Author (2021).

Figure 36 – Dimensionless gas superficial velocity at 0.858 [m] from the pipe inlet for the churn-annular transition simulated with a 15264 mesh.

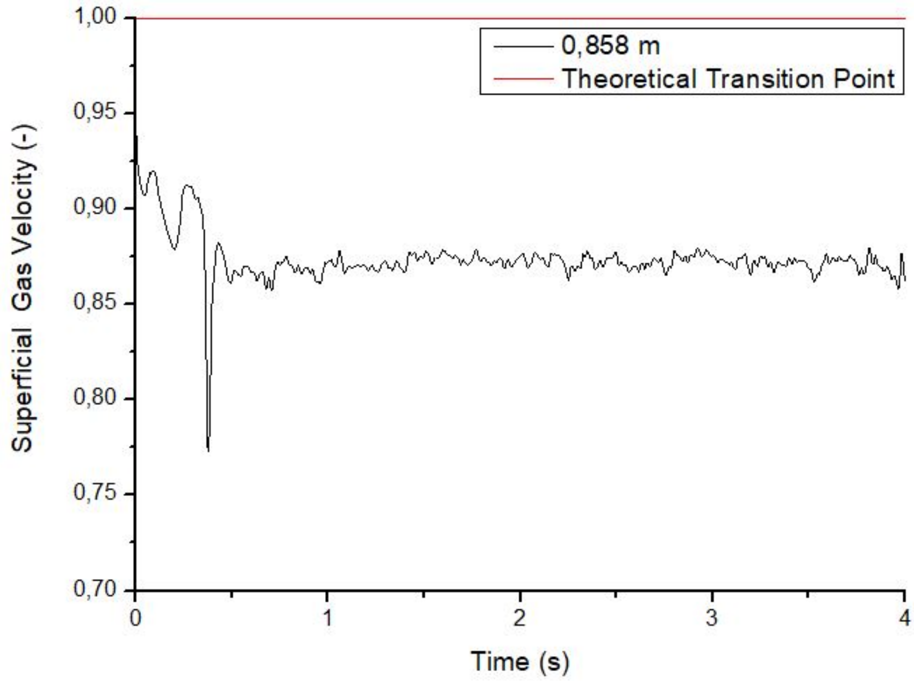

Source: Author (2021).

Figure 37 – Pressure gradient at 0.858 [m] from the inlet for the churn-annular transition simulated with a 15264 mesh.

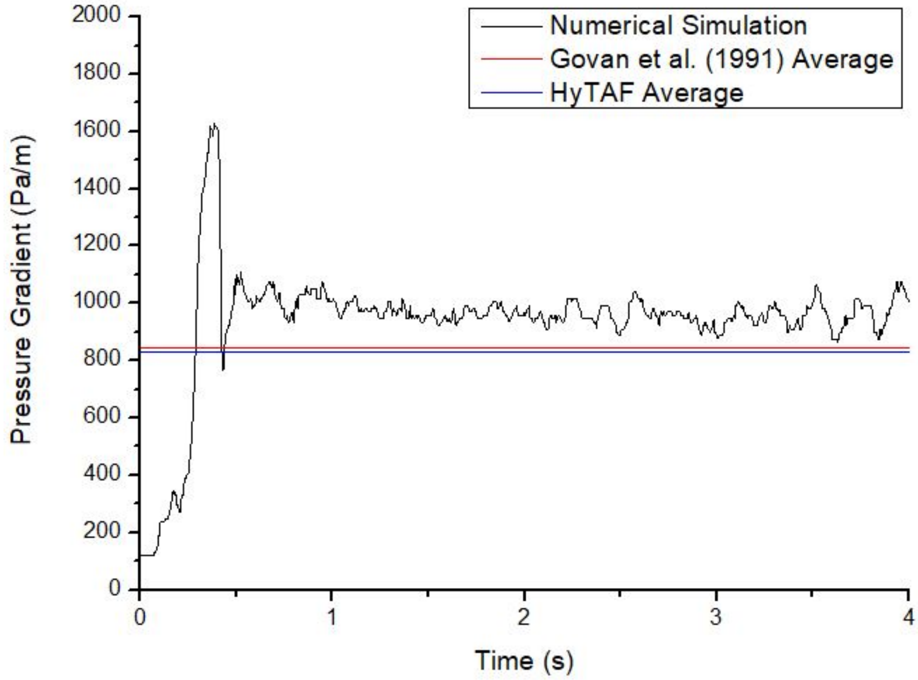

Source: Author (2021).

The results found for the void fraction and for the dimensionless gas superficial velocity are reflected in the pressure gradient, illustrated by Figure 37. Similarly to the other parameters obtained, the pressure gradient also shows mild fluctuations after the initial flow disturbance, caused by the influx of the liquid phase into the pipeline. The relative error calculated between the simulation of the pressure gradient with mesh 1 and the experiment by Govan *et al.* (1991) was 13.74%. For the HyTAF simulations, the relative error was 15.78%.

Figures 38 and 39 show the isosurfaces with 98% air for a short lapse of time, at 0.296 [m] and 1.195 [m] from the duct inlet, respectively. The simulation captured a very irregular liquid film with several undulations and discontinuities at the point located at 0.296 [m] from the entrance, where the flow is not fully developed. At the 1.195 [m] point, the liquid film acquires a slightly softer shape.

Figure 38 – Isosurfaces for churn-annular transition at 0.296 [m] simulated with a 15264 mesh.

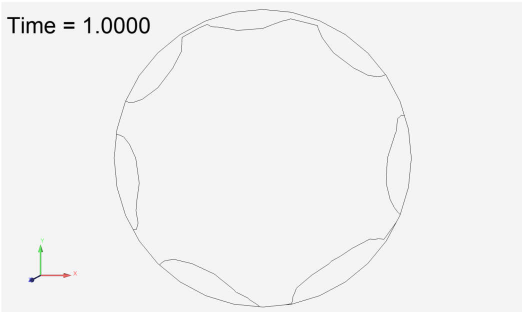

(a) Churn-annular transition in 1s.

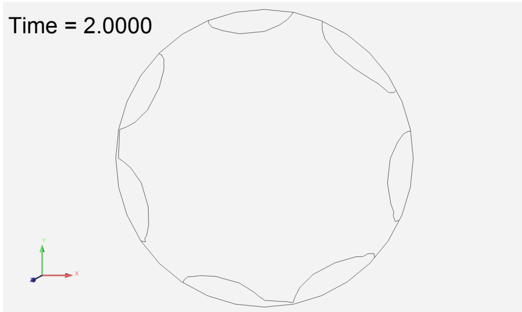

(b) Churn-annular transition in 2s.

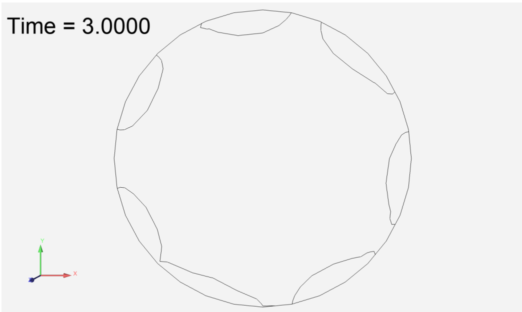

(c) Churn-annular transition in 3s.

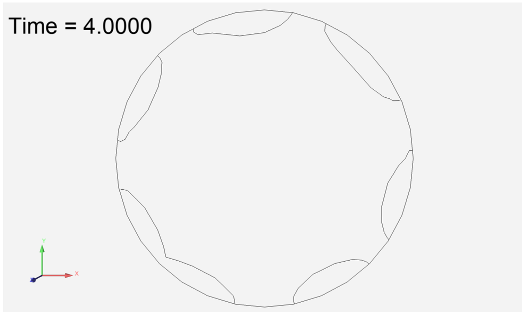

(d) Churn-annular transition in 4s.

Source: Author (2021).

Figure 39 – Isosurfaces for churn-annular transition at 1.195 [m] simulated with a 15264 mesh.

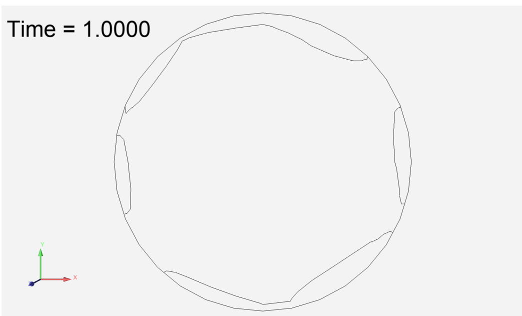

(a) Churn-annular transition in 1s.

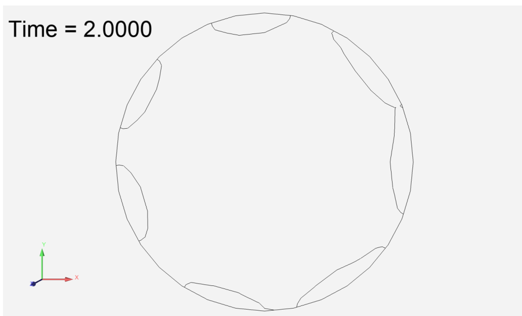

(b) Churn-annular transition in 2s.

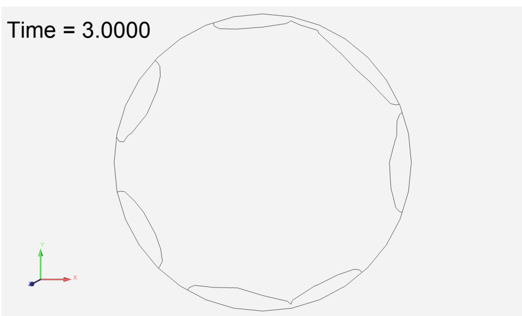

(c) Churn-annular transition in 3s.

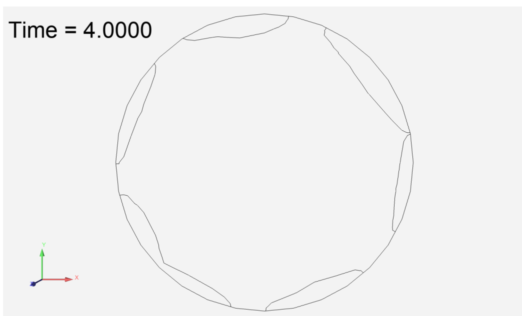

(d) Churn-annular transition in 4s.

Source: Author (2021).

5.2.2 Mesh 3: 48760 Volumes

The second simulated case for the transition between annular and churn flows was performed with a 48760-volume mesh. Figure 40 shows the temporal variation of the air void fraction, measured between the planes located at 0.296 [m] and 1.195 [m] from the pipe inlet. Over time, some oscillations in the void fraction are observed, which indicate that the simulation was able to capture some interaction between the phases. The relative error calculated between the simulation and the experiment by Govan *et al.* (1991) was 6.18%. For the HyTAF simulations, the relative error was 4.31%.

Figure 40 – Void fraction between the 0.296 [m] and 1.195 [m] planes for the churn-annular transition simulated with a 48760 mesh.

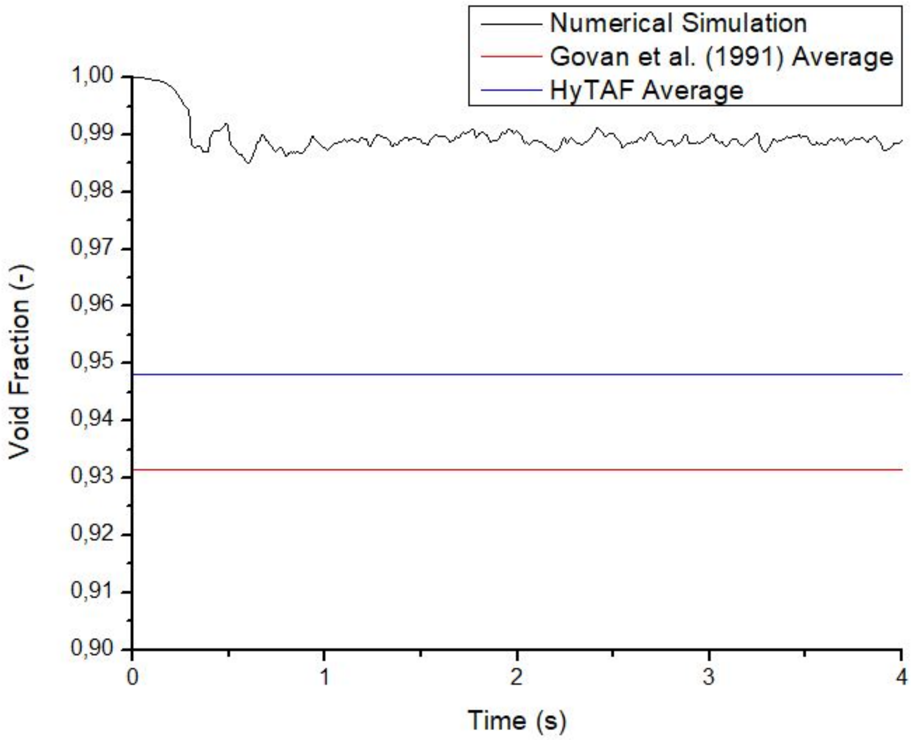

Source: Author (2021).

Figure 41 shows the time variation of the dimensionless gas superficial velocity. Large fluctuations appear and its average value calculated at the 0.858 [m] point was around 0.861, which is a value below the theoretical transition point. Wallis (1961) established that the flow reversal point, *i.e*, a point that characterizes the transition between the annular and churn flows, should occur when the dimensionless superficial velocity of the gas is approximately one. However, McQuillan (1985) presented several intervals where the flow reversal point could occur, which was emphasized by the work of Govan *et al.* (1991). The pressure gradient is shown in Figure 42. For this case, the relative error calculated between the simulation of the pressure gradient with the 48760-mesh, and the experiment conducted by Govan *et al.* (1991) was 11.01%. Regarding the HyTAF simulations, the relative error was 13.00%.

Figure 41 – Dimensionless gas superficial velocity at 0.858 [m] from the pipe inlet for the churn-annular transition simulated with a 48760 mesh.

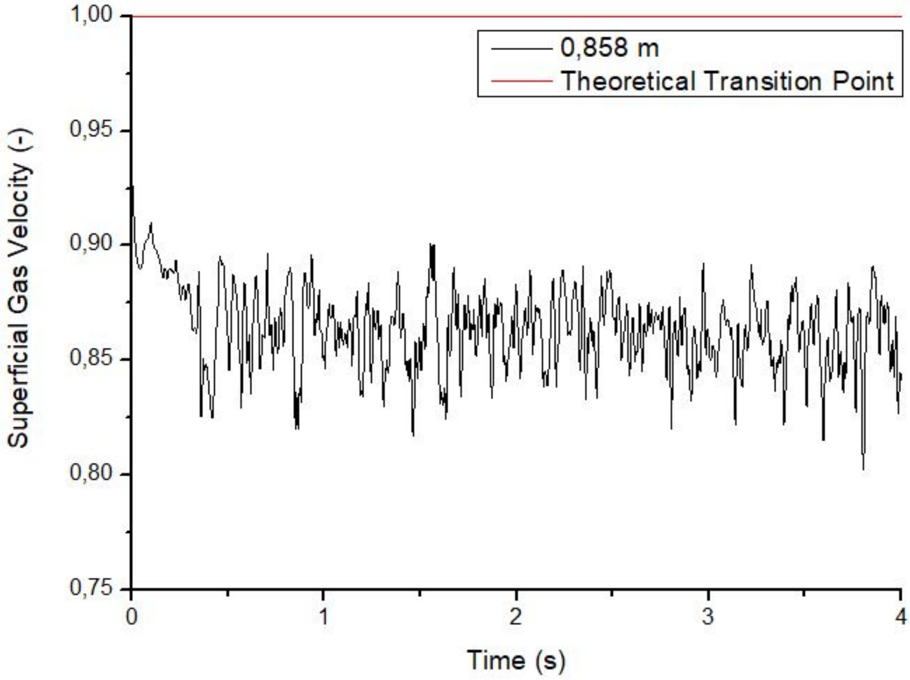

Source: Author (2021).

Figure 42 – Pressure gradient at 0.858 [m] from the inlet for the churn-annular transition simulated with a 48760 mesh.

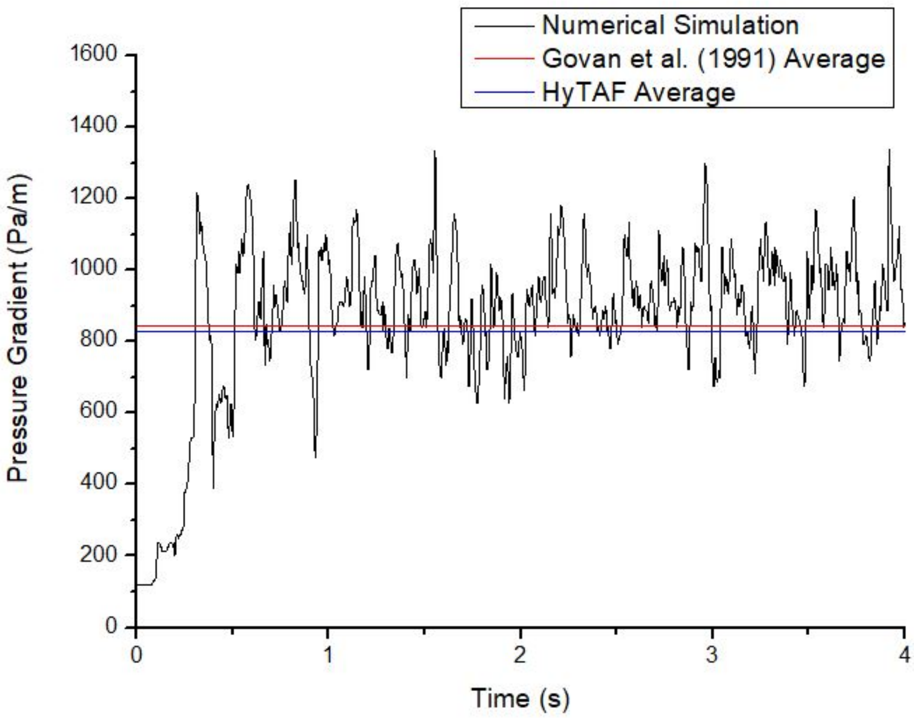

Source: Author (2021).

Figures 43 and 44 show the isosurfaces with 98% air for a short lapse of time, at points located at 0.296 [m] and 1.195 [m] from the pipe inlet, respectively. In Figure 43, the flow is not yet completely developed, as the point located at 0.296 [m] from the tube inlet is very close to the fluid injection point. At this point, it is possible to observe the formation of an unstable liquid film, which presents some undulations and becomes atomized in some parts of the tube. At 1.195 [m] from the pipe inlet, illustrated by Figure 44, the flow is already fully developed and along with an unstable film there are some filaments pulled from the film by shear forces. Unlike annular flow, the simulation with the transition point was able to capture the liquid filaments with the 48760-volume mesh.

Figure 43 – Isosurfaces for churn-annular transition at 0.296 [m] simulated with a 48760 mesh.

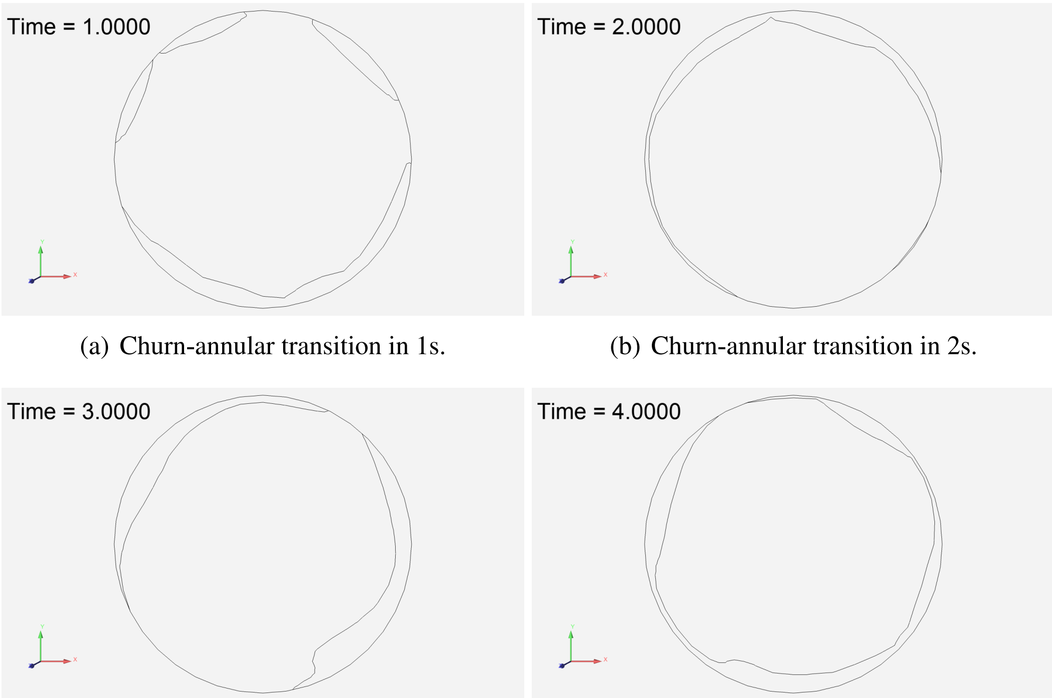

(a) Churn-annular transition in 1s.

(b) Churn-annular transition in 2s.

(c) Churn-annular transition in 3s.

(d) Churn-annular transition in 4s.

Source: Author (2021).

Figure 44 – Isosurfaces for churn-annular transition at 1.195 [m] simulated with a 48760 mesh.

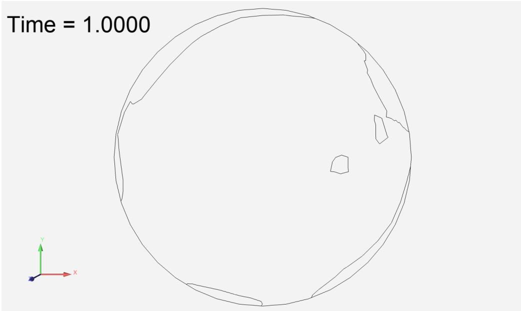

(a) Churn-annular transition in 1s.

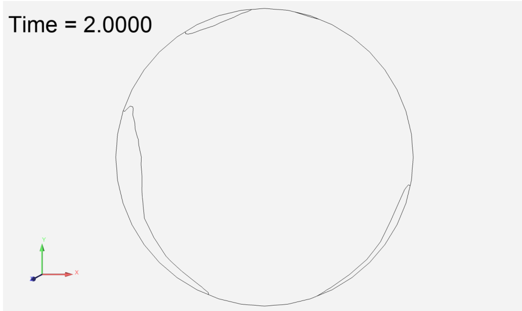

(b) Churn-annular transition in 2s.

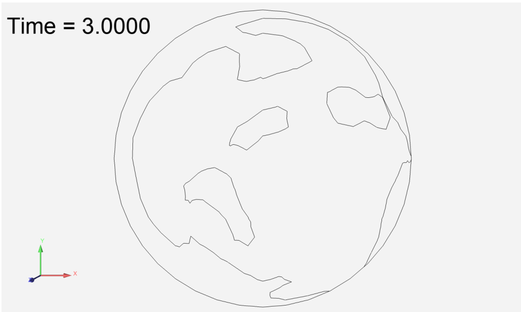

(c) Churn-annular transition in 3s.

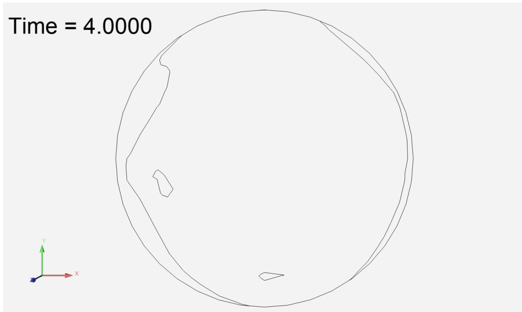

(d) Churn-annular transition in 4s.

Source: Author (2021).

5.2.3 Mesh 4: 186560 Volumes

A simulation for the transition point in a mesh with 186560 volumes was also performed to complete the analysis of the effect of the mesh size on the flow capture. The first parameter obtained was the temporal variation of the void fraction, shown in Figure 45. The fluctuations found in the void fraction are much more accentuated when compared to meshes 1 and 3, indicating that the mesh refining was able to capture greater details of the flow, and of the interaction between the phases. The points where there is a sharp drop in the void fraction probably indicate the passage of a large liquid filament in the pipeline. The relative error calculated between the simulation of the void fraction with this mesh, and the experiment by Govan *et al.* (1991) was 5.82%. For the HyTAF simulations, the relative error was 3.96%.

Figure 46 illustrates the dimensionless gas superficial velocity, measured at three different points: 0.381 [m], 0.858 [m] and 1.227 [m]. Through this figure, the dimensionless gas superficial velocity tends to increase with distance, so that the averages at points 0.381 [m], 0.858 [m] and 1.227 [m] were calculated for the last second of simulation such as 0.809, 0.867 and 0.879, respectively. This indicates that at the points farthest from the duct inlet, the gas fraction should be slightly higher. In addition, in the initial instants there is a greater variation in dimensionless gas superficial velocity, caused by the flow disturbance with the influx of the liquid phase in the pipe. Over time, the oscillations become milder, as the flow tends to reach the steady state.

Figure 45 – Void fraction between the 0.296 [m] and 1.195 [m] planes for the churn-annular transition simulated with a 186560 mesh.

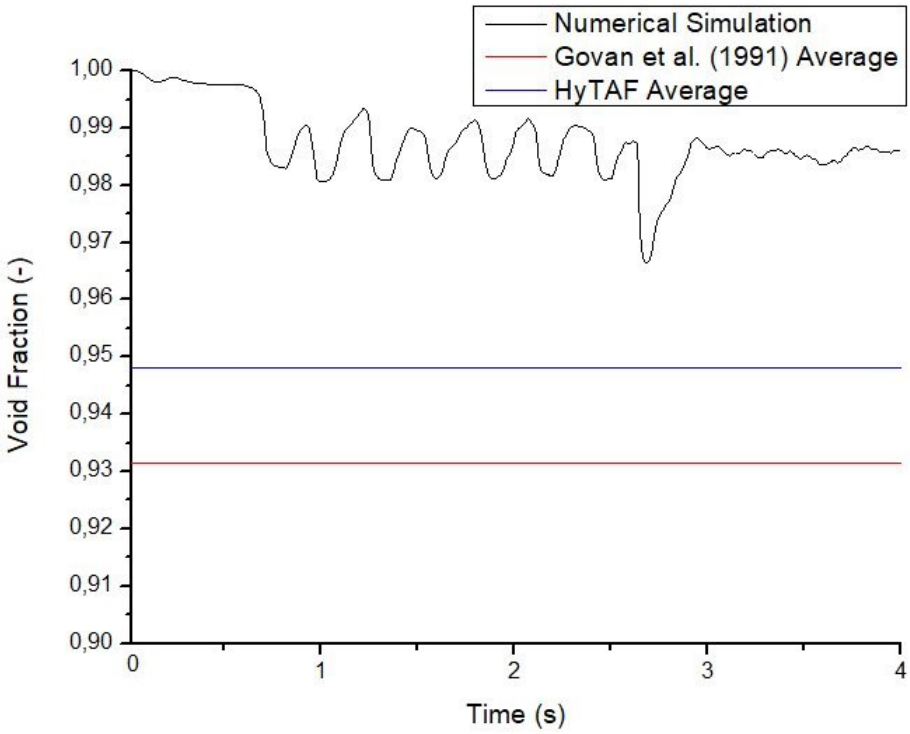

Source: Author (2021).

Figure 46 – Dimensionless gas superficial velocity measured at three different points: 0.381 [m], 0.858 [m] and 1.227 [m].

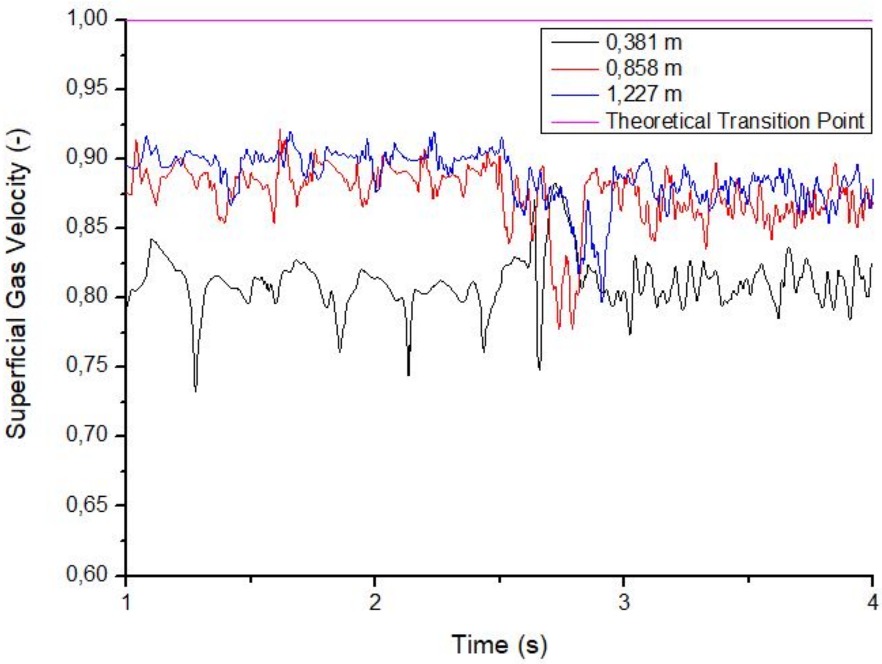

Source: Author (2021).

Figure 47 shows the time variation of the pressure gradient calculated between the plans located at 0.381 [m] and 1.227 [m] from the pipe inlet. As in the graphs of the void fraction, and of the dimensionless gas superficial velocity, fluctuations are more pronounced at the beginning of the simulation, because of the disturbance created in the flow with the insertion of the liquid phase in the tube. The relative error calculated between the simulation of the pressure gradient with mesh 4, and the experiment by Govan *et al.* (1991) was 32.74%. For the HyTAF simulations, the relative error was 35.12%.

Figures 48 and 49 illustrate the 98% air isosurfaces found for the transition at different times, at 0.296 [m] and 1.195 [m]. These figures present a little more detail when compared to Figures 43 and 44, generated by the simulation conducted with mesh 3. As in the previous cases, at 0.296 [m] from the tube inlet, the flow is not yet completely developed, so the simulation captures only a very unstable liquid film. The flow becomes completely developed at a point farther away from the fluid injection, as at the point located 1.195 [m] from the pipe inlet, illustrated by Figure 49.

At this point, in the earliest simulation times an unstable film is being formed, and after three seconds of simulation the flow seems to have reached a steady state, and some liquid filaments are observed. Analyzing the isosurfaces together with the graphs of the void fraction, superficial velocity, and pressure gradient, it is noted that, in fact, the behavior of the parameters illustrated by Figures 45, 46 and 47 changes in approximately three seconds of simulation, indicating the probable onset of a steady-state flow.

Figure 47 – Pressure gradient at 0.858 [m] from the inlet for the churn-annular transition simulated with a 186560 mesh.

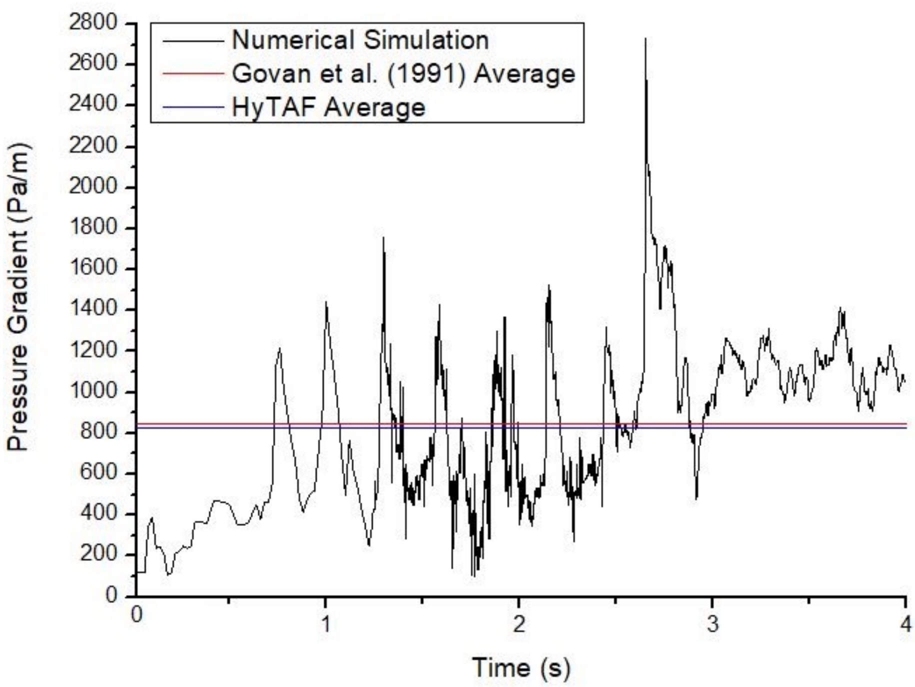

Source: Author (2021).

Figure 48 – Isosurfaces for churn-annular transition at 0.296 [m] simulated with a 186560 mesh.

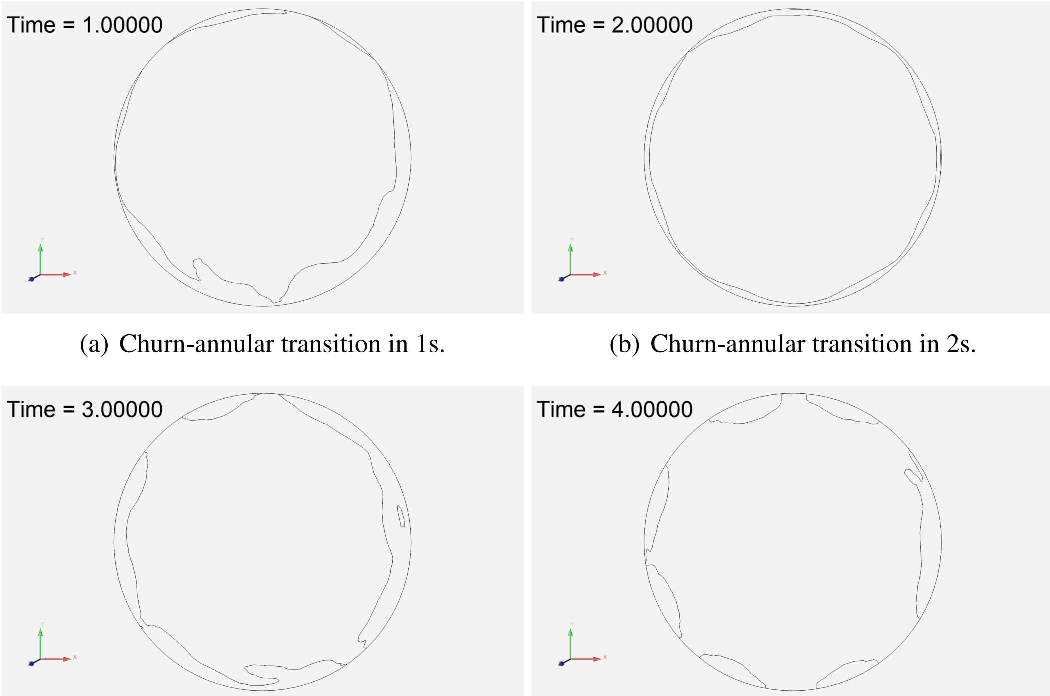

(a) Churn-annular transition in 1s.

(b) Churn-annular transition in 2s.

(c) Churn-annular transition in 3s.

(d) Churn-annular transition in 4s.

Source: Author (2021).

Figure 49 – Isosurfaces for churn-annular transition at 1.195 [m] simulated with a 186560 mesh.

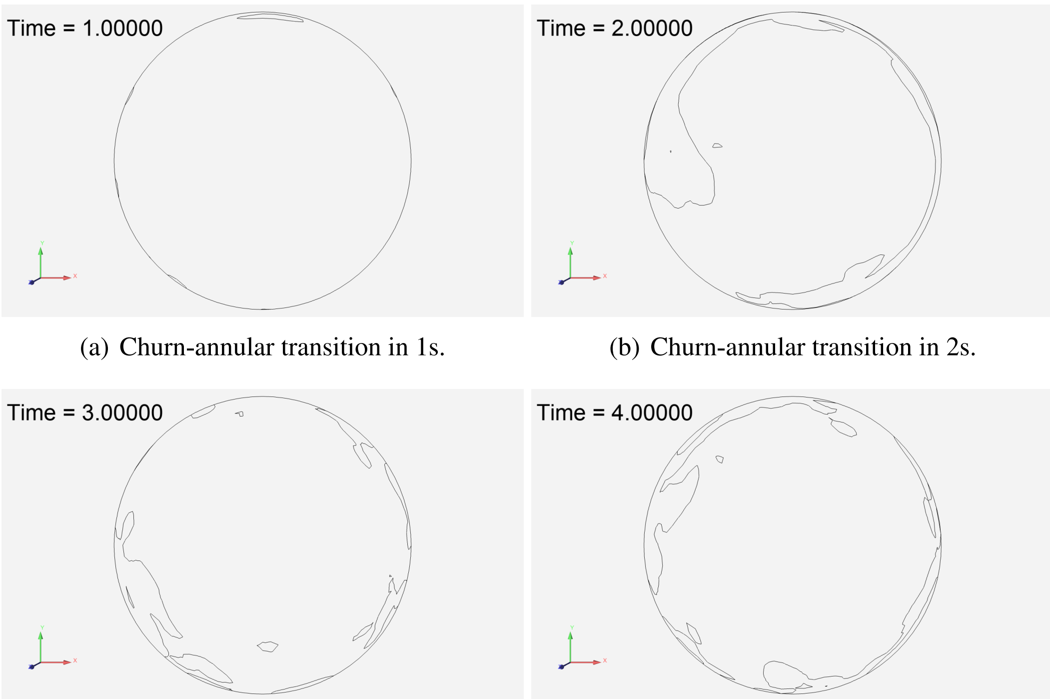

(a) Churn-annular transition in 1s.

(b) Churn-annular transition in 2s.

(c) Churn-annular transition in 3s.

(d) Churn-annular transition in 4s.

Source: Author (2021).

Table 5 summarizes the results found with the three meshes tested for the transition point.

Table 5 – Relative errors found for churn-annular transition.

CHURN-ANNULAR TRANSITION				
Relative Error	*Govan et al. (1991)*		*HyTAF*	
	Void Fraction [-]	Pressure Gradient [Pa/m]	Void Fraction [-]	Pressure Gradient [Pa/m]
Mesh 1	6.31%	13.74%	4.44%	15.78%
Mesh 3	6.18%	11.01%	4.31%	13.00%
Mesh 4	5.82%	32.74%	3.96%	35.12%

Source: Author (2021).

5.3 CHURN FLOW

The third simulated flow condition was the churn flow with a mass flow rate of $1.87x10^{-2}$ $[kg/s]$ for the air and $2.53x10^{-2}$ $[kg/s]$ for the water. The geometry of the piping, the fluids used, and the detailed boundary conditions have already been discussed in chapter 4.

5.3.1 Mesh 1: 15264 Volumes

The first case analyzed for churn flow was with the 15264-volume mesh. The results obtained with this mesh were very similar to those found for the annular flow and for the transition point discussed previously. Figure 50 shows the temporal variation of the void fraction. As in the previous cases, it presents few oscillations, indicating that the mesh is not thin enough to describe the details of the churn flow either. The relative error calculated between the simulation of the void fraction with this mesh and the experiment of Govan *et al.* (1991) was 8.02%. For the HyTAF simulations, the relative error was 5.09%.

Figure 51 presents the variation in the dimensionless gas superficial velocity, calculated at a point located 0.858 [m] from the pipe inlet. As expected, based on previously simulated cases with the same mesh, few oscillations were detected. The pressure gradient calculated between the planes at 0.381 [m] and 1.227 [m] from the pipe inlet is shown in Figure 52, and as in the other parameters found, it presents smooth oscillations after the initial disturbance of the flow with the influx of the liquid phase in the tube. The relative error calculated between the simulation of the pressure gradient with the mesh of 15264 volumes and the experiment by Govan *et al.* (1991) was 11.71%. For the HyTAF simulations, the relative error was 6.43%.

Figures 53 and 54 show the isosurface with 98% air obtained for the churn flow, at 0.296 [m] and 1.195 [m] from the pipe inlet. The behavior of the fluids inside the tube is also very similar to that found for the annular flow and for the transition point simulated with mesh 1. At 0.296 [m] from the tube inlet, the liquid film is very irregular and is still being formed. At point 1.195 [m], although the film still presents an irregular behavior, it acquires a slightly smoother format. In both cases no liquid droplets or filaments are detected by the simulations.

Figure 50 – Void fraction between the 0.296 [m] and 1.195 [m] planes for the churn flow simulated with a 15264 mesh.

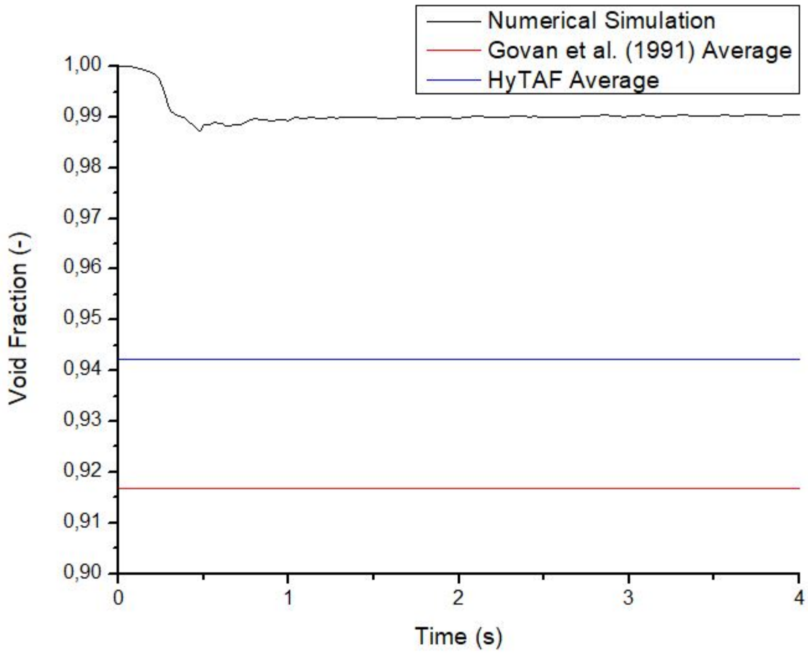

Source: Author (2021).

Figure 51 – Dimensionless gas superficial velocity at 0.858 [m] from the pipe inlet for the churn flow simulated with a 15264 mesh.

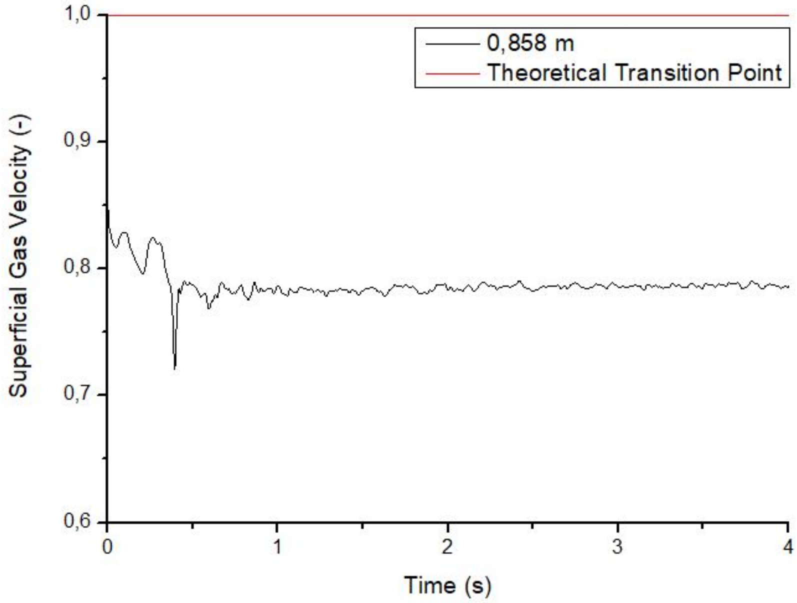

Source: Author (2021).

Figure 52 – Pressure gradient at 0.858 [m] from the inlet for the churn flow simulated with a 15264 mesh.

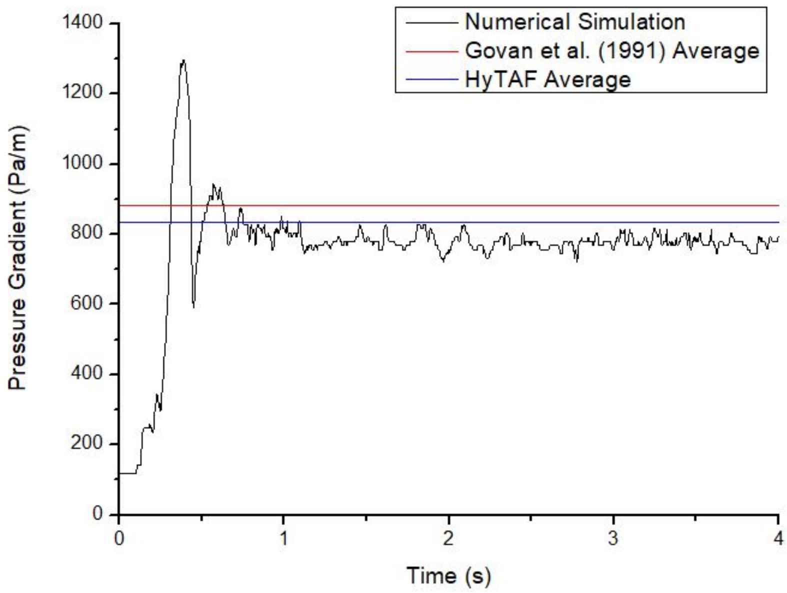

Source: Author (2021).

Figure 53 – Isosurfaces for annular flow at 0.296 [m] simulated with a 15264 mesh.

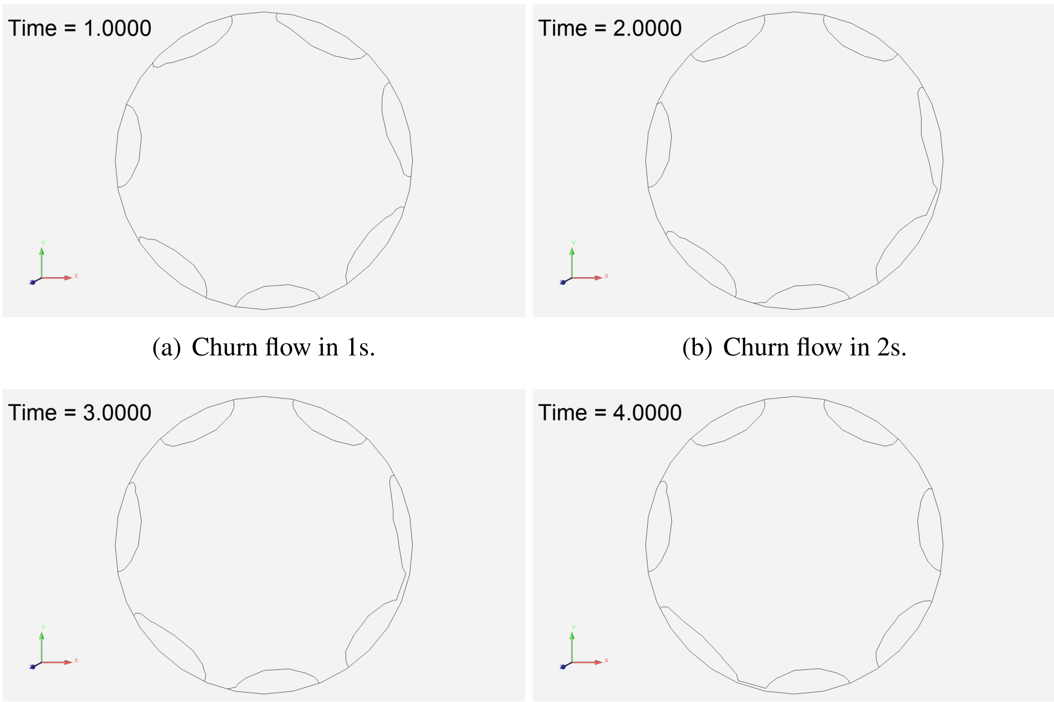

(a) Churn flow in 1s.

(b) Churn flow in 2s.

(c) Churn flow in 3s.

(d) Churn flow in 4s.

Source: Author (2021).

Figure 54 – Isosurfaces for annular flow at 1.195 [m] simulated with a 15264 mesh.

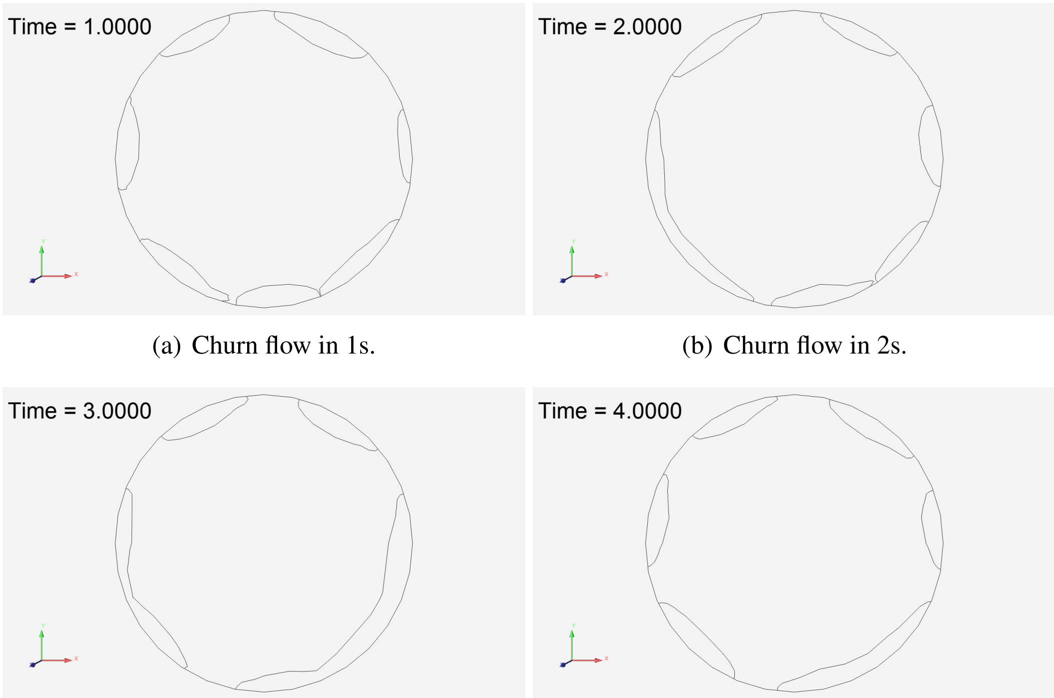

(a) Churn flow in 1s. (b) Churn flow in 2s.

(c) Churn flow in 3s. (d) Churn flow in 4s.

Source: Author (2021).

5.3.2 Mesh 2: 30528 Volumes

A second mesh with 30528 volumes was used to simulate the churn flow. This mesh has the same cross section as mesh 1, with 288 volumes, but it has a greater axial refining, containing 106 volumes. The void fraction found between the planes located at 0.296 [m] and 1.195 [m] from the pipe inlet is presented in Figure 55 below. As in the annular flow, some fluctuations in the gas void fraction are observed, demonstrating that the mesh axial refining was also able to capture the flow details and the interaction between the liquid and gas phases in the churn flow. The relative error calculated between the simulation of the void fraction with this mesh and the experiment by Govan *et al.* (1991) was 7.81%. For the HyTAF simulations, the relative error was 4.88%.

Figure 56 shows fluctuations in the dimensionless gas superficial velocity calculated at a point located 0.858 [m] from the pipe inlet. Regarding the annular flow, the gas superficial velocity is much smaller, consistently with what is expected, since in theory the churn flow should assume values below one.

Figure 55 – Void fraction between the 0.296 [m] and 1.195 [m] planes for the churn flow simulated with a 30528 mesh.

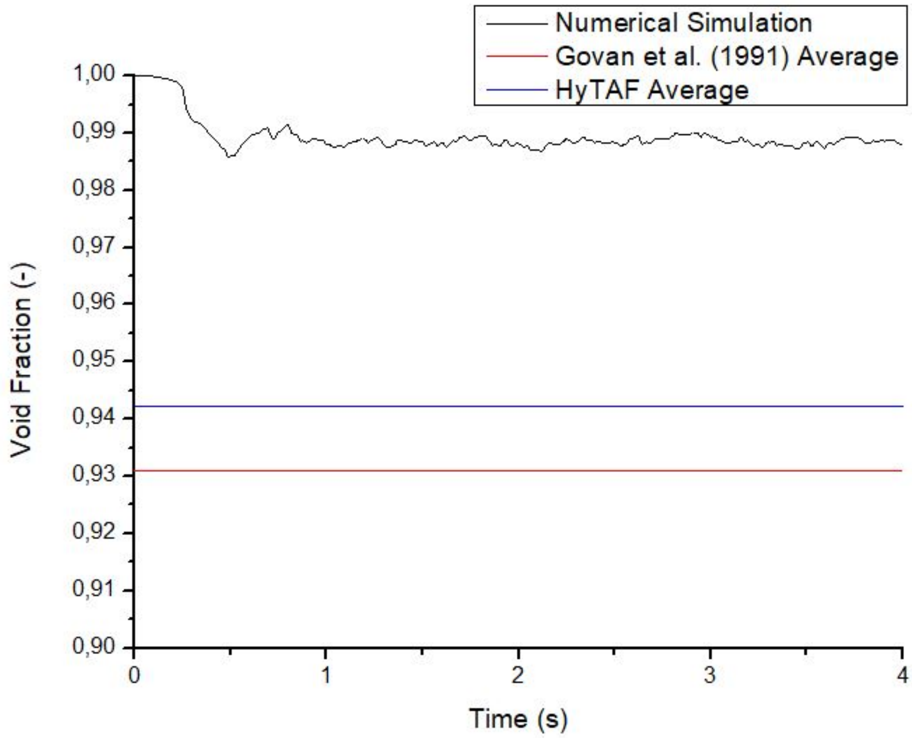

Source: Author (2021).

Figure 57 shows the time variation of the pressure gradient calculated between the planes located at 0.381 [m] and 1.227 [m] from the pipe inlet. The simulation detected large fluctuations, probably caused by the instability of the liquid film in the churn flow. The relative error calculated between the simulation of the pressure gradient with mesh 2 and the experiment by Govan *et al.* (1991) was 4.55%. For the HyTAF simulations, the relative error was 1.16%.

To analyze the real behavior of the flow inside the tube, isosurfaces with 98% air were obtained for the churn flow at different times, at points 0.296 [m] and 1.195 [m]. These isosurfaces are represented by Figures 58 and 59, respectively. The simulation conducted with the axially refined mesh, captured a liquid film with several undulations. The thickness of the film varies substantially with time, and this phenomenon is probably responsible for the variations found in the gas void fraction, since no filaments or liquid droplets are observed in this case. The axial refinement was not able to capture all the effects of the chaotic churn flow, probably because the refinement used in the cross section was the same as in mesh 1, with only 288 volumes. As in annular flow, the liquid film continues to run out even when the flow is already fully developed, which is an inconsistency found in the model.

Figure 56 – Dimensionless gas superficial velocity at 0.858 [m] from the pipe inlet for the churn flow simulated with a 30528 mesh.

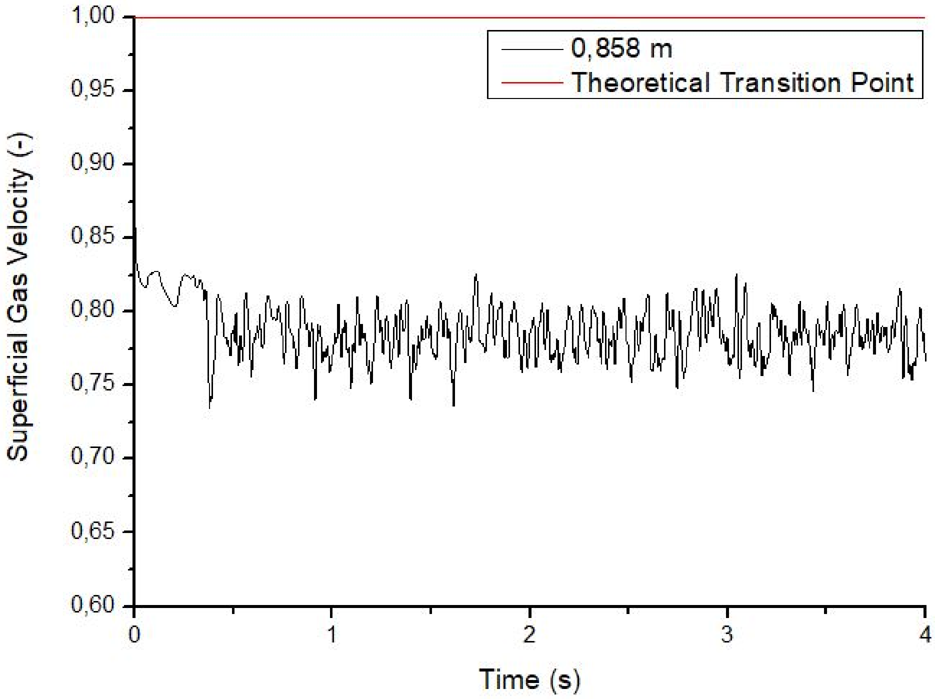

Source: Author (2021).

Figure 57 – Pressure gradient at 0.858 [m] from the inlet for the churn flow simulated with a 30528 mesh.

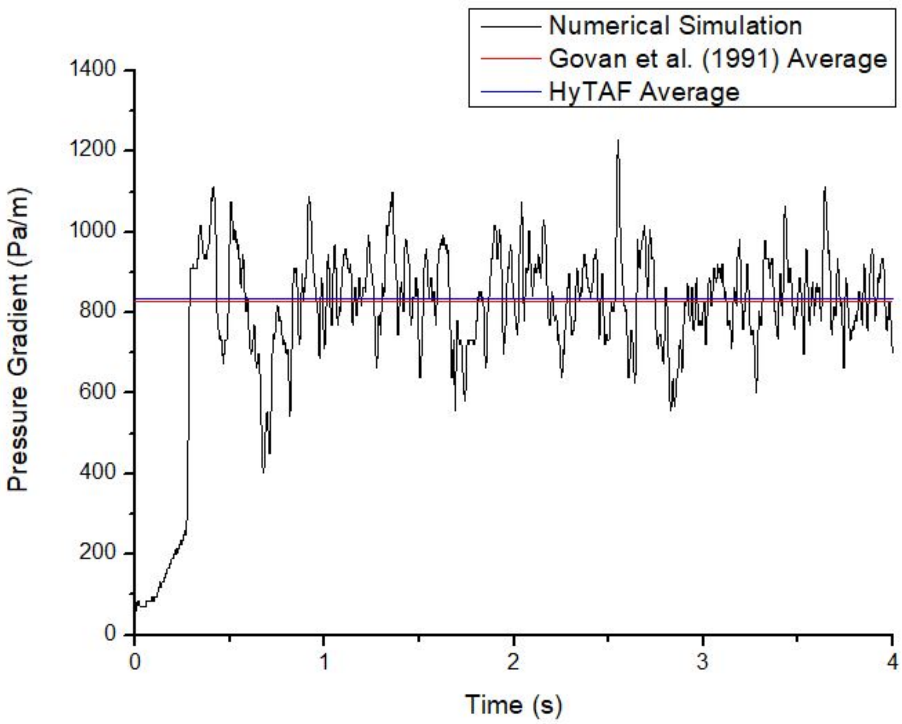

Source: Author (2021).

Figure 58 – Isosurfaces for churn flow at 0.296 [m] simulated with a 30528 mesh.

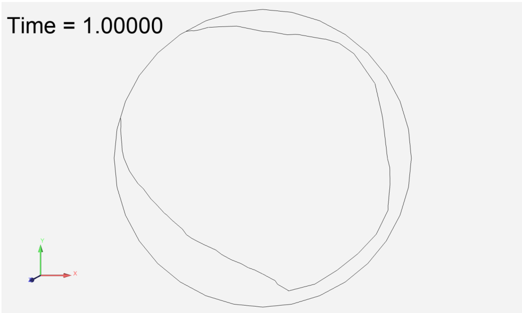

(a) Churn flow in 1s.

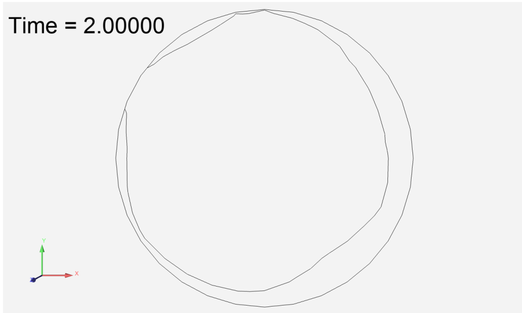

(b) Churn flow in 2s.

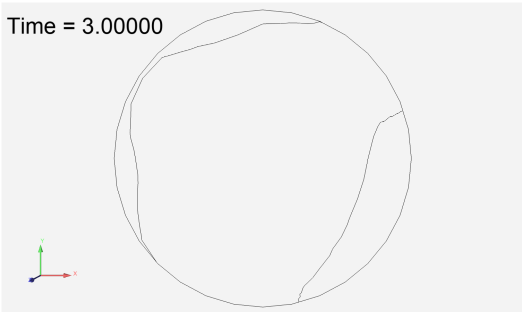

(c) Churn flow in 3s.

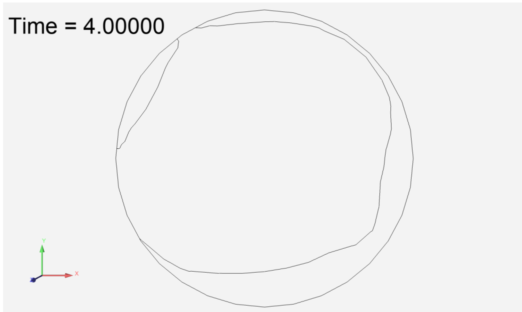

(d) Churn flow in 4s.

Source: Author (2021).

Figure 59 – Isosurfaces for churn flow at 1.195 [m] simulated with a 30528 mesh.

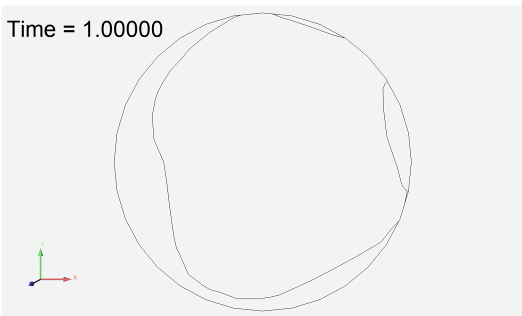

(a) Churn flow in 1s.

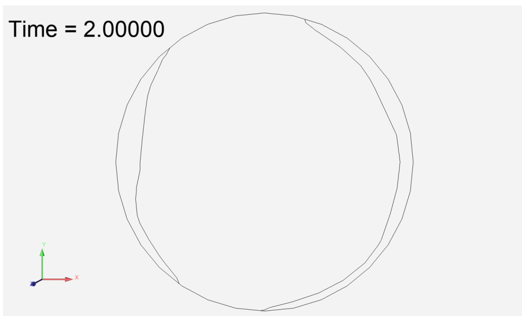

(b) Churn flow in 2s.

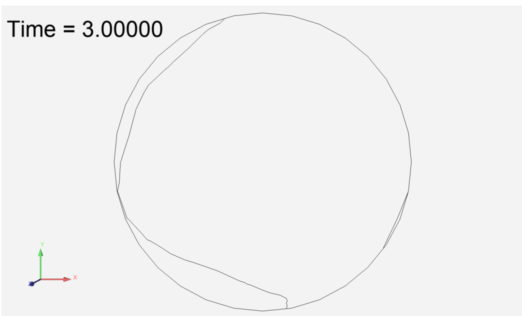

(c) Churn flow in 3s.

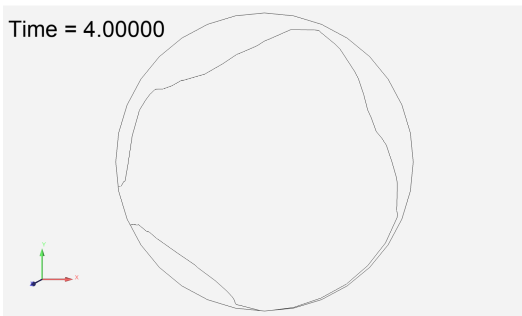

(d) Churn flow in 4s.

Source: Author (2021).

5.3.3 Mesh 3: 48760 Volumes

The third case studied was the churn flow with the same boundary conditions, in a mesh with 48760 volumes. The first parameter obtained was the temporal variation of the gas void fraction, shown in Figure 60. The initial drop indicates the influx of the liquid phase in the tube, and the oscillations observed over time represent the interaction with the liquid phase which, in the case of churn flow, may be indicative of the passage of interfacial waves and liquid filaments. The relative error calculated between the simulation of the void fraction with the third grid and the experiment by Govan *et al.* (1991) was 7.70%. For the HyTAF simulations, the relative error was 4.77%.

Figure 61 presents the temporal variation of the dimensionless gas superficial velocity at 0.858 [m] from the pipe inlet. Its behavior is very similar to that obtained with mesh 2, which presents some oscillations but remains at a value below the theoretical transition point.

Figure 60 – Void fraction between the 0.296 [m] and 1.195 [m] planes for the churn flow simulated with a 48760 mesh.

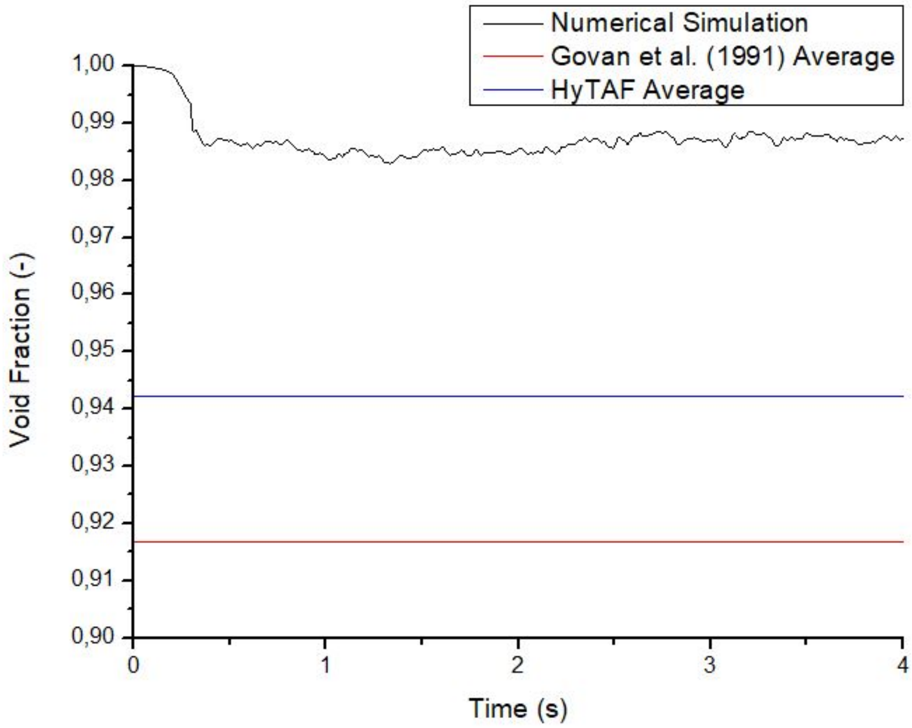

Source: Author (2021).

Figure 62 shows the time variation of the pressure gradient calculated between the planes located at 0.381 [m] and 1.227 [m] from the pipe inlet. It is possible to observe large fluctuations that can be attributed, in part, to the liquid filaments that flow through the duct causing a strangulation of the gas phase and, consequently, generating an oscillation in the pressure. In addition, another factor that contributes to a greater pressure fluctuation is that the liquid filaments flow at a velocity lower than that of the gas, thus causing a greater consumption of flow energy when they are accelerated towards the end of the tube. The relative error calculated between the simulation of the pressure gradient with the third mesh and the experiment by Govan *et al.* (1991) was 0.52%. For the HyTAF simulations, the relative error was 5.43%.

Figures 63 and 64 illustrate the 98% air isosurfaces found for the churn flow at points 0.296 [m] and 1.195 [m]. At 0.296 [m] from the inlet, the simulation detected an unstable liquid film that begins to form with the injection of the liquid phase into tube. The point located at 1.195 [m] from the inlet, on the other hand, is located farther away from the liquid injection point, and therefore the flow is completely developed. Thus, it is possible to identify small filaments that flow through the gas core formed by the collapsed Taylor bubbles. Even with the 48760-volume mesh, the liquid film continues to run out, not fully encompassing the tube diameter.

Figure 61 – Dimensionless gas superficial velocity at 0.858 [m] from the pipe inlet for the churn flow simulated with a 48760 mesh.

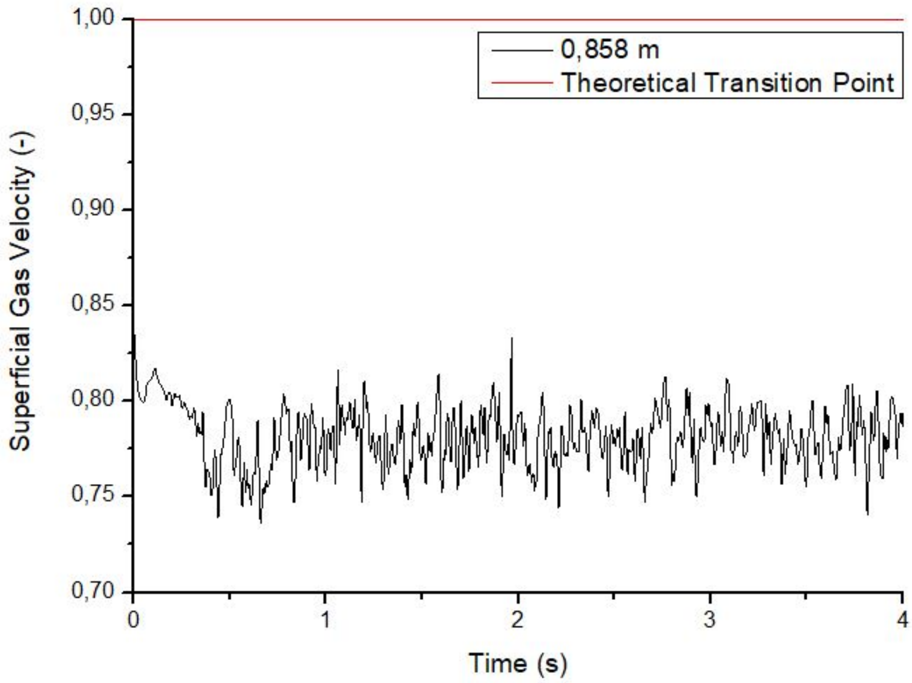

Source: Author (2021).

Figure 62 – Pressure gradient at 0.858 [m] from the inlet for the churn flow simulated with a 48760 mesh.

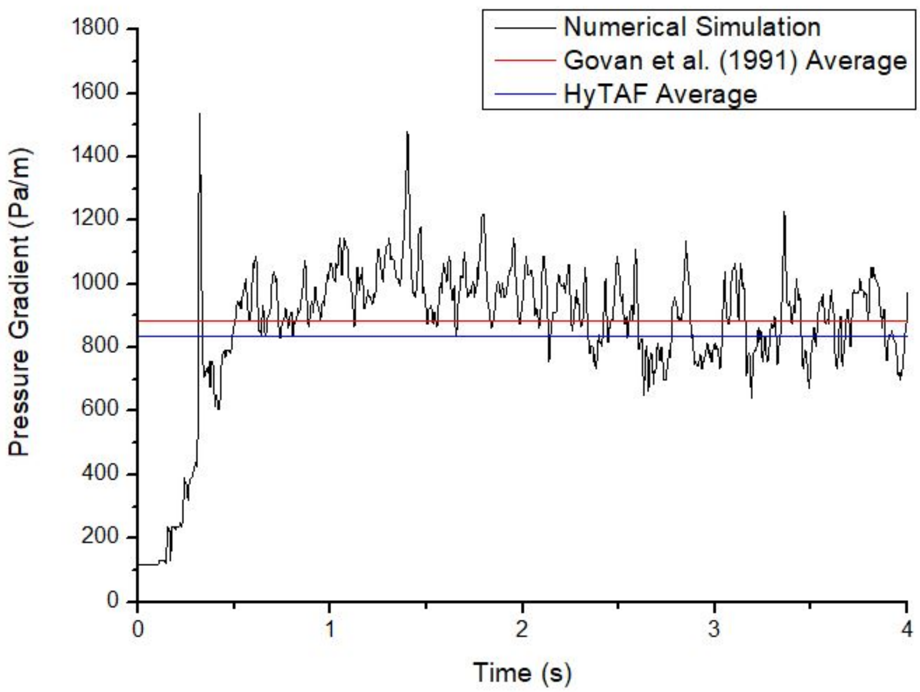

Source: Author (2021).

Figure 63 – Isosurfaces for churn flow at 0.296 [m] simulated with a 48760 mesh.

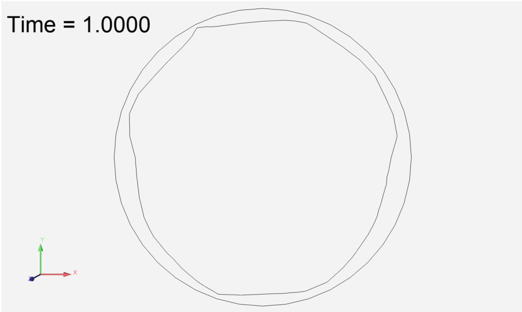

(a) Churn flow in 1s.

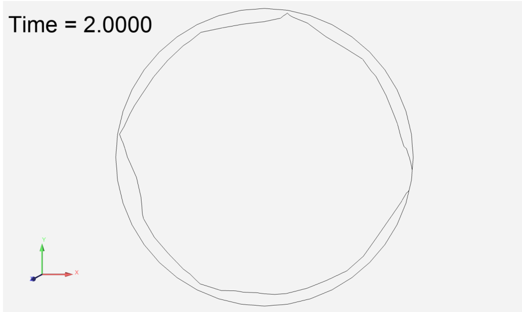

(b) Churn flow in 2s.

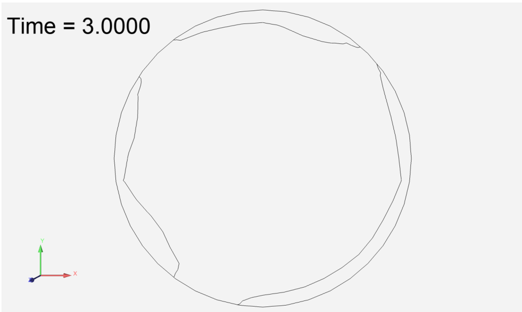

(c) Churn flow in 3s.

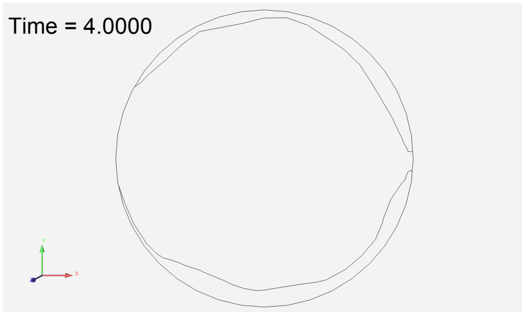

(d) Churn flow in 4s.

Source: Author (2021).

Figure 64 – Isosurfaces for churn flow at 1.195 [m] simulated with a 48760 mesh.

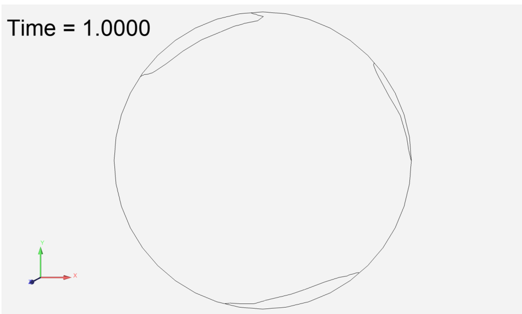

(a) Churn flow in 1s.

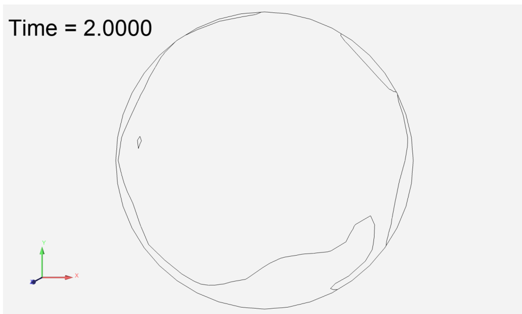

(b) Churn flow in 2s.

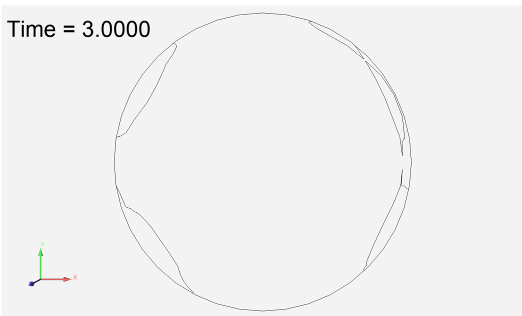

(c) Churn flow in 3s.

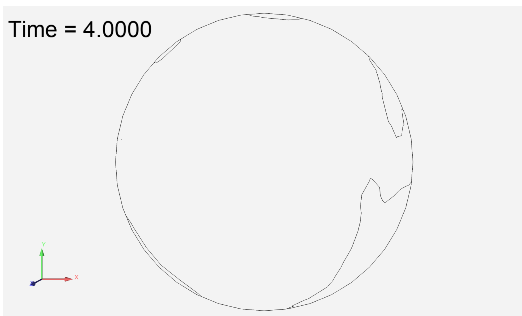

(d) Churn flow in 4s.

Source: Author (2021).

5.3.4 Mesh 4: 186560 Volumes

A simulation for the churn flow in a mesh with 186560 volumes was performed to complete the analysis of the effect of the mesh refinement on the flow capture. The behavior of the void fraction, shown in Figure 65, is very similar to that found in the simulation conducted with a mesh of 48760 volumes. The simulation was able to capture oscillations in the void fraction that probably indicate the interaction between the phases, through the presence of interfacial waves and liquid filaments. The relative error calculated between the simulation of the void fraction with mesh 4 and the experiment by Govan *et al.* (1991) was 7.71%. For the HyTAF simulations, the relative error was 4.78%.

Figure 65 – Void fraction between the 0.296 [m] and 1.195 [m] planes for the churn flow simulated with a 186560 mesh.

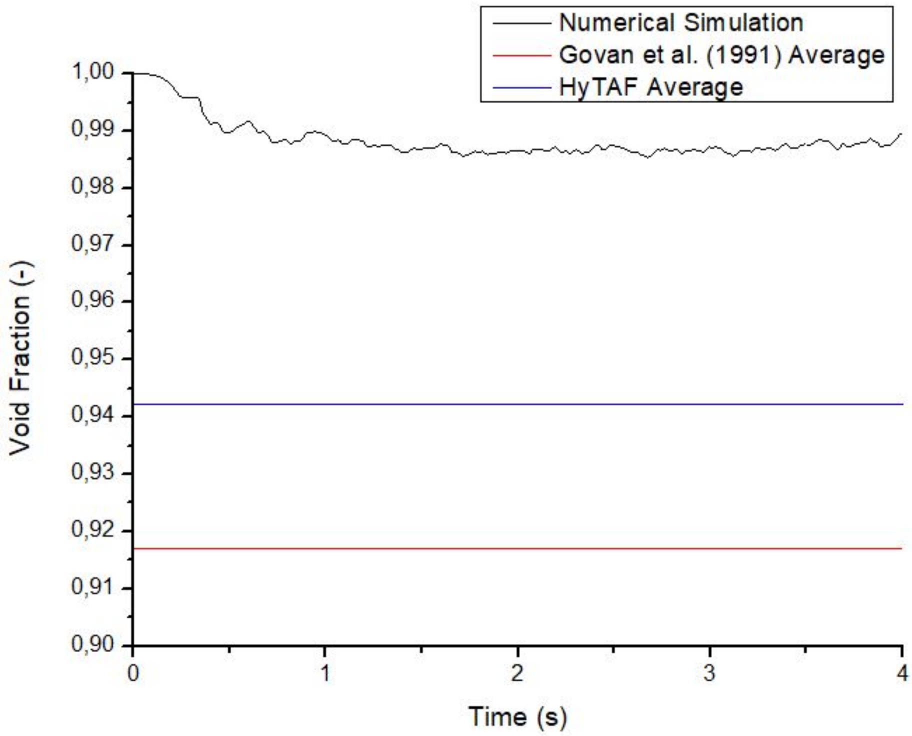

Source: Author (2021).

To analyze the influence of position in the dimensionless gas superficial velocity with mesh 4, this parameter was measured at three different points: 0.381 [m], 0.858 [m] and 1.227 [m], and is illustrated in Figure 66. Through this figure, the gas superficial velocity tends to increase with distance, so that the averages at points 0.381 [m], 0.858 [m] and 1.227 [m] were calculated for the last simulation second as 0.741, 0.784 and 0.791, respectively. This indicates that at the points farthest from the duct inlet, the gas fraction should be slightly higher.

Figure 67 shows the temporal variation of the pressure gradient calculated between the planes located at 0.381 [m] and 1.227 [m] from the pipe inlet. Again, the simulation detected large fluctuations, and the mean value of the simulations for the pressure gradient found is slightly lower when compared to mesh 3. The relative error calculated between the pressure gradient simulation with mesh 4 and the experiment of Govan *et al.* (1991) was 1.41%. For the HyTAF simulations, the relative error was 7.48%.

Figures 68 and 69 illustrate the 98% air isosurfaces found for the churn flow at different times, at points 0.296 [m] and 1.195 [m]. Through the analysis of these figures, the simulation is similar to the geometry of the churn flow found in the literature, and the mesh used with 186560 volumes was able to capture more details of churn flow. Different from what occurs in mesh 3, it is possible to observe an oscillating film and liquid filaments at the point closest to the inlet, located at 0.296 [m], even before the flow is completely developed. At the farthest point, located at 1.195 [m] from the inlet, the oscillations are even more perceptible, and more filaments and drops can be observed. It is important to note that even with the finer mesh, the liquid film continued to run out. Hence, it was not possible to accurately describe the oscillating liquid film of the churn flow even with the 186560-volume mesh.

Although the graphical results of the void fraction, dimensionless gas superficial velocity and pressure gradient, illustrated by Figures 65, 66 and 67, are very similar to those obtained through simulation with the 30528-volume mesh, the isosurfaces found with meshes 2 and 4 are completely different.

Figure 66 – Dimensionless gas superficial velocity measured at three different points: 0.381 [m], 0.858 [m] and 1.227 [m].

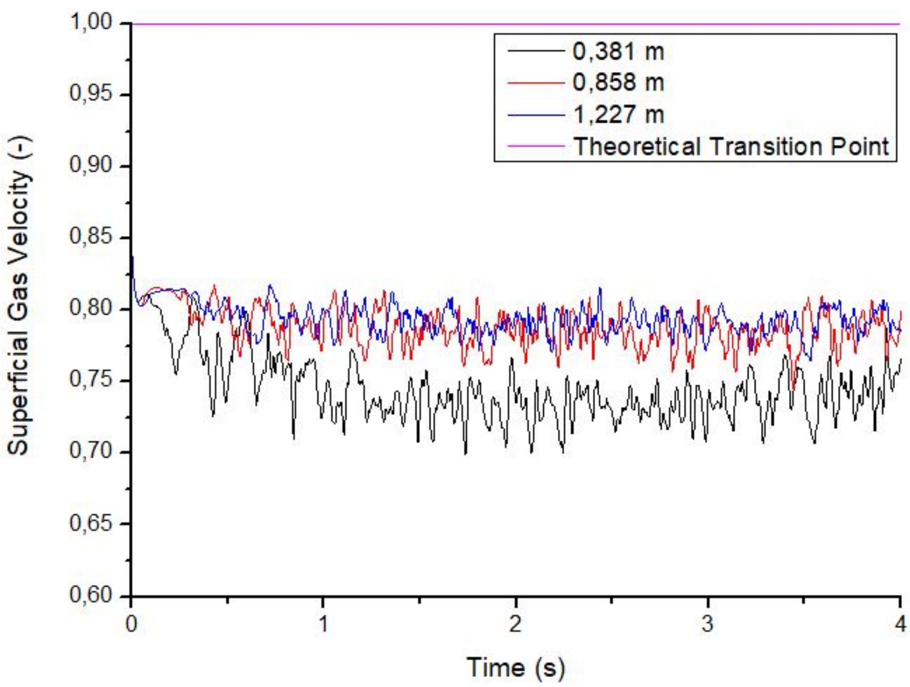

Source: Author (2021).

Figure 67 – Pressure gradient at 0.858 [m] from the inlet for the churn flow simulated with a 186560 mesh.

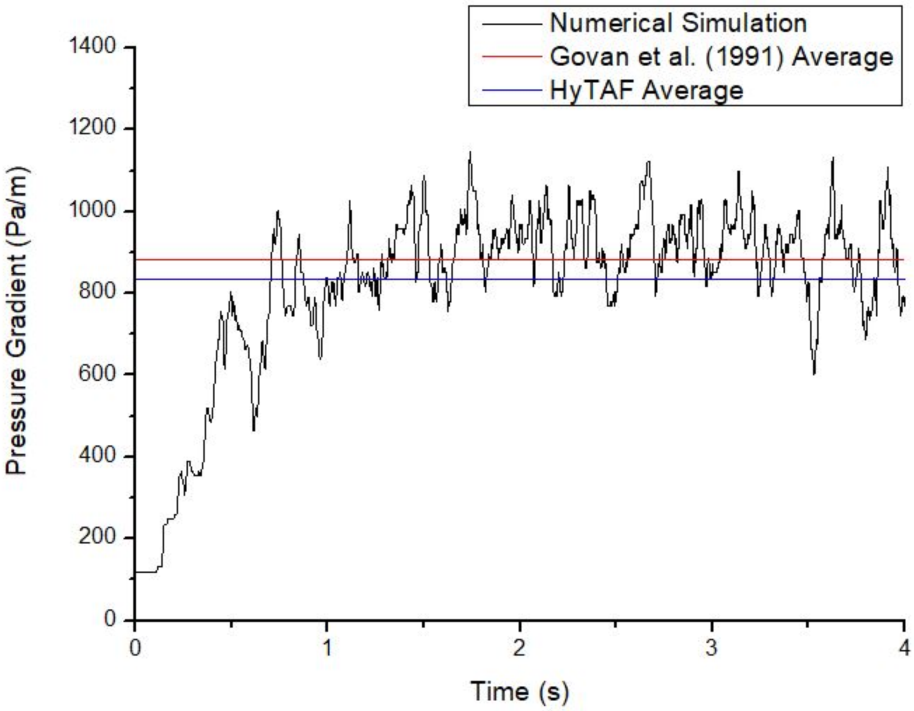

Source: Author (2021).

Figure 68 – Isosurfaces for churn flow transition at 0.296 [m] simulated with a 186560 mesh.

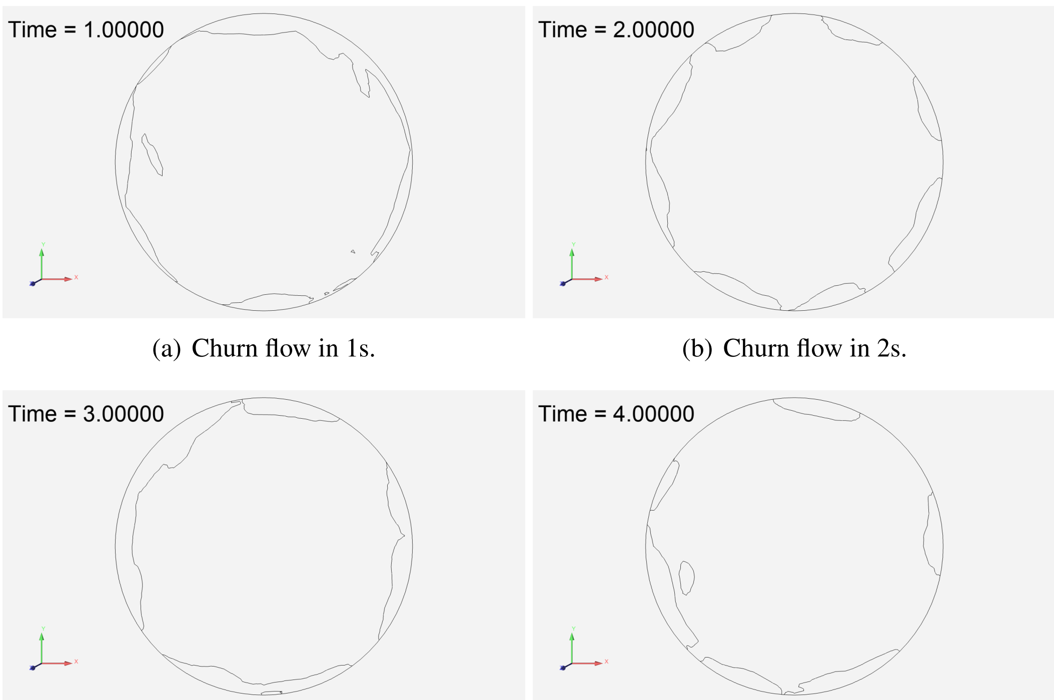

(a) Churn flow in 1s.

(b) Churn flow in 2s.

(c) Churn flow in 3s.

(d) Churn flow in 4s.

Source: Author (2021).

Figure 69 – Isosurfaces for churn flow transition at 1.195 [m] simulated with a 186560 mesh.

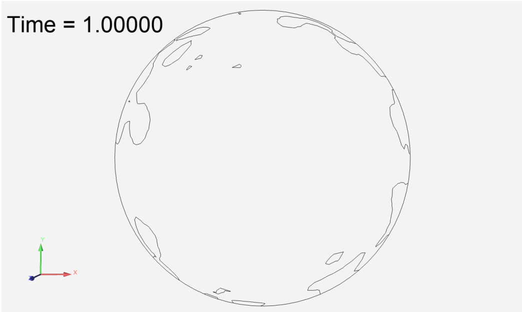

(a) Churn flow in 1s.

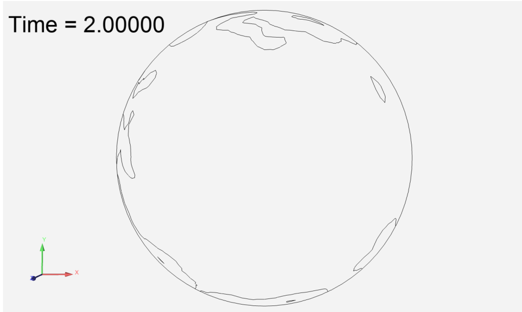

(b) Churn flow in 2s.

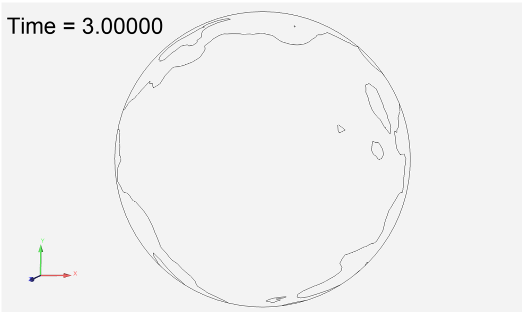

(c) Churn flow in 3s.

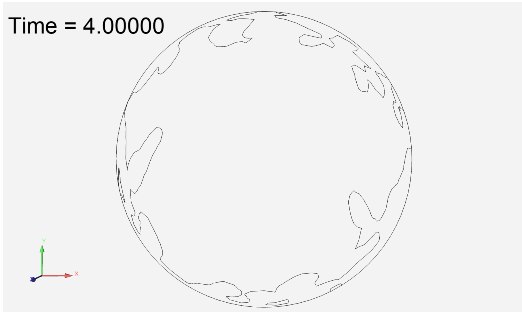

(d) Churn flow in 4s.

Source: Author (2021).

Table 6 summarizes the results found with the four meshes tested for the churn flow.

Table 6 – Relative errors found for churn flow.

CHURN FLOW				
Relative Error	*Govan et al. (1991)*		*HyTAF*	
	Void Fraction [-]	Pressure Gradient [Pa/m]	Void Fraction [-]	Pressure Gradient [Pa/m]
Mesh 1	8.02%	11.71%	5.09%	6.43%
Mesh 2	7.81%	4.55%	4.88%	1.16%
Mesh 3	7.70%	0.52%	4.77%	5.43%
Mesh 4	7.71%	1.41%	4.78%	7.48%

Source: Author (2021).

5.4 PRESSURE GRADIENT COMPARISON

Figure 70 below summarizes the results obtained for the pressure gradient with the 186560-volume mesh in the annular and churn patterns, as well as in the transition between these flow regimes. The comparison with the experiment conducted by Govan *et al.* and the HyTAF code simulations (ALVES, 2014; ALVES *et al.*, 2017) is also presented.

Through Figure 70, it is noticed that for the churn flow the relative errors found are significantly smaller when compared to the transition point and the annular flow. This occurs because the velocity difference between the phases is smaller, which generates less numerical diffusion. In addition, despite the 186560-volume mesh presenting more flow details than the thicker meshes, it presented a greater relative error regarding the Govan *et al.* (1991) experiment, and the HyTAF data. The finest mesh is not always the one with the best quality, because when the size of the cells is greatly reduced, they may flatten, worsening the aspect ratio, which is one of the factors used to check the quality of a mesh. Ideally, the aspect ratio should be equal to one to guarantee the best results, it is likely that the aspect ratio of mesh 4 is high, since it has a large cross-sectional refinement, containing 1760 volumes, and only 106 volumes in the axial.

Figure 70 – Pressure gradients calculated with the 186560-volume mesh.

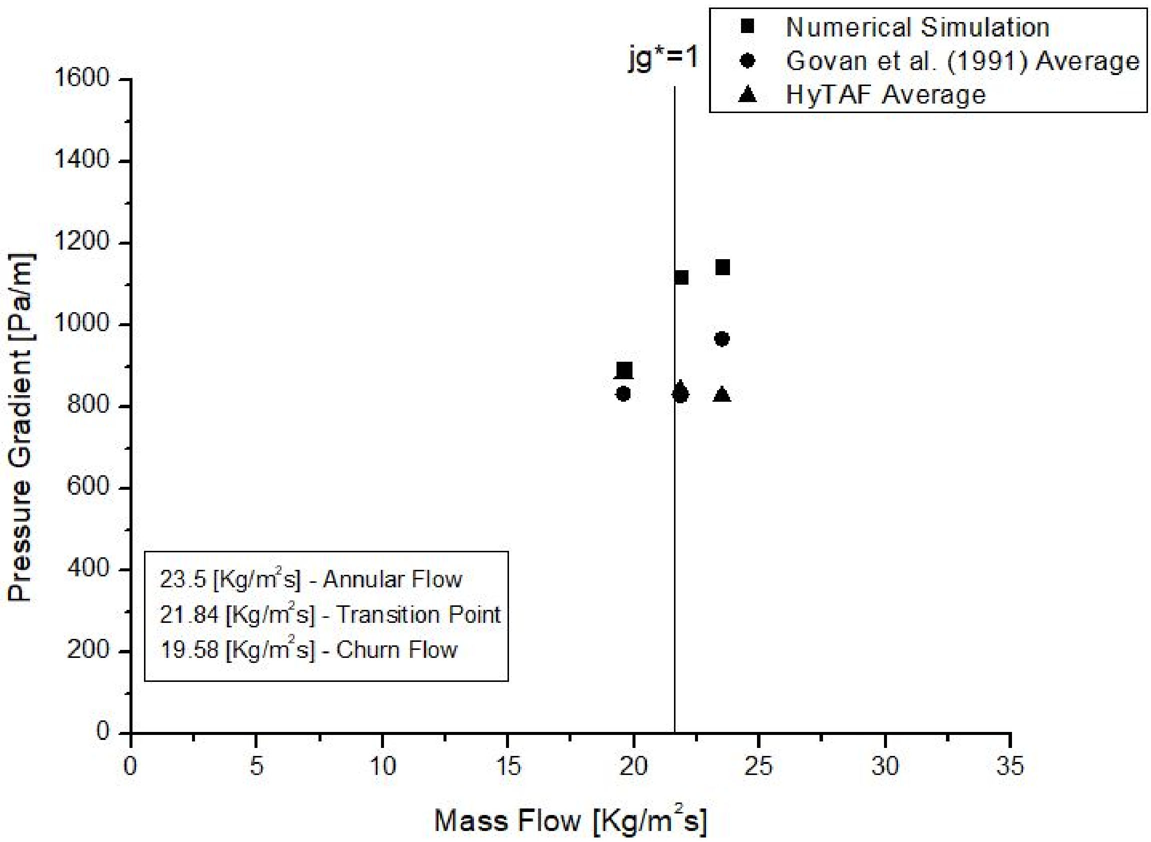

Source: Author (2021).

6 CONCLUSIONS

This work presented transient and three-dimensional investigations of the annular and churn liquid-gas flow patterns, as well as the transition between them. The hybrid `multiphaseEulerFoam` algorithm, which couples the characteristics of the Eulerian-Eulerian method (two fluid model) and the interface capture method (VOF), was used to conduct the simulations that were performed with the aid of the commercial OpenFOAM software. The experiments by Govan *et al.* (1991) served as a basis for the creation of the problem geometry and for the input of the initial and boundary conditions into the program. Four different meshes to verify the influence of the mesh refining on the numerical solution were simulated.

The simulations performed with the 15264-volume mesh did not present a very detailed result about the flow. In all cases the simulation captured very unstable liquid films and few oscillations were identified in the void fractions and in the other measured parameters. The isosurfaces confirmed that this mesh was not able to capture the passage of filaments or liquid droplets through the duct, for any of the flow patterns tested.

A second mesh with 30528 volumes was used to simulate the annular and churn flows. This mesh had the same cross section as mesh 1, with 288 volumes. However, it presented a greater axial refinement containing 106 volumes. In both cases, the simulations detected large fluctuations in the measured parameters, and the 98% air isosurfaces showed a great variation in the liquid film thicknesses over time. This variation in the film thickness is the possible cause of the fluctuations found in the void fraction, in the dimensionless gas superficial velocity and in the pressure gradient. In both cases, no liquid droplets or filaments were found in the simulation, probably because the refinement used in the cross section was the same as in mesh 1, with only 288 volumes.

The simulations conducted with the 48760-volume mesh presented, in general, the smallest relative errors when compared with the experiment of Govan *et al.* (1991) and with HyTAF simulations. The simulation was able to capture fluctuations and some details of annular and churn flows, and the transition between these flow regimes. In the annular flow it was not possible to detect, with this mesh, the liquid droplets that should be released from the film by shear forces. However, at the transition point and churn flow, the simulation was able to capture some liquid filaments dispersed in the gas phase.

In the simulations conducted with the 186560-volume mesh, more oscillations appeared in the measured parameters, and the isosurfaces presented a little more detail of the flows when compared to the 48760-volume mesh. This mesh captured liquid filaments in all tested cases, and was the only mesh capable of capturing this phenomenon in the annular flow, where the dispersed structures are smaller. Despite presenting more details in relation to other meshes, it presented a greater relative error when compared to the experiment by Govan *et al.* (1991) and with HyTAF simulations. This occurs because the finest mesh is not always the one with the best quality. When the size of the cells is reduced, they may flatten, worsening the aspect ratio, which is one of the factors used to check the quality of a mesh. Ideally, the aspect ratio should be equal to one to ensure the best results, it is likely that the aspect ratio of mesh 4 is high, since it has a large cross-sectional refining, containing 1760 volumes, and only 106 volumes in the axial.

In general, the relative errors found for the churn flow were much smaller than those found for the annular flow and for the transition point. This is because the velocity difference between the phases is lower, which generates less numerical diffusion. In addition, the calculated void fractions are overestimated, as the liquid droplets are much smaller than the tested meshes and could not be captured by the simulations even with the finest mesh. With the computers available for this work, it was only possible to create meshes that could capture the largest filaments of the flow patterns. One key feature of churn flow that simulations could not accurately capture is the oscilating liquid film at the wall.

The results presented are reasonable, especially for churn flow, where there is less numerical diffusion. In all tested cases, a small inconsistency was found in the model, since the simulations detected a non-continuous liquid film, which runs out in some regions of the tube wall and does not fully encompass the circumference. Several factors may have caused this inconsistency, such as the meshes used (aspect ratio and size), an inefficient capture of the interface (the VOF model per se), the surface tension modeling or even deficiency in friction shear stress modeling between phases.

It was possible to achieve the objectives of this work by describing the annular flow, the churn flow and the transition between them in a global way with a small difference in relation to the experiment conducted by Govan *et al*. (1991), still managing to reproduce characteristics of entrainment and deposition that only models based on experimental relationships can achieve.

As a suggestion for future works it would be interesting to perform the mesh tests while attempting to improve the grid aspect ratio. Another option for a future work would be to simulate the complete test section presented by Govan *et al.* (1991). This would address the inability of the current tests in capturing the oscilating film for churn flow and provide means to investigate the flow reversal phenomenon.

REFERENCES

ALIYU, Aliyu Musa *et al.* Interfacial friction in upward annular gas–liquid two-phase flow in pipes. **Experimental Thermal and Fluid Science**, v. 84, p. 90-109, 2017.

ALVES, Marcus Vinícius C. *et al.* Modeling transient churn-annular flows in a long vertical tube. **International Journal of Multiphase Flow**, v. 89, p. 399-412, 2017.

ALVES, M. V. C. **Modelagem numérica do escoamento transiente churn-anular em tubulações verticais e sua aplicação na simulação de carga de líquido em poços de gás**. 2014. 287 f. Tese (Doutorado) - Curso de Engenharia Mecânica, Universidade Federalde Santa Catarina, Florianópolis, 2014.

ANSYS INC. (Estados Unidos). **ANSYS Fluent User's Guide**, 2013. 2692 f.

BARBOSA, Jader Riso. **Phase change of single component fluids and mixtures in annular flow**. 2001. Tese de Doutorado. University of London-Imperial College London.

BEERENS, J. C. **Lubricated transport of heavy oil: Simulation of multiphase flow with OpenFOAM**. 2013.

BOYKO, L. D.; KRUZHILIN, G. N. **Heat transfer and hydraulic resistance during condensation of steam in a horizontal tube and in a bundle of tubes**. International Journal of Heat and Mass Transfer, v. 10, n. 3, p. 361-373, 1967.

BRACKBILL, Jeremiah U.; KOTHE, Douglas B.; ZEMACH, Charles. A continuum method for modeling surface tension. **Journal of computational physics**, v. 100, n. 2, p. 335-354, 1992.

BRAUNER, Neima; BARNEA, Dvora. Slug/churn transition in upward gas-liquid flow. **Chemical engineering science**, v. 41, n. 1, p. 159-163, 1986.

BRENNEN, Christopher Earls; BRENNEN, Christopher E. **Fundamentals of multiphase flow**. Cambridge university press, 2005.

CENGEL, Yunus A.; CIMBALA, John M. Properties of fluids. **Fluid Mechanics: Fundamentals and Applications**, p. 37-73, 2014.

CERNE, Gregor; PETELIN, Stojan; TISELJ, Iztok. Coupling of the interface tracking and the two-fluid models for the simulation of incompressible two-phase flow. **Journal of computational physics**, v. 171, n. 2, p. 776-804, 2001.

CFD ONLINE. **Turbulence intensity**. Disponível em: https://www.cfd-online.com/Wiki/Turbulence_intensity. Acesso em: 18 dez. 2020.

CHARLES, Wilson M. *et al.* Adaptive stochastic numerical scheme in parallel random walk models for transport problems in shallow water. **Mathematical and computer modelling**, v. 50, n. 7-8, p. 1177-1187, 2009.

CIONCOLINI, Andrea; THOME, John R.; LOMBARDI, Carlo. Algebraic turbulence modeling in adiabatic gas–liquid annular two-phase flow. **International Journal of Multiphase Flow**, v. 35, n. 6, p. 580-596, 2009.

COSTIGAN, G. **Flow pattern transitions in vertical gas-liquid flows**. 1997. Tese de Doutorado. University of Oxford.

CROWE, Clayton T. (Ed.). **Multiphase flow handbook**. CRC press, 2005.

DA RIVA, Enrico; DEL COL, Davide. Numerical simulation of churn flow in a vertical pipe. **Chemical Engineering Science**, v. 64, n. 17, p. 3753-3765, 2009.

DAVIDSON, Josh et al. Implementation of an openfoam numerical wave tank for wave energy experiments. In: **Proceedings of the 11th European wave and tidal energy conference**. European Wave and Tidal Energy Conference 2015, 2015.

DUKLER, A. E.; TAITEL, Yehuda. Flow pattern transitions in gas-liquid systems: measurement and modeling. **Multiphase science and technology**, v. 2, n. 1-4, 1986.

FABRE, Jean. Gas-liquid slug flow. In: **Modelling and experimentation in two-phase flow**. Springer, Vienna, 2003. p. 117-156.

GOVAN, A. H. *et al.* Flooding and churn flow in vertical pipes. **International journal of multiphase flow**, v. 17, n. 1, p. 27-44, 1991.

GOVAN, Alastair Hamilton. **Modelling of vertical annular and dispersed two-phase flows**. 1990.

GREENSHIELDS, Christopher J. **OpenFOAM user guide**. OpenFOAM Foundation Ltd, version, v. 3, n. 1, 2015, p. 47.

HAFEMANN, Thomas Eduardt et al. Modelling of Multiphase Fluid Flow and Heat Transfer in a Pre-salt Well to Predict APB. In: **Conference: IV Journeys of Multiphase Flows (JEM 2015)**, At Campinas, São Paulo, Brasil, Paper ID: JEM-2015-0058. 2015.

HERNANDEZ-PEREZ, Valente; ABDULKADIR, Mukhtar; AZZOPARDI, B. J. Grid generation issues in the CFD modelling of two-phase flow in a pipe. **The Journal of Computational Multiphase Flows**, v. 3, n. 1, p. 13-26, 2011.

HEWITT, G. F. **Handbook of Multiphase System**. McGraw-Hill, New York, 1982.

HEWITT, G. F.; GOVAN, A. H. Phenomenological modelling of non-equilibrium flows with phase change. **International journal of heat and mass transfer**, v. 33, n. 2, p. 229-242, 1990.

HEWITT, G. F.; HALL-TAYLOR, N. S.**Annular Two-Phase Flow**. Publisher: Pergamon Press., 1970.

HEWITT, Geoffrey F. Experimental and modelling studies of annular flow in the region between flow reversal and the pressure drop minimum. **Physico-Chemical Hydrodynamics**, v. 6, p. 43-50, 1985.

HILL, David Paul. **The computer simulation of dispersed two-phase flow.** 1998. Tese de Doutorado. University of London.

HUBBARD, M. G. and DUKLER, A. E. **The Chacacterization of Flow Regimes for Horizontal Two-Phase Flow**, Proc. Heat Transfer and Fluid Mech, Eds. M. A. Saad and J. A. Moller, Stanford University Press, 1966.

HUTCHINSON, P.; WHALLEY, P. A possible characterisation of entrainment in annular flow. **Chemical Engineering Science**, v. 28, n. 3, 1973, p. 974–975.

ISSA, Raad I.; GOSMAN, A. D.; WATKINS, A. P. The computation of compressible and incompressible recirculating flows by a non-iterative implicit scheme. **Journal of Computational Physics**, v. 62, n. 1, p. 66-82, 1986.

KAICHIRO, Mishima; ISHII, Mamoru. Flow regime transition criteria for upward two-phase flow in vertical tubes. **International Journal of Heat and Mass Transfer**, v. 27, n. 5, p. 723-737, 1984.

KARAMI, Hamidreza et al. CFD simulations of low liquid loading multiphase flow in horizontal pipelines. In: **Fluids Engineering Division Summer Meeting**. American Society of Mechanical Engineers, 2014. p. V002T06A011.

LEVY, Salomon. **Two-phase flow in complex systems**. John Wiley & Sons, 1999.

LIU, Y.; LI, W. Z.; QUAN, S. L. A self-standing two-fluid CFD model for vertical upward two-phase annular flow. **Nuclear Engineering and Design**, v. 241, n. 5, p. 1636-1642, 2011.

MALAMATENIOS, Ch; GIANNAKOGLOU, K. C.; PAPAILIOU, K. D. A coupled two-phase shear layer/liquid film calculation method. Formulation of the physical problem and solution algorithm. **International journal of multiphase flow**, v. 20, n. 3, p. 593-612, 1994.

MCQUILLAN, K. W. **Flooding in annular two-phase flow**. 1985. Tese de Doutorado. University of Oxford.

MCQUILLAN, K. W.; WHALLEY, P. B. Flow patterns in vertical two-phase flow. **International Journal of Multiphase Flow**, v. 11, n. 2, p. 161-175, 1985.

MEDINA, CÉSAR DANIEL PEREA. **Simulação numérica do escoamento bifásico líquido-gás em golfadas com transferência de calor em dutos horizontais**. Curitiba: Universidade Tecnológica Federal do Paraná, 159p. Dissertação de mestrado, 2011.

MENTER, Florian R. Two-equation eddy-viscosity turbulence models for engineering applications. **AIAA journal**, v. 32, n. 8, p. 1598-1605, 1994.

MENTER, Florian R.; KUNTZ, Martin; LANGTRY, Robin. Ten years of industrial experience with the SST turbulence model. **Turbulence, heat and mass transfer**, v. 4, n. 1, p. 625-632, 2003.

NOLETO, Luciano Gonçalves. **Uma abordagem Euleriana-Lagrangeana para simulação de escoamentos turbulentos com fronteiras móveis**. 2010.

OKAWA, Tomio; KATAOKA, Isao. Correlations for the mass transfer rate of droplets in vertical upward annular flow. **International journal of heat and mass transfer**, v. 48, n. 23-24, p. 4766-4778, 2005.

OWEN, David Garfield. **An experimental and theoretical analysis of equilibrium annular flows**. 1986. Tese de Doutorado. University of Birmingham.

OWEN, D. J. An improved annular two-phase flow model. In: **Third International Symposium on Multiphase Flow**, The Hague, 1987. BHRA, 1987.

PARSI, Mazdak *et al.* Assessment of a hybrid CFD model for simulation of complex vertical upward gas–liquid churn flow. **Chemical Engineering Research and Design**, v. 105, p. 71-84, 2016.

PHAM, Thinh Quy Duc; JEON, Jichan; CHOI, Sanghun. Quantitative comparison between volume-of-fluid and two-fluid models for two-phase flow simulation using OpenFOAM. **Journal of Mechanical Science and Technology**, v. 34, n. 3, p. 1157-1166, 2020.

QIU, Guodong *et al.* Numerical simulation of condensation of upward flow in a vertical pipe. In: **Fluids Engineering Division Summer Meeting**. American Society of Mechanical Engineers, 2014. p. V01DT32A003.

RIZZO FILHO, Haroldo dos Santos. **A otimização de gás lift na produção de petróleo: avaliação da curva de performance do poço.** 2011. Tese de Doutorado. Universidade Federal do Rio de Janeiro.

ROBERTS, D. N. **Studies of two-phase flow patterns by simultaneous X-ray and flash photography**. United Kingdom Atomic Energy Authority, 1969.

ROSA, Eugênio S. **Conceitos Básicos em Escoamentos Multifásicos**. In: ROSA, Eugênio S. Escoamento Multifásico Isotérmico. São Paulo: Bookman, 2012, p. 1-16.

SALLES, Marcos Vinícius. **Numerical Simulation of the vertical annular gas-liquid two-phase flow**. 2020. 78 f. Dissertação (Mestrado) - Curso de Engenharia Mecânica, Centro de Ciências Tecnológicas, Universidade do Estado de Santa Catarina, Joinville, 2020.

SANTIAGO, D. I. **Aplicação de um Modelo Lagrangiano de Trajetória de Partículas para Modelagem da Dispersão em Águas Rasas e Simulação no Canal de Acesso ao Porto de Vitória.** 2007. Dissertação (Mestrado em Engenharia Ambiental) - Programa de Pós Graduação em Engenharia Ambiental, Universidade Federal do Espírito Santo, 2007.

SANTOS, Fernando Luiz Pio dos. **Simulação numérica euleriana de escoamento gás-sólido em riser com dimensões reduzidas aplicando malhas refinadas**. 2008. Tese de Doutorado. Universidade de São Paulo.

SAWAI, T. *et al.* Gas–liquid interfacial structure and pressure drop characteristics of churn flow. **Experimental thermal and fluid science**, v. 28, n. 6, p. 597-606, 2004.

SEKOGUCHI, K. New development of experimental study on interfacial structure in gas-liquid two-phase flow. In: Proc. **4th World Conference on Experimental Heat Transfer, Fluid Mechanics and Thermodynamics**, Brussels. 1997. p. 1177-1188.

SIVIER, S. *et al.* Eulerian-Eulerian and Eulerian-Lagrangian methods in two phase flow. In: **Thirteenth international conference on numerical methods in fluid dynamics**. Springer, Berlin, Heidelberg, 1993. p. 473-477.

SKOPICH, Anton *et al.* Pipe-diameter effect on liquid loading in vertical gas wells. **SPE Production & Operations**, v. 30, n. 02, p. 164-176, 2015.

SOUSA, José Bezerra; LIMA, Elias Manoel; ANAZIA, Ricardo. **Utilização de Modelos Matemáticos de Poluição Atmosférica na Gestão da Qualidade do Ar**.

SPIVAKOVSKAYA, D.; HEEMINK, A. W.; DELEERSNIJDER, Eric. **The backward Îto method for the Lagrangian simulation of transport processes with large space variations of the diffusivity**. 2007.

TATTERSON, David Franklin. **Rates of automization and drop size in annular two phase flow**. PhDT, 1975.

TEKAVČIČ, Matej; KONČAR, Boštjan; KLJENAK, Ivo. Three-dimensional simulations of liquid waves in isothermal vertical churn flow with OpenFOAM. **Experimental and Computational Multiphase Flow**, v. 1, n. 4, p. 300-306, 2019.

TEZDUYAR, Tayfun E. Interface-tracking and interface-capturing techniques for finite element computation of moving boundaries and interfaces. **Computer Methods in Applied Mechanics and Engineering**, v. 195, n. 23-24, p. 2983-3000, 2006.

THAKER, Jignesh P.; BANERJEE, Jyotirmay. CFD simulation of two-phase flow phenomena in horizontal pipelines using openfoam. In: **Proceedings of the Fortieth National Conference on Fluid Mechanics and Fluid Power**. 2013.

TOCCI, F. **Assessment of a hybrid VOF two-fluid CFD solver for simulation of gas-liquid flows in vertical pipelines in OpenFoam.** 2016. 100 f. Dissertação (Mestrado) - Curso de Engenharia Aeronáutica, Politecnico di Milano, Milão, 2016.

VAN DER MEULEN, Gerrit Pieter. **Churn-annular gas-liquid flows in large diameter vertical pipes**. 2012. Tese de Doutorado. University of Nottingham.

WALLIS, G. B.**One-Dimensional Two-Phase Flow**.[S.l.]: McGraw-Hill, 1969.

WALTRICH, Paulo J.; FALCONE, Gioia; BARBOSA JR, Jader R. Liquid transport during gas flow transients applied to liquid loading in long vertical pipes. **Experimental Thermal and Fluid Science**, v. 68, p. 652-662, 2015.

WALTRICH, Paulo Jose. **Onset and subsequent transient phenomena of liquid loading in gas wells: experimental investigation using a large scale flow loop**. Texas A&M University, 2012.

WANG, Ke; YE, Jing; BAI, Bofeng. Entrained droplets in two-phase churn flow. **Chemical Engineering Science**, v. 164, p. 270-278, 2017.

WARDLE, Kent E.; WELLER, Henry G. Hybrid multiphase CFD solver for coupled dispersed/segregated flows in liquid-liquid extraction. **International Journal of Chemical Engineering**, v. 2013, 2013.

WELLER, Henry G. A new approach to VOF-based interface capturing methods for incompressible and compressible flow. **OpenCFD Ltd.**, Report TR/HGW, v. 4, 2008.

WHALLEY, P. B.; HEWITT, G. F. **The correlation of entrained fraction and entrainment rate in annular two-phase flow**, 1978. 123 p.

WHALLEY, P.; HEWITT, G.; HUTCHINSON, P. Experimental wave and entrainment measurements in vertical annular two-phase flow. **Multi-Phase Flow Systems Symposium**, Stratclyde, 1974.

WILCOX, David C. et al. **Turbulence modeling for CFD**. La Canada, CA: DCW industries, 1998.

WOLF, A.; JAYANTI, S.; HEWITT, G. F. Flow development in vertical annular flow. **Chemical Engineering Science**, v. 56, n. 10, p. 3221-3235, 2001.

WOLF, A.; JAYANTI, S.; HEWITT, G. F. On the nature of ephemeral waves in vertical annular flow. **International journal of multiphase flow**, v. 22, n. 2, p. 325-333, 1996.

WOLFF, F. G. **Análise de um modelo de escoamento bifásico ar-água em tubos verticais.** 2012. Trabalho apresentado como requisito parcial para obtenção do grau de Bacharel em Engenharia de Mecânica, Universidade Federal de Santa Catarina, Florianópolis, 2012.

WOLK, Frank. **Three-dimensional Lagrangian tracer modelling in Wadden Sea areas**. 2003. Tese de Doutorado.

ZHANG, Zhennan *et al.* Experimental study on entrained droplets in vertical two-phase churn and annular flows. **International Journal of Heat and Mass Transfer**, v. 138, p. 1346-1358, 2019.